ON THE ROLE OF PROJECTILE ELECTRONS IN AN INDEPENDENT ELECTRON MODEL DESCRIPTION OF DRESSED-ION IMPACT ON ATOMS

GERALD FRANZ BERNHARD SCHENK

A Dissertation submitted to the Faculty of Graduate Studies
in Partial Fulfillment of the Requirements for the Degree of
Doctor of Philosophy

Graduate Program in Physics and Astronomy
York University
Toronto, Ontario

June 2016

ABSTRACT

The presence of electrons on ions which collide with neutral atoms constitutes a challenge to theoretical descriptions of the collision dynamics. These collisions pose quantum-mechanical many-body problems that cannot be fully solved; one has to resort to approximations, such as the independent electron model (IEM), in which the N-electron problem is reduced to N single-electron problems. The time-development of a given electron is governed by the nuclear Coulomb potentials and an electronic mean-field potential formed by the other electrons. This framework is used in the present work to explore the active role of projectile electrons in collisions of dressed boron- and carbon-ions with neon atoms, as well as the seemingly simple He^+–He collision system.

In the present IEM description the collision problem is expressed in the form of time-dependent Schrödinger equations with a common single-electron Hamiltonian. The single-electron equations are solved numerically with a two-centre basis expansion method in which the continuum is represented by dynamically generated basis states. From these calculations single-electron transition amplitudes are obtained and many-electron quantities are computed with different statistical final-state analyses, which do or do not respect the Pauli exclusion principle.

In B^{2+}–Ne collisions transfer ionization processes that involve electrons at both centres were found to contribute to target multiple ionization coincident with an unchanged projectile charge state. Total

cross sections for collision channels where the projectile charge state is changed are presented for B^{2+}–Ne and C^{3+}–Ne collisions. The present method reliably provides total cross sections for most collision channels, except for the loss of projectile electrons. The contributions of these collision channels to the net recoil ion production are investigated. These results are compared with those for collisions of equicharged bare helium and lithium ions with neon.

In a modification of the present approach a piecewise definition of the common Hamiltonian is proposed. It ensures the correct asymptotic behaviour of the mean-field potential at large internuclear distances before the collision for active electrons of both centres. The model is applied to the He^+–He collision system and compared with the (unmodified) present approach.

ACKNOWLEDGEMENTS

In view of the long gestation of this dissertation, which may have been a rather exhaustive test of a supervisor's patience, I am all the more grateful to Prof. Tom Kirchner for his never failing kindness, courtesy, and helpfulness.

I shall always be grateful, as well, to Prof. Marko Horbatsch who in many discussions and seminars led me to questions that are relevant to the present work, and who provided valuable comments on the manuscript of this dissertation.

I am very much indebted to Prof. Hans Jürgen Lüdde for numerous correspondences through which I learnt that most obstacles I encountered in the numerical calculations were in fact evoked by not understanding the limits of physical models and approximations.

My sincerest thanks are due to Prof. Randy Lewis who as a member of my supervisory committee heard my research evaluations and encouraged me through calm reassurance.

I thank my examining committee and their chair Prof. Cody Storry for making themselves familiar with my research and advising me on several changes to the dissertation. In particular, I am grateful to Prof. Michael Daly, since atomic collision physics are not quite that close to his own research, which may have made this already dry text somewhat tedious to read. I am also especially thankful for the commitment of Prof. David Schultz despite the many obligations his offices at the University of North Texas certainly must bring.

My warmest thanks for their help through advice and insightful discussions are due to my colleagues Myrek Zapukhlyak, Mitsuko Murakami, and Maciek Śpiewanowski, as well as Alain Marsman- and Matthew Baxter, who also were so kind to advise me in countless instances on the wording of this dissertation.

CONTENTS

LIST OF TABLES

LIST OF FIGURES

GLOSSARY

AC	asymptotic correction
BGM	basis generator method
CDW-EIS	continuum distorted wave with eikonal initial state (method)
CMF	common–mean-field
COLTRIMS	cold target recoil ion momentum spectroscopy
CTMC	classical trajectory Monte Carlo (method)
DCS	differential cross sections
DFT	density functional theory
HF	Hartree–Fock
IEM	independent electron model
KS	Kohn–Sham
*n*CTMC	*n*-body CTMC
OC-BGM	one-centre BGM
OPM	optimized potential method
SE	Schrödinger equation
TC-BGM	two-centre BGM
TCAO	two-centre atomic orbital
TDDFT	time-dependent DFT
TDHF	time-dependent Hartree–Fock
TDOPM	time-dependent OPM
TDSE	time-dependent Schrödinger equation

INTRODUCTION

The research topic of the present dissertation is the theoretical analysis of ion–atom collisions at intermediate impact energies in which the projectile ion carries electrons into the collision. In the following such ions are called *dressed* ions.

Collisions of dressed ions with atoms are common in nature and in technical applications. For example, under plasma conditions encountered in fusion research collisions occur over a wide impact-energy range and with diverse collision partners, including intermediate-energy impact by heavy ions in low charge states [1–3]. Examples can also be found in solar system research, such as plasma in the Jovian system which was found to contain dressed sulphur ions [4]. Fast heavy ions were detected in the magnetosphere of Jupiter giving reason to expect intermediate-energy dressed-ion–atom collisions to occur [5]. Dressed-ion impact can also be relevant in applications of swift bare-ion beams when the beam passes media where multiple consecutive collisions occur. By transferring momentum in collision initially swift ions are slowed to the intermediate impact-energy regime. Electron capture from target atoms is then likely, these are carried into consecutive collisions. (This is in contrast to ion-atom–collision experiments where gas targets are kept at low pressure and thin enough to ensure single collision conditions, e.g. 0.1 Pa for a 2 mm interaction length in a target gas jet [6]). An example where collisions in a dense medium occur is the stopping of fast ions in water, e.g. in radiation therapy with ion beams [7–9]. In

medical applications of ion beams an accurate prediction of the spatial distribution of the energy deposited by the ions is required, often model descriptions of the stopping process are used [10, 11]. On a microscopic scale the stopping mechanisms are tremendously more complex than what is typically considered in atomic and molecular collision physics where single collisions are considered. The same applies to the plasma physics examples mentioned above. Models describing these processes often rely on experimental and theoretical data that quantify single collision events, and this data is typically provided in databases [12].

In the intermediate energy range, from about 10 keV/u to a few MeV/u, excitations, transfer of electrons between the atom and the ion, and transitions to the continuum occur. The following nomenclature is often used: electron *removal* from the target can happen due to electron *capture* by the projectile or emission of electrons (*ionization*) in consequence producing a *recoil ion* [13]. Projectile electron *loss*, coincident with electron removal from neutral target atoms, occurs typically in the form of electron emission to the continuum [14]. These descriptive terms are somewhat too simple in order to discuss dressed-ion–atom collisions of interest where multiple electron processes are very likely. The coincident transfer of many electrons and a large number of possible transfer channels give rise to complexity.

A theoretical description of these collision processes is difficult on a fundamental level. This can be seen when taking one step back, to the problem of *bare*-ion impact on atoms, i.e. collisions with projectile ions stripped entirely of electrons before the collision. The theory of these collisions has been understood for a long time through quantum mechanics, in particular the time-dependent Schrödinger equation (TDSE) [15], that has been known for ninety years. Yet, because many-particle problems cannot be solved analytically, collision problems remained a challenge ever after. Theoretical descriptions have to rely on approximations and models to find solutions numerically.

An example for such a model description is the independent electron model (IEM) [16] where the many-electron problem is simplified to single-electron problems. Electron-electron interactions are approximated through an electronic mean-field potential. An electron is referred to as an *active* electron when its time development is considered in this model. In cases where only the contribution to the mean field is taken into account the expression *passive* electrons is used. In order to obtain many-electron quantities from the single-electron solutions a statistical final-state analysis is used. An example for such a many-electron quantity is the probability to find the system in a specific configuration after the collision.

Further approximations are needed to solve single-electron problems. An example are perturbative methods: The first-order Born approach used by Bates and Griffing [17] for fast proton–hydrogen collisions allows only small perturbations and is limited to fast collisions and low projectile charge states. With higher-order perturbative methods, such as the continuum distorted wave – eikonal initial state (CDW-EIS) [18] method, these limits have been pushed and ion–atom collisions at intermediate impact energies can be considered. Starting from a Born ansatz the projectile is considered a perturbing influence and the plane initial and final waves are distorted by phase factors that arise from Coulomb interaction with the nuclear charges [19, 20]. The initial wave function is normalized and an eikonal approximation is used to describe the state of the target electron in the field of the distant projectile at initial time [18]. The CDW-EIS method has been used widely in calculations, for example, for electron capture by bare helium ions in collisions with helium atoms [21, 22], and multiple ionization of noble gases by bare ion impact [23–26].

When using perturbative methods for dressed-ion–atom collision problems active electrons are typically considered either for the target or for the projectile. Passive electrons of the dressed-ion projectiles in collisions with atomic hydrogen were represented by a

parametric effective model charge in first-order perturbation theory calculations [27]. Often a constant effective charge is used in CDW-EIS calculations, an example at intermediate impact energies are calculations for Li^+–He collisions [28]. However, this approach is mostly used for collisions with fast highly-charged dressed ions [29–32]. The CDW-EIS approach by Miraglia and Gravielle [33] to describe dressed-ion–atom collisions at intermediate impact energies uses an effective projectile charge that is a function of the momentum transferred in the collision. Calculations with this method were made for He^+ impact on noble gases [26, 34] and B^{2+} impact on Ne [35].

Perturbative methods are often not reliable for collisions at the lower end of the intermediate impact energy regime [36]. A non-perturbative, albeit classical theory, is the classical trajectory Monte Carlo (CTMC) method [37, 38]. In CTMC the electron is treated as a classical particle whose initial position and momentum determine a trajectory subject to the Coulomb potentials of target and projectile. The nuclear motion is determined in reference [38] separately from the electronic problem as a classical two-body problem. A large number of samples are randomly drawn from the initial probability distribution of the electrons' positions and momenta, each sample determines a trajectory. These trajectories are calculated and results can be categorized, based on their final position and momentum, as belonging to one of three possible channels, the electron remains at its centre, it is transferred to the other centre, or emitted as a free particle [37]. The method was extended to more than one electron with an IEM [39], and has been used for a wide range of collision problems [13].

Beyond the IEM the presence of electrons at both collision centres in dressed-ion–atom collisions can be directly addressed in the framework of CTMC by considering target and projectile electrons in an n-body calculation [40]. This n-body CTMC (nCTMC) approach has been used for F^{6+}–Ne collisions [40] and dressed beryllium-ion im-

pact on hydrogen [41]. Further examples for the nCTMC method are calculations for simultaneous ionization of He^+ in impacts with Ne [42], and electron emission from the Li^+–He system [28]. Constant effective projectile charges were used in CTMC calculations where the dressed-ion–hydrogen collision system was treated as an effective one-electron problem [38]. The IEM in conjunction with the CTMC has been applied to dressed-ion–helium collision problems, for example, [5, 43].

Calculations where the electronic problem was treated fully quantum mechanically and with a non-perturbative method came late, compared to the methods mentioned above. One reason appears to be that computing hardware had to advance to make such calculations numerically feasible. Schaudt et al used a time-dependent Hartree–Fock (TDHF) method to describe charge transfer in He^{2+}–He collisions [44]. In the TDHF method the many-electron wave functions are expressed as Slater determinants comprising single-electron wave functions. The time development of these single-electron wave functions is described by equations that are derived by variational treatment of the action integral for the many-electron system. By expanding wave functions in a finite basis differential equations can be rendered as a system of coupled equations that can be expressed in matrix-vector form and solved numerically. Such coupled-channel methods have been used for calculations in one-electron collision systems, for example [45], and for a wide range of ion–atom collisions with the basis generator method (BGM) [46], for example, proton impact on atomic oxygen [47] and bare-ion impact on noble gases [48, 49]. The many-electron problem was addressed through an IEM. (The present work relies on the BGM, a brief summary of the method will follow below.)

Active target and projectile electrons in dressed-ion collisions were considered in independent BGM calculations that were combined in a final-state analysis [50]. This approach has been applied to He^+–Ne

[50, 51] and C^{3+}-Ne [52] collisions. An overview of BGM calculations can be found in reference [53].

Dressed-ion–atom collisions provide, due to the the presence of electrons at the projectile, interesting tests for theorectical models, notably in the framework of the IEM. The role of projectile electrons can be coarsely separated into an active role, in which their transitions change the charge states of target and projectile, and into a passive role, that of screening the projectile nucleus. In an IEM description the active and the passive role of electrons can be investigated separately. Projectile electrons can be included or omitted at the level of a statistical final-state analysis which allows to study their active effect on the collision products (presupposed, the method allows active projectile electrons in the first place). Comparisons with equicharged bare-ion impact – that is, impact of an ion with like initial charge state – on the same target atom help to understand the passive role of projectile electrons.

Collision Systems of Interest

In the present work theoretical results will be compared with experimental data in the form of cross sections as functions of the impact energy. Total target ionization and electron transfer cross sections for dressed-ion impact have been measured in a number of experiments, for example, dressed-ion impact on hydrogen [54, 55], and on noble gas atoms [6, 35, 52, 55–65]. Yet, not in all experiments target charge states were measured in coincidence with projectile charge states, which is required to investigate the active role of projectile electrons. In addition, experimental data ought to be available for equicharged bare-ion collision systems, in order to make comparison possible. Collision systems for which this is the case, and that have been investigated in the course of the present work, are B^{2+}–Ne [35, 62] and C^{3+}–Ne [52, 61–64]. The corresponding equicharged bare-ion

collision systems are He^{2+}–Ne [66, 67] and Li^{3+}–Ne [52, 64], respectively.

Absolute total cross section measurements are difficult, and experimental results are typically normalized [68] (e.g. to net ion production cross sections σ_+ measured by Rudd et al [58, 66, 69]). In comparisons of theory and experiment in this work more attention is given to the shape of data with regard to the impact energy and to consistency among different channels than is given to close coincidence of theoretical and experimental values on an absolute scale.

Present Theory

A semi-classical description of the collision problem is used in this work. This approach, where the electronic problem is described quantum mechanically and the nuclear motion is dealt with classically, is possible since with the Born–Oppenheimer approximation [70] both problems can be separated, and since quantum effects are not relevant to the nuclear motion for the impact energies and impact parameters of interest. The nuclear motion is described by straight-line trajectories; this is a good approximation as long as impact energies exceed $> 5\,\mathrm{keV/u}$ [71]. The fastest collisions in this work at impact energies $E \approx 2\,\mathrm{MeV/u}$ are still slow enough to treat the problem using a non-relativistic description.[1] While relativistic effects can play a role when dealing with the strong fields of nuclei with high atomic numbers they are negligible for the atoms (ions) considered in the present work [72].

A TDHF ansatz is used for the electronic problem. The many-electron wave function is expressed as a Slater determinant of single-electron wave functions whose time development is described by

[1] $E = 2\,\mathrm{MeV/u}$ corresponds to the velocity in atomic units $v = 9\,\mathrm{au}$, with $c = 137\,\mathrm{au}$ the Lorentz factor $\gamma = \left(1 - v^2/c^2\right)^{-1/2} = 1.0027$ differs only slightly from unity.

TDHF equations. These equations contain Hartree terms, that correspond to the electronic screening of the nuclear potential, and nonlocal exchange terms. Approximating these terms with local mean-field potentials leads to single-electron equations in TDSE form. In these equations the time development of all electrons initially at the target (projectile) depends on the same single-electron Hamiltonian, for which exchange is considered at the target (projectile) only.

In the common–mean-field approach the same Hamiltonian is used for electrons of both centres. This is a pragmatic approximation, and one can get good results when investigating target electron removal that is due to transitions to the continuum and (or) transfer to the projectile. On the flip side, for initial projectile electrons the common–mean-field approach approximates the asymptotic behaviour of the effective potentials poorly. In consequence one cannot expect good results for collision channels that depend mostly on transitions of projectile electrons. Nonetheless, the common–mean-field approach is used for most of the present calculations, as the collision channels of interest are dominated by target electron transitions.

The electronic mean field has to change in time if it is to correspond to the changing electronic state over the course of the collision. This time dependence is present in the TDHF ansatz, but was lost in the local potential approximations used in this work. This is dealt with in two ways: In the no-response approximation the time dependence is neglected and the shape and strength of the initial mean field potentials of the atom and the ion are constant in time. In the global target-response model the time dependence of the target mean-field potential is approximated by scaling the initial potential with a factor that depends on the net target occupation. Numerical atomic and ionic ground-state potentials are used for the initial mean-field potentials in the present calculation [73].

The single-electron equations are solved with the BGM [46], a basis expansion method in a finite model space. Target atomic orbitals and

states that are generated thereof span the model space. The generation scheme approximates an optimum solution space as the system develops in time. The dynamical adaptation of the model space to the problem allows convergent results with a manageable basis size. In the two-centre BGM (TC-BGM) [74] the basis also contains ionic eigenstates of the projectile, which leads to a more accurate description of electron transfer between both collision partners and allows to consider active electrons that are initially at the projectile. Calculations that were carried out with the earlier implementation of BGM, where no projectile states are included in the basis, are henceforth referred to as one-centre BGM (OC-BGM).

In the statistical final-state analysis many-electron observables are calculated, namely, probabilities to find k electrons at the projectile and l in the continuum. In the determinantal method the many-electron probabilities are calculated from inner products of Slater determinants of the propagated single-electron wavefunctions and a final configuration. The method of Lüdde and Dreizler [75] is used to reduce the numerical complexity of this problem. Since Slater determinants are used the correct antisymmetric property of the many-electron state is ensured, and accordingly, the Pauli principle is adhered to in this calculation. The other statistical final-state analysis used in the present calculations is the multinomial method. A combinatoric approach is used to calculate many-electron probabilities from single-electron transition probabilities. The multinomial analysis does not adhere to the Pauli principle.

Structure of this Dissertation

In the first chapter the single-electron equations are derived, beginning from the TDHF ansatz, following the steps mentioned above. Chapter 2 is to give an overview of the TC-BGM. The statistical methods used to calculate many-electron probabilities are described in

the third chapter. In chapter 4 the size and composition of the basis as well as its convergence with regard to small changes is discussed. This is followed, in the same chapter, by test calculations to analyze different approaches to the extraction of probabilities when target response is considered.

In the fifth chapter results for ion–neon collisions are shown and discussed. It begins with a detailed investigation of target ionization coincident with an unchanged projectile charge state in B^{2+}–Ne collisions. In the following sections the discussion is extended to to collision channels where the projectile charge state changes. In addition, further collision systems are considered, namely, He^{2+}, Li^{3+}, and C^{3+} impact on neon. This includes a comparison of results of target-response and no-response calculations, an analysis of contributions to the net recoil ion production, and a comparison of dressed-ion impact with equicharged bare-ion impact on neon.

In the sixth chapter a different approach to combine the target and the projectile problem is investigated. A piecewise defined potential function is used in a Hamiltonian for electrons of both centres, in order to improve the description of projectile electron loss processes without worsening target ionization and capture results. At large internuclear distances before the collision the piecewise potential function shows the correct asymptotic behaviour for electrons of the target and the projectile. This asymptotic-correction approach is applied to the He^+–He collision system, and calculated results are compared with experimental data [58, 68, 76–78]. The dissertation is concluded in the following chapter.

Atomic Units

Atomic units $\hbar = m_e = 4\pi\epsilon_0 = e = 1$ are used throughout this dissertation, unless stated otherwise. When it is thought to improve clarity values in atomic units may be denoted by an 'a.u.' suffix.

Exceptions to the use of atomic units are, impact energies E in 'eV', unified atomic mass units 'u', and total cross sections σ in 'cm^2'.

1 INDEPENDENT ELECTRON MODEL FOR DRESSED–ION–ATOM COLLISIONS

The collision systems of interest in this work permit to describe the nuclear motion independently of the electronic problem in a semi-classical approximation where the nuclear motion happens on predetermined trajectories. In the intermediate-energy regime the velocity v_{rel} of the projectile relative to the target is fast enough to allow the use of straight-line trajectories with an impact parameter approximation. As discussed in the introduction the present collision problems can be treated non-relativistically.

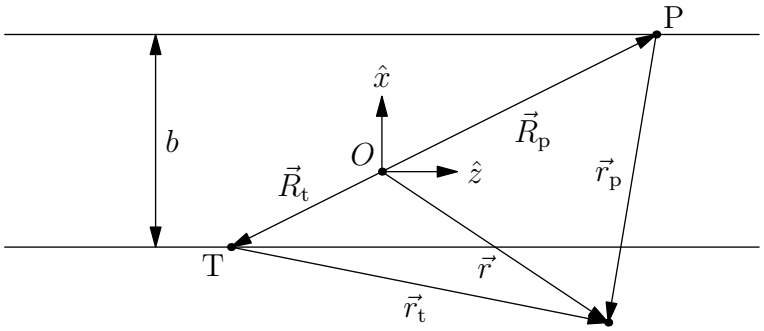

Figure 1: Diagram of the geometry of the B^{2+}–Ne collision system, using the straight-line–trajectory approximation. (The origin is shown at the centre of mass for the B^{2+}–Ne collision system.)

Figure 1 shows the scattering plane of the collision system. $\boldsymbol{R}_{\mathrm{t}}(t)$ and $\boldsymbol{R}_{\mathrm{p}}(t)$ are the position vectors of both centres with respect to the

centre-of-mass. The respective velocities are

$$\boldsymbol{v}_\mathrm{t} = -\frac{M_\mathrm{t}}{M_\mathrm{t}+M_\mathrm{p}} v_\mathrm{rel}\hat{z} \quad \text{and} \quad \boldsymbol{v}_\mathrm{p} = \frac{M_\mathrm{p}}{M_\mathrm{t}+M_\mathrm{p}} v_\mathrm{rel}\hat{z}, \tag{1}$$

where M_t and M_p are the masses of the target and projectile nuclei. The vectors $\boldsymbol{r}_\mathrm{t} = \boldsymbol{r} - \boldsymbol{R}_\mathrm{t}(t)$ and $\boldsymbol{r}_\mathrm{p} = \boldsymbol{r} - \boldsymbol{R}_\mathrm{p}(t)$ point from each collision centre to the position $\boldsymbol{r}$ of an electron. The collision is followed over a finite time interval, such that the internuclear distance at initial time t_0 and final time t_f is sufficiently large for transition probabilities to stabilize. The perturbation on either collision partner by the other is then negligible. Both, the target atom and the projectile ion are assumed to be in their ground state at $t = t_0$. The target is a closed-shell neutral atom with $N_\mathrm{t} = Z_\mathrm{t}$ electrons. The projectile is an ion that carries $N_\mathrm{p} = 0, \ldots, Z_\mathrm{p} - 1$ electrons into the collision. Z_t and Z_p are the atomic numbers of the target and projectile, respectively.

1.1 THE MANY-ELECTRON PROBLEM

With the presuppositions of semi-classical approximation and non-relativistic description the collision problem becomes a many-electron problem described by the TDSE

$$\big(\hat{H}(t) - \mathrm{i}\partial_t\big)\Psi(t) = 0, \tag{2}$$

with the initial condition $\Psi(t_0) = \Psi_0$. The Hamiltonian $\hat{H}(t) = \hat{T} + \hat{V}_{ee} + \hat{V}_\mathrm{ext}(t)$ comprises the kinetic energy of the electrons, electron-electron interaction, and the external potential due to the collision centres' Coulomb potentials. Expressed for N electrons it reads

$$\hat{H}(t) = \sum_{i=1}^{N}\left(-\frac{1}{2}\Delta_i\right) + \sum_{i<j}^{N}\frac{1}{|\boldsymbol{r}_i - \boldsymbol{r}_j|} + \sum_{i=1}^{N}\left(-\frac{Z_\mathrm{t}}{|\boldsymbol{r}_i - \boldsymbol{R}_\mathrm{t}|} - \frac{Z_\mathrm{p}}{|\boldsymbol{r}_i - \boldsymbol{R}_\mathrm{p}|}\right). \tag{3}$$

The problem (2) is solved in an independent electron approximation with the TDHF approach of reference [50]. In this approximation, the many-electron wave function is at all times given by a single Slater determinant

$$\Psi(\boldsymbol{r}_1,\ldots,\boldsymbol{r}_N,\sigma_1,\ldots,\sigma_N,t)=\frac{1}{\sqrt{N!}}\begin{vmatrix}\psi_{1\sigma_1}(\boldsymbol{r}_1,t) & \ldots & \psi_{N\sigma_N}(\boldsymbol{r}_1,t)\\ \vdots & & \vdots\\ \psi_{1\sigma_1}(\boldsymbol{r}_N,t) & \ldots & \psi_{N\sigma_N}(\boldsymbol{r}_N,t)\end{vmatrix} \tag{4}$$

for the orthonormal set of single-electron states $\{|\psi_{i\sigma_i}\rangle\}$, where the z-component of the spin is denoted by the index σ_i. In order to make it easier to specifically discuss the time development of electrons of either collision centre it is useful to distinguish between wave functions corresponding to initial target and projectile electrons, respectively denoted by $\theta_{i\sigma_i}$ and $\phi_{j\sigma_j}$; $|\Psi\rangle = |\theta_{1\sigma_1}\cdots\theta_{N_\mathrm{t}\sigma_{N_\mathrm{t}}}\,\phi_{1\sigma_1}\cdots\phi_{N_\mathrm{p}\sigma_{N_\mathrm{p}}}\rangle$. The TDHF equations that govern the time development are found with the variational principle applied to the action functional [79]

$$A[\Psi]=\int_{t_0}^{t_\mathrm{f}}\mathrm{d}t\langle\Psi(t)\,|\,\mathrm{i}\partial_t-\hat{H}(t)\,|\,\Psi(t)\rangle, \tag{5}$$

for the Hamiltonian (3) and Slater determinant (4). The action becomes stationary, $\delta A=0$, with regard to variations $\delta\psi^*_{i\sigma_i}$ when the

TDHF equations are satisfied:

$$
\begin{aligned}
\mathrm{i}\partial_t \theta_{i\sigma_i}(\boldsymbol{r},t) = &\left(-\frac{1}{2}\Delta - \frac{Z_\mathrm{t}}{r_\mathrm{t}} - \frac{Z_\mathrm{p}}{r_\mathrm{p}}\right)\theta_{i\sigma_i}(\boldsymbol{r},t) \\
&+ \sum_{k=1}^{N_\mathrm{t}} \int \mathrm{d}^3 r' \, \frac{\left|\theta_{k\sigma_k}(\boldsymbol{r}',t)\right|^2}{|\boldsymbol{r}-\boldsymbol{r}'|}\theta_{i\sigma_i}(\boldsymbol{r},t) \\
&- \sum_{k=1}^{N_\mathrm{t}} \delta_{\sigma_i\sigma_k} \int \mathrm{d}^3 r' \, \frac{\theta^*_{k\sigma_k}(\boldsymbol{r}',t)\,\theta_{i\sigma_i}(\boldsymbol{r}',t)}{|\boldsymbol{r}-\boldsymbol{r}'|}\,\theta_{k\sigma_k}(\boldsymbol{r},t) \\
&+ \sum_{l=1}^{N_\mathrm{p}} \int \mathrm{d}^3 r' \, \frac{\left|\phi_{l\sigma_l}(\boldsymbol{r}',t)\right|^2}{|\boldsymbol{r}-\boldsymbol{r}'|}\,\theta_{i\sigma_i}(\boldsymbol{r},t) \\
&- \sum_{l=1}^{N_\mathrm{p}} \delta_{\sigma_i\sigma_l} \int \mathrm{d}^3 r' \, \frac{\phi^*_{l\sigma_l}(\boldsymbol{r}',t)\,\theta_{i\sigma_i}(\boldsymbol{r}',t)}{|\boldsymbol{r}-\boldsymbol{r}'|}\,\phi_{l\sigma_l}(\boldsymbol{r},t),
\end{aligned}
\tag{6}
$$

for initial conditions of the target, $i = 1, \ldots, N_\mathrm{t}$, and

$$
\begin{aligned}
\mathrm{i}\partial_t \phi_{j\sigma_j}(\boldsymbol{r},t) = &\left(-\frac{1}{2}\Delta - \frac{Z_\mathrm{t}}{r_\mathrm{t}} - \frac{Z_\mathrm{p}}{r_\mathrm{p}}\right)\phi_{j\sigma_j}(\boldsymbol{r},t) \\
&+ \sum_{k=1}^{N_\mathrm{p}} \int \mathrm{d}^3 r' \, \frac{\left|\phi_{k\sigma_k}(\boldsymbol{r}',t)\right|^2}{|\boldsymbol{r}-\boldsymbol{r}'|}\phi_{j\sigma_j}(\boldsymbol{r},t) \\
&- \sum_{k=1}^{N_\mathrm{p}} \delta_{\sigma_j\sigma_k} \int \mathrm{d}^3 r' \, \frac{\phi^*_{k\sigma_k}(\boldsymbol{r}',t)\,\phi_{j\sigma_j}(\boldsymbol{r}',t)}{|\boldsymbol{r}-\boldsymbol{r}'|}\,\phi_{k\sigma_k}(\boldsymbol{r},t) \\
&+ \sum_{l=1}^{N_\mathrm{t}} \int \mathrm{d}^3 r' \, \frac{\left|\theta_{l\sigma_l}(\boldsymbol{r}',t)\right|^2}{|\boldsymbol{r}-\boldsymbol{r}'|}\,\phi_{j\sigma_j}(\boldsymbol{r},t) \\
&- \sum_{l=1}^{N_\mathrm{t}} \delta_{\sigma_j\sigma_l} \int \mathrm{d}^3 r' \, \frac{\theta^*_{l\sigma_l}(\boldsymbol{r}',t)\,\phi_{j\sigma_j}(\boldsymbol{r}',t)}{|\boldsymbol{r}-\boldsymbol{r}'|}\,\theta_{l\sigma_l}(\boldsymbol{r},t),
\end{aligned}
\tag{7}
$$

for initial conditions of the projectile, $j = 1, \ldots, N_\mathrm{p}$. The propagated states $|\theta_{i\sigma_i}(t)\rangle$, $|\phi_{j\sigma_j}(t)\rangle$ remain orthonormal throughout the time development.

Listed line-by-line, the components of the TDHF equations for the initial target electrons (6) are: First, the terms corresponding to the

kinetic energy T and the external potential V_{ext}; then from the second line on the terms related to V_{ee} – beginning with the Hartree potential of the target electrons

$$v^{\text{t}}_{\text{Ha}}(\boldsymbol{r}, t) = \sum_{k=1}^{N_{\text{t}}} \int \mathrm{d}^3 r' \, \frac{\left|\theta_{k\sigma_k}(\boldsymbol{r}', t)\right|^2}{|\boldsymbol{r} - \boldsymbol{r}'|}. \tag{8}$$

The third line contains the TDHF exchange term for the initial target electrons of equal spin z-projection. It is followed by the Hartree potential of the projectile electrons $v^{\text{p}}_{\text{Ha}}(\boldsymbol{r}, t)$, defined by the same token as (8). Finally, there is a two-centre exchange term, that depends on the overlap of the propagated wave function $\theta_{i\sigma_i}$ with those propagated by equation (7) $\phi_{j\sigma_j}$ of equal spin z-projection. The projectile TDHF equations (7) follow the same pattern.

In extension of [50], where due to the single electron of a He^+ ion projectile the TDHF equations are slightly simpler, N_{p} electrons are considered in (6), and in (7). Collision systems with more than one open shell cannot be described with the present ansatz [80]. In the present work only target atoms with closed shells are considered, viz. helium and neon. The dressed-ion projectiles are limited to spin doublet systems, in the present calculations these are He^+, B^{2+}, and C^{3+}.

Over the course of a collision the Hartree potential can change considerably as the wave functions develop in time. This can be interpreted with the physical picture of changing charge clouds that are screening the nuclei [44]. Response is a cause for the non-linearity of the TDHF equations. As a consequence of this non-linearity transition amplitudes that are obtained by projecting the propagated wave functions on final states oscillate in time even at asymptotically large distances [81]. These 'TDHF-oscillations' were first discussed in the context of ion–atom collisions in conjunction with TDHF calculations for proton impact on helium [81] and remained a concern in sub-

sequent calculations [44, 80, 82, 83].

A description of the electronic problem in a TDHF approach approximates electron-electron interactions and does not account for correlation. Correlation is typically defined indirectly, for example, by Löwdin [84] for a stationary problem: The correlation energy of helium is the difference between the ground state energy resulting from a Hartree–Fock (HF) calculation and that from the exact solution of the Schrödinger equation (SE) (cf. [85] for recent calculations). For the time-dependent case the definition of correlation is less clear [44, 86]. Stolterfoht[1] identified correlation as the difference between exact transition probabilities and those predicted by TDHF [44]. One problem with this definition is that the results of TDHF calculations often oscillate in time [83, 88]. For the present calculations correlation is not considered.

local potential approximations

Solving the TDHF equations (6) and (7) for the collision systems of interest with $N \geq 10$ is numerically expensive due to the non-local exchange terms. Approximations for the exchange terms are used to obtain single-electron equations that are easier to compute than the TDHF equations.

The two-centre exchange terms in both sets of equations are entirely omitted. Before the collision these terms vanish as long as the internuclear distance is large. As soon as the projectile and target get into close proximity and from then on this is not (necessarily) the case any more. The omission of the two-centre exchange terms is a source of error, in particular for the description of electron transfer [50]. The single-centre exchange term in the TDHF equations for target electrons (6) is approximated by a local potential $v_{\mathrm{ex}}^{\mathrm{t}}$, to be specified further below. With these approximations for the exchange

[1] According to Schaudt et al [44] published in [87].

terms and with the Hartree potential v_{Ha} of the form (8) the target TDHF equations (6) can be written in the form of a set of TDSEs,

$$\mathrm{i}\partial_t\, \theta_i(\boldsymbol{r},t) = \hat{h}_{\mathrm{t}}(\boldsymbol{r},t)\, \theta_i(\boldsymbol{r},t), \quad i = 1,\ldots,N_{\mathrm{t}}, \tag{9}$$

with the single-electron Hamiltonian,

$$\hat{h}_{\mathrm{t}}(\boldsymbol{r},t) = -\frac{1}{2}\Delta_{\boldsymbol{r}} - \frac{Z_{\mathrm{t}}}{r_{\mathrm{t}}} + v^{\mathrm{t}}_{\mathrm{Ha}}(\boldsymbol{r},t) + v^{\mathrm{t}}_{\mathrm{ex}}(\boldsymbol{r},t) - \frac{Z_{\mathrm{p}}}{r_{\mathrm{p}}} + v^{\mathrm{p}}_{\mathrm{Ha}}(\boldsymbol{r},t). \tag{10}$$

The exchange terms in the projectile TDHF equations (7) are approximated following the same concept, which leads to the projectile single-electron equations

$$\mathrm{i}\partial_t\, \phi_j(\boldsymbol{r},t) = \hat{h}_{\mathrm{p}}(\boldsymbol{r},t)\, \phi_j(\boldsymbol{r},t), \quad j = 1,\ldots,N_{\mathrm{p}}, \tag{11}$$

with the single-electron Hamiltonian

$$\hat{h}_{\mathrm{p}}(\boldsymbol{r},t) = -\frac{1}{2}\Delta_{\boldsymbol{r}} - \frac{Z_{\mathrm{p}}}{r_{\mathrm{p}}} + v^{\mathrm{p}}_{\mathrm{Ha}}(\boldsymbol{r},t) + v^{\mathrm{p}}_{\mathrm{ex}}(\boldsymbol{r},t) - \frac{Z_{\mathrm{t}}}{r_{\mathrm{t}}} + v^{\mathrm{t}}_{\mathrm{Ha}}(\boldsymbol{r},t). \tag{12}$$

As the wave functions are developed in time by different equations, either (9) or (11), they lose orthogonality. At some point the approach for the target and that for the projectile have to be combined; models to do this will be discussed in section 1.4. This discussion is easier when the approximations for the local potentials take a more concrete shape. For this it is convenient to define effective potentials for the target,

$$v^{\mathrm{t}}_{\mathrm{eff}}(\boldsymbol{r},t) = -\frac{Z_{\mathrm{t}}}{r_{\mathrm{t}}} + v^{\mathrm{t}}_{\mathrm{Ha}}(\boldsymbol{r},t) + v^{\mathrm{t}}_{\mathrm{ex}}(\boldsymbol{r},t), \tag{13}$$

and similarly for the projectile, $v^{\mathrm{p}}_{\mathrm{eff}}$. The following equally applies to the effective potentials of both centres, the distinction is given up in the notation, unless needed. Separated into a static and a dynamic

part,

$$v_{\text{eff}}(\boldsymbol{r}, t) = v^0_{\text{eff}}(\boldsymbol{r}) + \delta v_{\text{eff}}(\boldsymbol{r}, t), \tag{14}$$

the static potential $v^0_{\text{eff}}(\boldsymbol{r})$ can be identified as the ground-state potential of the respective atom or ion, because $\delta v_{\text{eff}}(\boldsymbol{r}, t_0) = 0$ at initial time. The ground-state potentials are discussed first, the time-dependence of the effective potentials and the approximations to deal with them will follow in section 1.3.

1.2 GROUND-STATE POTENTIALS

The effective potential v^0_{eff} is the ground-state potential of the undisturbed collision partner. The ground-state potentials of the target atom and dressed projectile ions used in the present work are numerical results of an optimized potential method (OPM) calculation [73]. Within a HF framework the OPM was developed by Talman and Shadwick [89].[2] It is an iterative method to find an effective local potential that is variationally optimized: Single-electron orbitals ψ_i are obtained from the stationary Schrödinger equation

$$\left[-\frac{1}{2}\Delta + v^0_{\text{eff}}(\boldsymbol{r})\right]\psi_i(\boldsymbol{r}) = \varepsilon_i \psi_i(\boldsymbol{r}) \tag{15}$$

with the effective potential v^0_{eff} in the Hamiltonian. The energy expectation value $\langle \hat{H} \rangle$ with regard to the Slater determinant of the ψ_i is minimized through variation of the effective potential. This yields the OPM equations, which are linear integral equations of the form

$$\int \mathrm{d}^3 r'\, K(\boldsymbol{r}, \boldsymbol{r}') v_{\text{ex}}(\boldsymbol{r}') = Q(\boldsymbol{r}), \tag{16}$$

where the kernel K and inhomogeneity Q are functionals of the orbitals and their energy eigenvalues (cf. reference [89], equations 3.5 and

[2] Also by Sharp and Horton [90] as an extension to a method developed by Slater [91]. The former apparently remained unnoticed for three decades.

3.7). In the case of degenerate orbitals of same ℓ quantum number, e.g. for closed-shell atoms, angular dependence can be eliminated, leading to radial OPM equations for the exchange potential $v_{\mathrm{ex}} = v^0_{\mathrm{eff}} - v_{\mathrm{Ha}} + Z/r$. In an iterative numerical process the OPM equations (16) and stationary Schrödinger equations (15) are solved for self-consistent orbitals ψ_i and effective potential v^0_{eff}. The self-consistent approach of reference [89] where the orbitals depend on a local potential has later been recognized as the exchange-only limit of the Kohn–Sham (KS) scheme [92] of density functional theory (DFT) [93]. An overview of the OPM within the framework of DFT can be found in references [73, 94–96]. When correlation is neglected (i.e. exchange-only) and the exact HF exchange functional is used, the DFT approach to OPM is identical to the HF approach by Talman and Shadwick.

Figure 2 shows the effective OPM ground-state potential for neon $v^0_{\mathrm{eff}}(r)$, and the potentials v_{Ha} and v_{ex} it includes. For small distances the effective potential approaches $-Z/r$ while for large distances r the effective potential is asymptotic to $-1/r$. At large distances the Hartree potential v_{Ha} approaches N_{Ne}/r, it compensates the nuclear Coulomb potential entirely (since $N_{\mathrm{Ne}} = Z = 10$). The asymptotic behaviour of the effective potential is thus determined by the exchange potential v_{ex} whose asymptotic limit is $-1/r$, since at large distances it compensates self-interaction included in the Hartree potential. The orbital structure is evident in the v_{ex} curve with a small oscillation in the transition region from the K to the L shell [95, 96], i.e. where the combined probability density of the L shell orbitals exceeds that of the $1s$ orbital.

1.3 TIME-DEPENDENT EFFECTIVE POTENTIALS

As the charge density of the atom or ion reacts to the passing collision partner the screening of the nucleus changes, and $\delta v_{\mathrm{eff}}(\boldsymbol{r}, t)$ deviates from zero in equation (14). An ideal way to deal with this

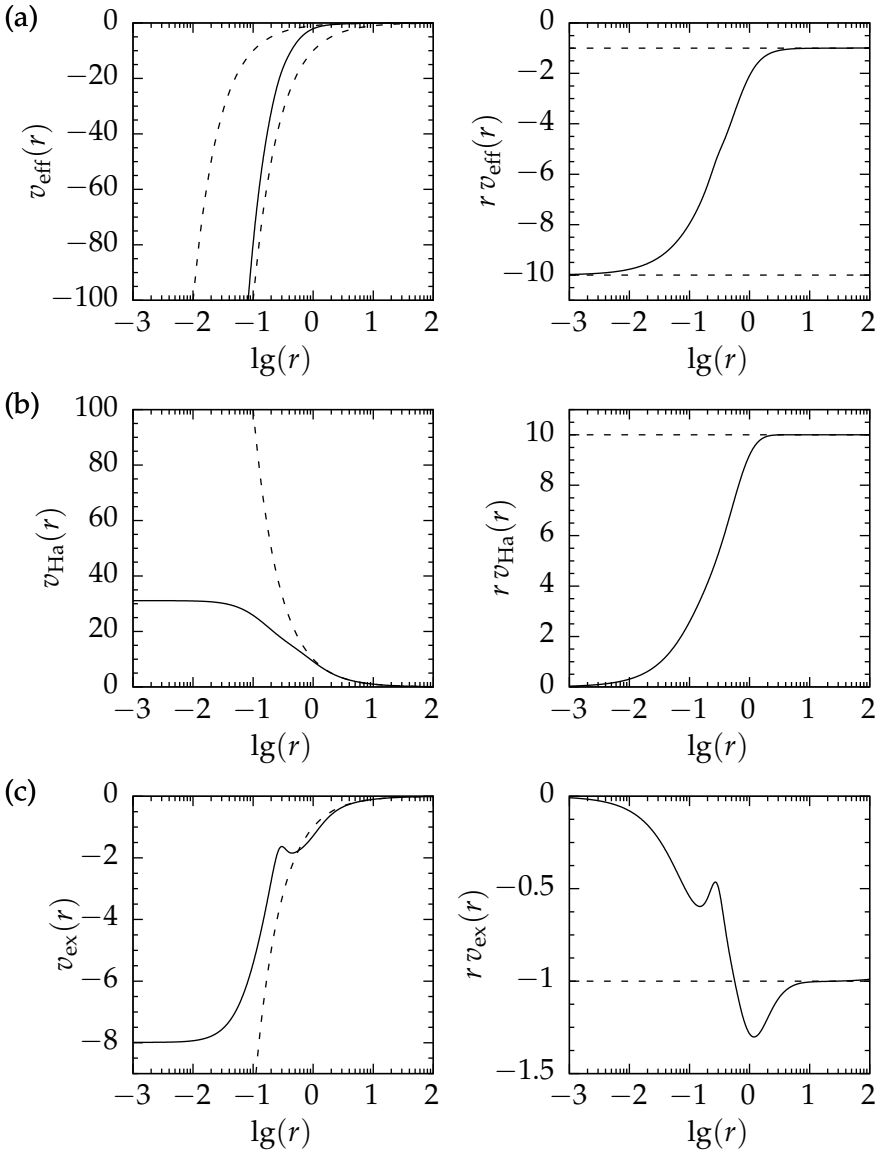

Figure 2: Neon ground-state effective potential $v^0_{\mathrm{eff}} = -10/r + v_{\mathrm{Ha}} + v_{\mathrm{ex}}$ (a), Hartree potential $v_{\mathrm{Ha}}(r)$ (b), and exchange potential $v_{\mathrm{ex}}(r)$ (c). The panels on the left-hand side show the potentials v, those on the right-hand side rv to emphasize the asymptotic behaviour. The potentials are shown as functions of the radius r (solid lines). As a reference, Coulomb potentials of relevant charges are also included in the plots (dashed lines).

problem would be to determine the effective potential at all times with a time-dependent OPM (TDOPM) approach [97]. However, this is presently computationally out of reach for the collision problems of interest in this work. For the helium atom in an exchange-only description the problem is simplified. The OPM equation (16) in a two-electron spin-singlet atom is reduced to a Poisson integral of the density $2|\psi(\boldsymbol{r},t)|^2$. In calculations for antiproton–helium collisions by Keim et al [98] the effective potential was determined at every time step by solving the Poisson equation with regard to the propagated states. These in turn were solutions of the TDSE that depends on the time-dependent effective potential. While the description of ionization could be improved in comparison to previous calculations [99], ensuring numerical stability proved rather difficult with this method [100].

In the present work the time dependence of the effective potentials is addressed in two much simpler ways: (i) the no-response approximation, $\delta v^{\mathrm{t}}_{\mathrm{eff}}(t) = \delta v^{\mathrm{p}}_{\mathrm{eff}}(t) = 0$, for all $t \in [t_0, t_{\mathrm{f}}]$; (ii) a target-response model, where $\delta v^{\mathrm{t}}_{\mathrm{eff}}$ is a function of a global observable while $\delta v^{\mathrm{p}}_{\mathrm{eff}} = 0$. In this approximation an angular-dependent response of the screening electron density is not considered, the target effective potential retains radial symmetry at all times.

1.3.1 *No-response approximation*

In the no-response approximation, $\delta v^{\mathrm{t}}_{\mathrm{eff}}(t) = \delta v^{\mathrm{p}}_{\mathrm{eff}}(t) = 0$, the effective potentials of target and projectile, respectively, are unchanged throughout the collision. While both effective potentials are independent of time in the reference frame of the respective centre, the single-electron Hamiltonian still remains time-dependent, due to the time-dependent geometry of the collision system. The problem is simplified by having to deal with radially symmetric potentials of frozen form and strength, where only the positions of the centres

change in time. Nonetheless, the no-response approximation is reasonable for collisions where the probability of electron removal is low, or in fast collisions $v_{\mathrm{rel}} \gg 1$ when the electronic charge density screening the nucleus has not enough time to react to the disturbance by the passing collision partner.

1.3.2 *Target-response approximation*

The present work uses the approach of reference [48] to model the response $\delta v^{\mathrm{t}}_{\mathrm{eff}}(r_{\mathrm{t}}, t)$: The ansatz is to approximate the effective potential (14) by a linear combination of ionic potentials $v_{q_{\mathrm{t}}}$ weighted with the probability $P^{\mathrm{t}}_{q_{\mathrm{t}}}(t)$ for the target to assume the charge state q_{t}:

$$v^{\mathrm{t}}_{\mathrm{eff}}(t) = \sum_{q_{\mathrm{t}}=0}^{N_{\mathrm{t}}} P^{\mathrm{t}}_{q_{\mathrm{t}}}(t)\ v^{\mathrm{t}}_{q_{\mathrm{t}}}. \tag{17}$$

To make the ansatz (17) viable the following conditions have to be met:

(i) $v^{\mathrm{t}}_0 = v^{0\,\mathrm{t}}_{\mathrm{eff}}$, since for the undisturbed atom $\delta v^{\mathrm{t}}_{\mathrm{eff}} = 0$;

(ii) removal of a single electron ought not reduce screening, $v^{\mathrm{t}}_1 = v^{0\,\mathrm{t}}_{\mathrm{eff}}$;

(iii) for a fully ionized target $v^{\mathrm{t}}_{N_{\mathrm{t}}}(r) = -Z_{\mathrm{t}}/r_{\mathrm{t}}$.

The rationale for condition (ii) can be found when considering single ionization in a naïve physical picture: As one electron is (re)moved from its centre it is subject to the Coulomb potential of the target nucleus screened by the remaining $N_{\mathrm{t}} - 1$ electrons. In other words, the active electron has to be subject to an effective potential that approaches $-1/r_{\mathrm{t}}$ for large r_{t} but does not reduce the screening due to removal of other electrons.

A more practical argument for condition (ii) comes from experience with TDHF investigations of single ionization where a frozen-TDHF approximation is preferable for the same reasons [48]. The

simplest model potential that meets the conditions is

$$v^{\mathrm{t}}_{q_\mathrm{t}} = v^{0\,\mathrm{t}}_{\mathrm{eff}} - \frac{q_\mathrm{t}-1}{N_\mathrm{t}-1}(v^{0\,\mathrm{t}}_{\mathrm{ex}} + v^{0\,\mathrm{t}}_{\mathrm{Ha}}) \quad \text{for } q_\mathrm{t} \geq 1. \tag{18}$$

Inserted in the sum (17),

$$v^{\mathrm{t}}_{\mathrm{eff}}(t) = v^{0\,\mathrm{t}}_{\mathrm{eff}} - (v^{0\,\mathrm{t}}_{\mathrm{ex}} + v^{0\,\mathrm{t}}_{\mathrm{Ha}}) \sum_{q_\mathrm{t}=2}^{N_\mathrm{t}} P^{\mathrm{t}}_{q_\mathrm{t}}(t) \frac{q_\mathrm{t}-1}{N_\mathrm{t}-1}, \tag{19}$$

the separation in a static and dynamic part, as in (14), becomes visible. While a statistical model is required to find the probabilities P_q, the net target occupation

$$P^{\mathrm{t}}_{\mathrm{net}} = N_\mathrm{t} - \sum_{q_\mathrm{t}=0}^{N_\mathrm{t}} q_\mathrm{t} P_{q_\mathrm{t}} \tag{20}$$

is a directly accessible observable (the weighted sum is an expression for the net electron removal). Extracting single-electron probabilities that sum up to $P^{\mathrm{t}}_{\mathrm{net}}$ requires further considerations that will be discussed in section 1.5. The effective potential can be expressed with the net occupation [48],

$$v^{\mathrm{t}}_{\mathrm{eff}}(t) = -\frac{Z_\mathrm{t}}{r_\mathrm{t}} + a(t)\,\left(v^{0\,\mathrm{t}}_{\mathrm{ex}} + v^{0\,\mathrm{t}}_{\mathrm{Ha}}\right), \tag{21}$$

where

$$a(t) = \frac{P^{\mathrm{t}}_{\mathrm{net}}(t) - \left(P^{\mathrm{t}}_{\mathrm{net}}(t)/N_\mathrm{t}\right)^{N_\mathrm{t}}}{N_\mathrm{t}-1}. \tag{22}$$

The second term in the numerator of (22), $\left(P^{\mathrm{t}}_{\mathrm{net}}(t)/N_\mathrm{t}\right)^{N_\mathrm{t}}$, can be interpreted as the probability that no electrons are removed from the atom; for it to be meaningful $P^{\mathrm{t}}_{\mathrm{net}}(t)$ must not exceed the number of electrons at the target N_t. In a collision with a projectile that carries electrons into the collision it is possible that capture from the projectile indeed causes $P^{\mathrm{t}}_{\mathrm{net}} > N_\mathrm{t}$. However, it happens so rarely that it

can be safely neglected by truncating $P^{\mathrm{t}}_{\mathrm{net}}$ at N_{t}.

1.4 COMBINING THE TARGET AND PROJECTILE PROBLEMS

With the response approximations of section 1.3 based on the ground-state potentials of section 1.2 the single-electron target Hamiltonian (10) takes a more concrete form,

$$\hat{h}_{\mathrm{t}}(\boldsymbol{r},t) = -\frac{1}{2}\Delta_{\boldsymbol{r}} - \frac{Z_{\mathrm{t}}}{r_{\mathrm{t}}} - \frac{Z_{\mathrm{p}}}{r_{\mathrm{p}}} + a\left[v^{\mathrm{t}}_{\mathrm{ex}}(r_{\mathrm{t}}) + v^{\mathrm{t}}_{\mathrm{Ha}}(r_{\mathrm{t}})\right] + v^{\mathrm{p}}_{\mathrm{Ha}}(r_{\mathrm{p}}), \quad (23)$$

where the screening factor is either $a = 1$ in case of the no-response approximation, or given by (22) for the target-response model. Including the single-electron projectile Hamiltonian (12) in a description that considers active electrons at both centres can be done in several ways:

(i) The *coupled–mean-field* approach of [50] propagates the target and projectile electrons by solving the single-electron equations (9) and (11) in independent calculations. To consider response for the potential screening the target would couple the calculations through the target Hartree potential in the projectile Hamiltonian (12). While response was considered in the He^+–Ne calculations of [50] for the target Hamiltonian (23), it did not apply to the single electron of the projectile. In subsequent work for C^{3+}-ion impact on neon [52] the no-response approximation was used for the projectile Hamiltonian

$$\hat{h}_{\mathrm{p}}(\boldsymbol{r},t) = -\frac{1}{2}\Delta_{\boldsymbol{r}} + v^{0\,\mathrm{p}}_{\mathrm{eff}}(r_{\mathrm{p}}) - \frac{Z_{\mathrm{t}}}{r_{\mathrm{t}}} + v^{0\,\mathrm{t}}_{\mathrm{Ha}}(r_{\mathrm{t}}). \quad (24)$$

The coupled–mean-field method has the disadvantage that the orthogonality of the propagated target and projectile wave functions is lost [50]. When combining the results of the calculations for each collision centre at the stage of the final-state ana-

lysis the non-orthogonality of orbitals leads to a noticeable error [51]. This was overcome by renormalization of the many-electron wave function [51].

Advantages of the coupled–mean-field approach are: Before the collision the electrons of both centres are subject to potentials with the correct asymptotic behaviour at large distances. From the point of view of a projectile electron the target atom's nucleus is entirely screened by its electrons at asymptotic distances. Self interaction at large distances is compensated for active projectile electrons, the effective potential is thus asymptotic to $-(q_\mathrm{p}+1)/r_\mathrm{p}$.

(ii) In the *common–mean-field approach* electrons of the target and the projectile are propagated with the same Hamiltonian. Giving up the nomenclature that distinguishes between target and projectile wave functions introduced at the beginning of this chapter, such that $\left|\Psi\right\rangle = \left|\psi_1 \cdots \psi_N\right\rangle \equiv \left|\theta_1 \cdots \theta_{N_\mathrm{t}}\, \phi_1 \cdots \phi_{N_\mathrm{p}}\right\rangle$, the single-electron equations (9) and (11) can be summarized as

$$\mathrm{i}\partial_t\, \psi_i(\boldsymbol{r},t) = \hat{h}(\boldsymbol{r},t)\, \psi_i(\boldsymbol{r},t), \quad i = 1,\ldots,N, \tag{25}$$

where the common single-electron Hamiltonian is chosen as $\hat{h} \equiv \hat{h}_\mathrm{t}$ (23). Unlike in the coupled–mean-field approach the orthogonality of the propagated wave functions is retained. Unfortunately, this comes at a price, projectile electrons are subject to potentials with decidedly wrong behaviour at asymptotic distances before the collision. Namely, the target atom does not appear neutral at a large distance, its potential is asymptotic to $-1/r_\mathrm{t}$, which is a consequence of the target exchange potential v_ex^t compensating the self-interaction of target electrons. Likewise, the projectile ion does not appear attractive enough to a projectile electron, as the projectile exchange potential v_ex^p is not

included. Self interaction is not compensated at large distances and the effective potential goes asymptotically to $-q_\mathrm{p}/r_\mathrm{p}$. This choice of Hamiltonian is not without alternative for a common–mean-field description, nonetheless, it is a good choice for the present ion-neon collision calculations where $N_\mathrm{t} > N_\mathrm{p}$. The main interest in these collisions are target electron removal processes; a less accurate representation of projectile electron processes is a concession that can be made.

(iii) When target and projectile exchange terms are modeled with the help of a piecewise function in a common Hamiltonian it is possible to keep orthogonality of the propagated states of both centres and the correct asymptotic behaviour of the overall potentials before the collision.

The coupled–mean-field model (i) was used in several previous works [51, 101, 102] and serves as a reference here, however, no calculations are performed with this approach in the present work. The asymptotic correction approach (iii) brings its own complications and is discussed in more detail in chapter 6. In the following the discussion continues with the *common–mean-field* model (ii), where the single-electron target and projectile wave functions are propagated with the single-electron equations (25) and the Hamiltonian $\hat{h} \equiv \hat{h}_\mathrm{t}$ (23).

Single-electron transition amplitudes

$$c_i^\nu = \langle \varphi_\nu | \psi_i \rangle \tag{26}$$

quantify, through $p_i^\nu = |c_i^\nu|^2$, the probability for an electron corresponding to an initial condition i to be found in a bound state $\left|\varphi_\nu\right\rangle$ of the target, $\{\left|\varphi_\nu\right\rangle | 1 \le \nu \le K_\mathrm{t}\}$, or the projectile, $\{\left|\varphi_\nu\right\rangle | K_\mathrm{t} < \nu \le K\}$ after the collision. The K target and projectile bound states are, somewhat arbitrarily, ordered with K_t target states first, followed by K_p projectile states. The single-electron probabilities for the ith active electron to occupy a target state, a projectile state, or to be found in the continuum are, respectively,

$$p_i^\mathrm{t} = \sum_{\nu=1}^{K_\mathrm{t}} |c_i^\nu|^2, \qquad p_i^\mathrm{p} = \sum_{\nu=K_\mathrm{t}+1}^{K} |c_i^\nu|^2, \qquad p_i = 1 - \sum_{\nu=1}^{K} |c_i^\nu|^2 = 1 - p_i^\mathrm{t} - p_i^\mathrm{p}. \tag{27}$$

In the IEM many-electron probabilities require statistical models, which will be discussed in chapter 3. Net probabilities are sums of single-electron probabilities and directly accessible. The target net occupation is

$$P_\mathrm{net}^\mathrm{t} = \sum_{i=1}^{N} \sum_{\nu=1}^{K_\mathrm{t}} |c_i^\nu|^2, \tag{28}$$

while the projectile net occupation $P_\mathrm{net}^\mathrm{p}$ is defined correspondingly.

In the no-response approximation, $\delta v_\mathrm{eff} = 0$, and at final time the bound target and projectile eigenstates $|\varphi_\nu\rangle$ in (26) are identical to the initial eigenstates $|\varphi_\nu^0\rangle$ defined by

$$\left[-\frac{1}{2}\Delta_{r_\mathrm{t}} + v_\mathrm{eff}^{0\,\mathrm{t}}(r_\mathrm{t})\right] \varphi_\nu^0(r_\mathrm{t}) = \epsilon_\nu^0 \, \varphi_\nu^0(r_\mathrm{t}) \quad \text{for } \nu = 1, \ldots, K_\mathrm{t} \tag{29}$$

and

$$\left[-\frac{1}{2}\Delta_{r_\mathrm{p}} + v_\mathrm{eff}^{0\mathrm{p}}(r_\mathrm{p})\right]\varphi_\nu^0(r_\mathrm{p}) = \epsilon_\nu^0\,\varphi_\nu^0(r_\mathrm{p}) \quad \text{for } \nu = K_\mathrm{t}+1,\ldots,K. \tag{30}$$

In the case of the neutral target atom the first N_t eigenstates are equivalent to the $\left|\psi_i(t=t_0)\right\rangle$, for $i = 1,\ldots,N_\mathrm{t}$, and likewise for the first N_p projectile states.

The eigenfunctions of equations (29) and (30) are physically meaningful in the no-response approximation whenever the internuclear distances are sufficiently large to ensure undisturbed single-centre systems; in particular at final time t_f, where a statistical final-state analysis is conducted to obtain results. In the case of the global target-response approximation (cf. section 1.3.2) two complications arise: (i) The initial eigenstates $\left|\varphi_\nu^0\right\rangle$ of the target atom are not eigenstates of an ionized target. (ii) Unlike in the no-response case probabilities need to be extracted at all times, not just for the final-state analysis (cf. equation (22)). However, the interpretation of the single-electron transition amplitudes (26) as contributions to net probabilities (28) becomes questionable when target and projectile are in close proximity.

The first issue leads to oscillations of extracted probabilities in time, and has been identified in TDHF calculations [82, 83] and more recent calculations using the same framework as the present work [48, 98]. An ansatz to avoid it is to find instantaneous eigenstates $\left|\varphi_\mathrm{t}(t)\right\rangle$ of the Hamiltonian at all times [48]

$$\left[-\frac{1}{2}\Delta_{r_\mathrm{t}} + v_\mathrm{eff}^{\mathrm{t}}(r_\mathrm{t},t)\right]\varphi_\nu(r_\mathrm{t},t) = \epsilon_\nu(t)\varphi_\nu(r_\mathrm{t},t) \quad \text{for } \nu = 1,\ldots,K_\mathrm{t}, \tag{31}$$

and define transition amplitudes (26) with respect to these states. This approach has been used in several works with the BGM [48, 49, 51, 103], however, not yet in the two-centre BGM framework used in the present work. The present results have been obtained by us-

ing initial atomic eigenstates $\left|\varphi_t^0\right\rangle$. The inaccuracies caused by the oscillations are evaluated in section 4.2. The second complication is inherent in the present target-response model, as it depends on the occupation of target states (22). This is problematic when target and projectile are in close proximity where the physical significance of initial eigenstates (29) and instantaneous eigenstates (31) is questionable.

2 BASIS GENERATOR METHOD

2.1 BASIS EXPANSION

In the common–mean-field description the time development of the N-electron system is described by the single-electron equations (25) with the single-electron Hamiltonian (23). In the following it is assumed that the Hamiltonian can be separated,

$$\hat{h} = \hat{h}_0 + \hat{v}(t), \tag{32}$$

into a stationary part $\hat{h}_0$ and a time-dependent external potential $\hat{v}(t)$ that vanishes for asymptotic times. In the following notation the $\boldsymbol{r}$ and t dependence is implicit. Since the propagated wave functions do not differ for either spin the single-electron equations have to be solved for odd values of the index i only. By defining the Schrödinger operator

$$\hat{O} = \hat{h} - \mathrm{i}\partial_t \tag{33}$$

the single-electron equations (25) can be written as

$$\hat{O}\big|\psi_i\big\rangle = 0. \tag{34}$$

The single-electron equations (34) are solved with a basis expansion approach. Several intermediate steps that lead towards the basis expansion used in the present calculations are described in the following. Let's assume each propagated state is expressed as a linear

combination

$$|\psi_i\rangle = \sum_j c_{ij} |\xi_j\rangle \tag{35}$$

of states that form the orthogonal basis $\{|\xi_j\rangle\}$. The coefficients are $c_{ij} = \langle \xi_j \mid \psi_i \rangle$. Substituting the propagated state in the TDSE (34) with (35) leads to the coupled-channel equations

$$\mathrm{i}\dot{c}_{ik} = \sum_j c_{ij} \langle \xi_k \mid \hat{O} \mid \xi_j \rangle, \tag{36}$$

where time dependence of the basis states $|\xi_j\rangle$ is allowed.

2.2 FINITE BASIS, OPTIMIZED MODEL SPACE

The equations (36) are exact for a complete basis $\{|\xi_j\rangle\}$, however, to solve the problem numerically only a truncated basis can be used. Such a finite basis $\{|\xi_j\rangle | \, j = 1, \ldots, J\}$ spans a model space $\mathcal{A}$. Even when the solutions are contained at a point in time in this model space (e.g. for a system in the ground state) this cannot be ensured in general as the system develops in time. The coupled-channel equations couple to the subspace $\mathcal{B}$ which is complementary to the model space $\mathcal{A}$. An approach to quantify the coupling to $\mathcal{B}$ is developed in [104] along the lines of the optical potential method of Feshbach [105].

The propagated state $|\psi_i\rangle$ can be separated into components of each subspace (i is understood unless needed),

$$|\psi\rangle = \hat{A}|\psi\rangle + \hat{B}|\psi\rangle = |\psi^{\mathcal{A}}\rangle + |\psi^{\mathcal{B}}\rangle, \tag{37}$$

where the idempotent and hermitian operators $\hat{A}$ and $\hat{B}$ are projectors on the model space $\mathcal{A}$ and the complementary space $\mathcal{B}$, respectively. Thus, $\hat{A} + \hat{B} = \hat{1}$ and $\hat{A}\hat{B} = \hat{B}\hat{A} = 0$. With (37) the TDSE (34)

can be written as

$$\hat{A}\,\hat{O}\,\hat{A}\big|\psi^{\mathcal{A}}(t)\big\rangle = -\hat{A}\,\hat{O}\,\hat{B}\big|\psi^{\mathcal{B}}(t)\big\rangle, \tag{38}$$

$$\hat{B}\,\hat{O}\,\hat{B}\big|\psi^{\mathcal{B}}(t)\big\rangle = -\hat{B}\,\hat{O}\,\hat{A}\big|\psi^{\mathcal{A}}(t)\big\rangle. \tag{39}$$

The expression on the right hand side of the model-space equation (38) couples to the complementary space. One could use a rather direct approximation, neglect the coupling and solve $\hat{A}\,\hat{O}\,\hat{A}\big|\psi^{\mathcal{A}}(t)\big\rangle = 0$. However, the probability flux due to the coupling term is very sensitive to the choice of basis for a physical situation [104]. This usually requires a large basis and makes convergence of the results with respect to the basis choice not very predictable [106]. To go beyond this approximation the coupling term in (38) is to be expressed in terms of states in the model space $\big|\psi^{\mathcal{A}}\big\rangle$. This can be done with the help of the propagator $\hat{B}(t,t')$, which is defined such that for $t' = t$ it is the projector on the complementary space $\mathcal{B}$, $B(t) = B(t,t)$, and it satisfies $\hat{B}(t)\,\hat{O}\,\hat{B}(t,t') = 0$. With the propagator the solution for the $\mathcal{B}$-space equation (39) can be written as [107, 108]:

$$\big|\psi^{\mathcal{B}}(t)\big\rangle = -\mathrm{i}\int_{t_0}^{t} \mathrm{d}t\,\hat{B}(t,t')\,\hat{O}(t')\big|\psi^{\mathcal{A}}(t')\big\rangle. \tag{40}$$

In other words, the propagator $\hat{B}(t,t')$ is responsible for the time development of the part of the solution which is lost by truncating the basis, namely $\big|\psi^{\mathcal{B}}\big\rangle$. With (38) and (40) coupled-channel equations can be found that are, up to a coupling term[1] that is non-local in

[1] With (40) the right-hand side of (38) can be expressed as $\hat{A}\,\hat{O}\,\hat{A}\big|\psi^{\mathcal{A}}(t)\big\rangle = \hat{V}_{\mathrm{opt}}\big|\psi^{\mathcal{A}}(t)\big\rangle$, where the optical potential $\hat{V}_{\mathrm{opt}}$ is non-local in time and defined by

$$\hat{V}_{\mathrm{opt}}\big|\psi^{\mathcal{A}}(t)\big\rangle = \mathrm{i}\hat{A}(t)\,\hat{O}(t)\int_{t_0}^{t}\mathrm{d}t'\,\hat{B}(t,t')\,\hat{O}(t')\big|\psi^{\mathcal{A}}(t')\big\rangle.$$

time, similar to (36) [108]:

$$\begin{aligned} \mathrm{i}\dot{c}_{ik} = &\sum_{j=1}^{J} c_{ij} \langle \xi_k \mid \hat{O} \mid \xi_j \rangle \\ &- \mathrm{i} \sum_{j=1}^{J} \int_{t_0}^{t} \mathrm{d}t' \, c_{ij}(t') \langle \xi_k(t) | \, \hat{O}(t) \hat{B}(t,t') \, \hat{O}(t') \, | \xi_j(t') \rangle . \end{aligned} \tag{41}$$

The optimized model space concept of [108] is to construct a basis that changes in time such that the coupling between the sub spaces is minimized. It was shown that a basis can be constructed hierarchically in such a way that the coupling term disappears for all but the highest hierarchy levels. A set of eigenfunctions $\{\phi_1^0, \ldots, \phi_K^0\}$ of the unperturbed Hamiltonian of the collision system $\hat{h}_0$ (32) forms the base of the hierarchy. All other basis states are defined by the recursion relation

$$|\phi_v^u\rangle = \hat{O} |\phi_v^{u-1}\rangle . \tag{42}$$

While the basis $\{|\phi_v^u\rangle\}$ is not orthonormal, the basis functions can be shown to be linear independent [108]. Expressed in this basis the coupled-channel equations (41) that describe the time development of each single-electron wave function ψ_i are

$$\begin{aligned} \mathrm{i} \sum_{u=0}^{U} \sum_{v=0}^{V} \dot{c}_v^u \langle \phi_{v'}^{u'} \mid \phi_v^u \rangle = &\sum_{u=0}^{U} \sum_{v=0}^{V} c_v^u \langle \phi_{v'}^{u'} \mid \hat{O} \mid \phi_v^u \rangle \\ &- \mathrm{i} \sum_{u=0}^{U} \sum_{v=0}^{V} \int_{t_0}^{t} \mathrm{d}t' \, c_{uv}(t') \langle \phi_v^{u+1}(t) | \hat{B}(t,t') | \phi_v^{u+1}(t') \rangle \end{aligned} \tag{43}$$

(as above, the index i is understood). For all basis states below the highest hierarchy level, $u < U$, projection on the complementary space is $\hat{B}|\phi_v^{u+1}\rangle = 0$; the coupling term vanishes. For the highest hierarchy level the projection is $\hat{B}|\phi_v^{U+1}\rangle = |\phi_v^{U+1}\rangle$. Based on this

argument it was also shown that, orthogonalized states of one hierarchy level only couple to the next higher level [108]. The population of states decreases with increasing hierarchy level u as more and more interactions are required to populate each level. One can expect an approximation where the coupling term is omitted to become more accurate as more hierarchy levels U are included.

Due to the recursion relation (42) the complexity of basis states grows quickly with increasing u, which makes direct application of this approach not practical for $u > 1$. A first approximative approach was explored in [109] wherein u in (42) is limited to a maximum of 1. It was realized in calculations for one-electron collision systems [45].

2.3 BASIS GENERATION

The rapidly increasing complexity due to the recursive construction principle (42) can be avoided altogether with a slight change of the premise of the ansatz: Instead of generating a basis that forms the described optimized model space, a model space that is larger and contains the optimized model space at all times is spanned by basis states that are easier to generate. Such a BGM approach is described in detail in [46]. However, for a practical implementation, as used to calculate the present results, a number of approximations are needed. In the following the theory will be summarized quite coarsely, leaping, for example, from requirements for BGM basis states to the states that are used as approximations.

The basis $\left\{\chi_\nu^\mu(t) \;\middle|\; \nu = 1,\ldots,K,\ \mu = 0,\ldots,M_\nu\right\}$ is defined to span the space $\mathcal{A}'$ that contains the optimized model space of section 2.2: $\mathcal{A}' \supseteq \mathcal{A}$ at all times [46]. For the basis to have this property it is sufficient that two requirements are met [46]: the physical initial condition (i.e. the initial states $|\psi_i(t_0)\rangle = |\varphi_\nu^0\rangle$) must be contained in the basis, and $(\hat{h} - \mathrm{i}\partial_t)|\chi_\mu^\nu\rangle$ must be expressible as a linear combination of basis states $|\chi_{\nu'}^{\mu'}\rangle$. The ansatz of [46] for a construction principle to

generate such a basis $\{\chi_\nu^\mu\}$ is:

$$\left|\chi_\nu^\mu\right\rangle = \hat{W}(t)\left|\chi_\nu^{\mu-1}\right\rangle, \tag{44}$$

where $\hat{W}$ is a regularized potential that corresponds to the external potential $\hat{v}(t)$ in (32); it will be specified below. Reference [46] showed for a specific Hamiltonian and a specific operator $\hat{W}$ that with χ_ν^0 that resemble spherical Slater-type orbitals the basis generated with (44) meets the conditions. As an approximation to these orbitals the basis is directly generated from eigenfunctions φ_ν^0 of the system in the ground state (29, 30). Since (29) and (30) are in the frame of the respective collision centre, translation factors have to be taken into account for the zeroth order of the basis [74, 106]

$$\chi_\nu^0(\boldsymbol{r}) = \begin{cases} \varphi_\nu^0(\boldsymbol{r}_\mathrm{t}) e^{\mathrm{i}\boldsymbol{v}_\mathrm{t}\boldsymbol{r}} & \text{for } \nu \leq K_\mathrm{t} \\ \varphi_\nu^0(\boldsymbol{r}_\mathrm{p}) e^{\mathrm{i}\boldsymbol{v}_\mathrm{p}\boldsymbol{r}} & \text{for } K_\mathrm{t} < \nu \leq K \end{cases} \tag{45}$$

where $\boldsymbol{v}_\mathrm{t}$ and $\boldsymbol{v}_\mathrm{p}$ (1) are the velocities of each centre with respect to the centre of mass. In the BGM as it was initially developed in [46], and implemented in a number of works, for example, [47–51, 103, 110, 111], only target states were included in the basis, the inclusion of states of both centres in (45) is the central aspect of the extension of the method, namely, the two-centre BGM (TC-BGM), introduced in [74]. BGM calculations where the two-centre extension of the method are (were) not used are referred to as OC-BGM. In general, the present results were calculated with the TC-BGM.[2]

Basis size and structure are set by the choice of the number of generating basis states K and the maximum hierarchy levels $M_1, \ldots, M_K$ (see section 4.1 for concrete values). While (45) includes target and projectile states in the $\mu = 0$ order of the BGM basis, the higher

[2] There is one exception, response test calculations shown in section 4.2 use the OC-BGM rather than the TC-BGM.

hierarchies are only generated (44) from either target or projectile states.[3] For the present problems no states are generated from projectile states, namely, for $\nu > K_\mathrm{t}$ $M_\nu = 0$.

A basis generated from the $|\chi_\nu^0\rangle$ (45) cannot guarantee that the space it spans always contains the optimized model space and that the decoupling of lower hierarchy states from the complementary space is retained – unlike a basis that is constructed strictly in accordance with the requirements stated above. Nonetheless, atomic eigenstates $|\varphi_\nu^0\rangle$ are used as practical approximations to states that meet the stricter requirements – one can expect a basis that is still well-adapted to the problem. Convergence of numerical results with respect to the basis size and structure becomes the criterion to evaluate the approximation.

The choice to build the higher hierarchy levels of the model space solely from target orbitals suggests to use a generating potential $\hat{W}$ in (44) that corresponds to the projectile potential. It has emerged from earlier BGM calculations [47–51, 103, 110, 111] that good results can be obtained with the method when the generating potential shows the $1/r_\mathrm{p}$ Coulomb tail of the projectile, such as the regularized potential [107]

$$W_\mathrm{p} = \frac{\left(1 - \mathrm{e}^{-\alpha r_\mathrm{p}}\right)}{r_\mathrm{p}}, \tag{46}$$

with the regularisation parameter $\alpha = 1$.[4] Since the basis is generated (44) with an operator $\hat{W}_\mathrm{p}$, which corresponds to the projectile potential, applied on target states $\{|\chi_\nu^0\rangle | \nu = 1, \ldots, K_\mathrm{t}\}$, the model space it spans is optimized for describing transitions of target electrons. The reasons from section 1.4 for prioritising target electrons

[3] In an extension to the TC-BGM a basis has been built from generating states of both centres. This method has been used in calculations of the $(\mathrm{He\,H})^{2+}$ quasi molecule in an intense laser field [112].

[4] A different regularisation, of the form $(r^2 + \varepsilon^2)^{-1/2}$, was proposed in [46]. However, no sufficient convergence could be attained in the range of possbile ε values [107].

in (25) apply here as well. The regularized potential W_{p} is used in (44) only, and not in the single-electron equations (25), where the unchanged nuclear Coulomb potential is part of $v_{\mathrm{eff}}^{\mathrm{p}}$. With the single-electron states expanded in the BGM basis

$$\big|\psi_i(t)\big\rangle = \sum_{\nu=1}^{K} \sum_{\mu=0}^{M_\nu} c_{\mu\nu}^{i}(t) \big|\chi_\nu^\mu(t)\big\rangle \tag{47}$$

the single-electron equations (25) with the Hamiltonian (23) can be solved through the coupled-channel equations

$$\mathrm{i} \sum_{\nu=1}^{K} \sum_{\mu=0}^{M_\nu} \dot{c}_{\mu\nu}^{i}(t) \big\langle \chi_{\nu'}^{\mu'} \,\big|\, \chi_\nu^\mu \big\rangle = \sum_{\nu=1}^{K} \sum_{\mu=0}^{M_\nu} c_{\mu\nu}^{i}(t) \big\langle \chi_{\nu'}^{\mu'} \,\big|\, \hat{h} - \mathrm{i}\partial_t \,\big|\, \chi_\nu^\mu \big\rangle. \tag{48}$$

These equations can be written in matrix-vector form

$$\mathrm{i} S \dot{\boldsymbol{c}}_i = M \boldsymbol{c}_i \tag{49}$$

where $\boldsymbol{c}_i$ is a vector with components $c_{\mu\nu}^{i}$, S is the overlap matrix, and M the Schrödinger matrix. The matrix elements are

$$S_{\nu'\nu}^{\mu'\mu} = \big\langle \chi_{\nu'}^{\mu'} \,\big|\, \chi_\nu^\mu \big\rangle, \tag{50}$$

$$M_{\nu'\nu}^{\mu'\mu} = \big\langle \chi_{\nu'}^{\mu'} \,\big|\, \hat{h} - \mathrm{i}\partial_t \,\big|\, \chi_\nu^\mu \big\rangle. \tag{51}$$

The computation of these matrix elements is involved. Several transformations of the matrices are needed to make the problem manageable, these are described in references [106, 113] for the TC-BGM.

The basis constructed from atomic eigenstates with (44) and the potential (46) is not orthogonal. Orthogonality of the generated states $\big|\chi_\nu^\mu\big\rangle$ for $\mu > 0$, with the atomic eigenstates is required for a straightforward final-state analysis. Accordingly, an orthogonalisation of the generated states is performed during basis generation [107].

As in section 1.5 where the extraction of probabilities from the single-electron equations is described, single-electron transition amplitudes result from the time-development of the problem. Expressed in the (orthogonalized) BGM basis the transition amplitudes are (26)

$$c_i^\nu = \sum_{\nu'}^{K} \sum_{\mu'_\nu}^{M_\nu} c^i_{\mu'\nu'} \langle \varphi_\nu \mid \chi^{\mu'}_{\nu'} \rangle. \tag{52}$$

For the no-response approximation (cf. s. 1.3.1) and when projecting on initial eigenstates $|\varphi^0_\nu\rangle$ (29, 30) in the target-response model, the transition amplitudes are identical to the coefficients in the coupled-channel equations (48),

$$c_i^\nu = c^i_{\mu\nu}\big|_{\mu=0}. \tag{53}$$

3 STATISTICAL FINAL-STATE ANALYSIS

While single-electron probabilities and net probabilities, such as the target net occupation $P_{\text{net}}^{\text{t}}$, can be obtained immediately from the results of the BGM calculation, statistical models are needed to investigate multi-electron processes. The starting point for these models are the transition amplitudes c_i^ν (26) extracted at final time by projecting the propagated states $|\psi_i(t)\rangle$ on bound target or projectile states $|\varphi_\nu^0\rangle$ (29, 30).

The objective of a statistical final-state analysis are observables that can be directly compared with experiments. In this work only total cross sections

$$\sigma = 2\pi \int_0^\infty b \; p(b) \, \mathrm{d}b, \tag{54}$$

are used in comparison with experiments, mostly as functions of the projectile kinetic energy E. The probabilities required in (54) are calculated in three ways: from sums of single-electron probabilities; from inner products of the Slater determinants of the many-electron state at final time and specific final configurations; and from multinomial combination of single-electron probabilities.

The net recoil ion production is a net cross section that can be directly calculated from the target net occupation $P_{\text{net}}^{\text{t}}$ (28):

$$\sigma_+ = 2\pi \int_0^\infty b \big[N_{\text{t}} - P_{\text{net}}^{\text{t}}(b) \big] \, \mathrm{d}b \, . \tag{55}$$

As a quantity that depends in experiments on the total charge of re-

coiling ionized target atoms and on beam properties[1] the net recoil ion production was early accessible in experiments [114–116] and thus much experimental data is available [13]. A weighted sum of total cross sections to yield recoil ions of charge state q_t is an equivalent expression [68],

$$\sigma_+ = \sum_{q_\mathrm{t}=1}^{N_\mathrm{t}} q_\mathrm{t} \sigma_{q_\mathrm{t}}. \tag{56}$$

More interesting in the context of this work are the total cross sections σ_{kl} that discriminate between the final charge states of both collision partners. The naming convention has been carried over from bare-ion impact calculations: k denotes the number of electrons that are found at the projectile; l denotes those in the continuum. Accordingly, the charge states are $q_\mathrm{t} = k - N_\mathrm{p} + l$ and $q_\mathrm{p} = Z_\mathrm{p} - k$. The cross sections σ_{q_t} and σ_{kl} are obtained via (54) from probabilities found with the statistical final-state analyses described in the following.

3.1 DETERMINANTAL ANALYSIS

In the present IEM description the many-electron wave function at final time $\Psi(t_\mathrm{f})$ is expressed as a Slater determinant (4), the associated many-electron state is denoted as $|\psi_1, \ldots, \psi_N, t_\mathrm{f}\rangle$. In the following the probability to find the collision system in a specific final configuration is called *exclusive probability*. For a final configuration $|f_1 \ldots f_N\rangle$, which is also expressed as a Slater determinant, this probability is

$$P_{f_1,\ldots,f_N} = \left|\langle \psi_1, \ldots, \psi_N, t_\mathrm{f} \mid f_1, \ldots, f_N \rangle\right|^2. \tag{57}$$

[1] In experiments the net recoil ion production σ_+ is proportional to the ratio of the total charge Q_total of the recoil ions produced by a beam of N_beam particles, $\sigma_+ \propto Q_\mathrm{total}/N_\mathrm{beam}$ [13].

Equation (57) can be expressed as

$$P_{f_1,\ldots,f_N} = \det \boldsymbol{\gamma} \tag{58}$$

where $\boldsymbol{\gamma}$ is the one-particle density matrix with the matrix elements

$$\gamma_{mn} = \sum_{i=1}^{N} \langle f_m \mid \psi_i \rangle \langle \psi_i \mid f_n \rangle. \tag{59}$$

The inner products of f_j and ϕ_i are identical to the transition amplitudes c_i^ν (26) if f_j is a bound target or projectile state φ_ν^0. Thus the matrix elements of the one-particle density matrix are

$$\gamma_{mn} = \sum_{i=1}^{N} c_i^m c_i^{n*}. \tag{60}$$

In contrast to the exclusive probability the probability to find the system in any configuration that fits a given criterion is called *inclusive probability*. An example for the latter is the probability P_{kl} to find k electrons at the projectile and l electrons in the continuum. Inclusive probabilities can be obtained by summation of all exclusive probabilities that correspond to many-electron states that fit the pattern. For example, adding all $P_{f_1,\ldots,f_N}$ for which $N-k-l$ of the f_j correspond to $\{\varphi_1,\ldots,\varphi_{K_t}\}$ and k of the f_j correspond to $\{\varphi_{K_t+1},\ldots,\varphi_K\}$ results in P_{kl}. Such a procedure is not very practical for collision problems with many electrons as in the present work, namely, $N \geq 10$.

The simplest example for an inclusive probability is one where $N-1$ electrons occupy a specific final state each, while the remaining electron can be in any other, unoccupied, state:

$$P_{f_1,\ldots,f_{N-1}} = \sum_{f_N} P_{f_1,\ldots,f_N}\,. \tag{61}$$

More generally, the inclusive probability to find u electrons in given

states and $N-u$ electrons in any other state, namely, $N-u$ electrons are not measured, is

$$P_{f_1,\ldots,f_u} = \sum_{f_{u+1}<\cdots<f_N} P_{f_1,\ldots,f_N}. \tag{62}$$

Reference [75] shows that the determinant of a reduced density matrix of dimension $u \times u$ is an equivalent description for this inclusive probability,

$$P_{f_1,\ldots,f_u} = \begin{vmatrix} \gamma_{11} & \cdots & \gamma_{1u} \\ \vdots & & \vdots \\ \gamma_{u1} & \cdots & \gamma_{uu} \end{vmatrix}. \tag{63}$$

From here on, a combinatoric approach is used to calculate probabilities that can be compared with experiments. The first example for these is the probability P_m that exactly m electrons are at the target. It can be generated from sums of the inclusive probabilities of equation (62). The final states are from the set of bound target states (cf. section 1.5), $\mathcal{T} = \{\varphi_1, \ldots, \varphi_{K_\mathrm{t}}\}$:

$$P_u^\mathrm{t} = \sum_{\substack{f_1<\cdots<f_u \\ f_j\in\mathcal{T}}} P_{f_1\ldots f_u}. \tag{64}$$

It can be shown that P_m can be expressed in terms of P_u^t [107],

$$P_m = \sum_{u=m}^{N} (-1)^{u-m} \binom{u}{u-m} P_u^\mathrm{t} \tag{65}$$

The probabilities P_m are equivalent to multiple target ionization probabilities P_{q_t} for $q_\mathrm{t} = N_\mathrm{t} - m$.

Probabilities where the final charge states of both centres are considered are found following the same approach. The inclusive probability to find at least u electrons at the target and at least v electrons

at the projectile is defined following the pattern of (64),

$$P''_{uv} = \sum_{\substack{f_1<\cdots<f_u \\ f_j\in\mathcal{T}}} \sum_{\substack{f_{u+1}<\cdots<f_v \\ f_j\in\mathcal{P}}} P_{f_1,\ldots,f_{u+v}}\,, \tag{66}$$

where $\mathcal{P} = \{\varphi_{K_t+1}, \ldots, \varphi_K\}$ is the set of bound projectile states. With the help of P''_{uv} the probabilities P'_{mk} to find exactly m electrons at the target and k electrons at the projectile can be expressed as

$$P'_{mk} = \sum_{u=m}^{N} \sum_{v=k}^{N-u} (-1)^{u-m+v-k} \binom{u}{u-m} \binom{v}{k-v} P''_{uv}\,. \tag{67}$$

Through the sum $N = k + l + m$ these probabilities are directly equivalent to the probabilities

$$P_{kl} = P'_{m=N-k-l,k}\,. \tag{68}$$

While the inclusive-probability method of [75] greatly reduces the combinatoric complexity of the problem, calculating the probabilities P_{kl} is still numerically expensive. In order to calculate them with available computing hardware concessions had to be made to reduce the complexity. Namely, in the present calculations the set of possible final target states has been restricted to the L and M shells. Tests have shown that transitions to the target N shell are negligible and this restriction has no noticeable effect on the results.

3.2 MULTINOMIAL ANALYSIS

In chapter 1 the spin projection of single-electron states was distinguished when establishing the IEM description. However, the time development of single-electron wave functions that differ in spin only is identical due to restricting the scope of the model to atoms and ions that can be described with a single Slater determinant (4)

and approximating the electron-electron interaction with local potentials (cf. p. 17 ff.) What is more relevant to the multinomial analysis is that this applies also to the transition probabilities (27). This tempts one to introduce a change of the nomenclature: Initial conditions $\psi_j(t = t_0)$ are counted with the index j up to the number J of originally occupied spatial orbitals (e.g. $1s$, $2s$,...), each occupied by $n_j = 1, 2$ electrons. For brevity the index j is referred to as initial condition. It is assumed that there is an even number of electrons initially at the target, then each j corresponds to every other i, while $J_\mathrm{t} = N_\mathrm{t}/2$, $J_\mathrm{p} = \lceil N_\mathrm{p}/2 \rceil$, and $J = J_\mathrm{t} + J_\mathrm{p}$.[2]

3.2.1 *Binomial analysis*

In the binomial analysis only electron removal from one collision centre is considered, one does not distinguish between transfer to a bound state of the collision partner or to the continuum. The probability for an electron of the initial condition $j = \lceil i/2 \rceil$ to occupy a bound state of the target atom is p_j^t (27) and the target electron removal probability is $p_j^\mathrm{rt} = 1 - p_j^\mathrm{t}$. Analogously, the projectile electron occupation is p_j^p (27) and removal is $p_j^\mathrm{rp} = 1 - p_j^\mathrm{p}$ for $j = J_\mathrm{t} + 1, \ldots, J$. In the following electron removal from the target is discussed, and the t indices are omitted unless required.

The probability that $q_j = 0, \ldots, n_j$ electrons are removed for an initial condition j is

$$B(j, q_j) = \binom{n_j}{q_j} (1 - p_j)^{q_j} (p_j)^{(N_j - q_j)}. \tag{69}$$

Assuming mutually independent events the product of all $B(j, q_j)$ is

[2] Let $a \in \mathbb{R}$ and $i \in \mathbb{N}$, such that $0 \leq a - i < 1$, then the ceiling is

$$\lceil a \rceil = \begin{cases} a & \text{for } a = i \\ i + 1 & \text{otherwise} \end{cases}$$

the probability for one process leading to the removal of

$$q_\Sigma = \sum_j^{J_\mathrm{t}} q_j \tag{70}$$

electrons, while the sum over all processes is the binomial probability

$$P_q = \sum_{q_1=0}^{n_1} \cdots \sum_{q_{J_\mathrm{t}}=0}^{n_{J_\mathrm{t}}} \left[\delta_{q,q_\Sigma} \prod_j B(j, q_j) \right]. \tag{71}$$

The Kronecker delta ensures that only processes that lead to the removal of the desired number of electrons are summed up, and contribute to the overall probability. Reference [111] shows the same equation in slightly different form, instead of using a delta the sum only includes terms that lead to correct electron removal.

3.2.2 *Trinomial analysis*

In order to consider not only electron removal from the target, but also distinguish ionization and capture by the projectile a trinomial analysis has been introduced in [117]. As a first step a few more single-electron probabilities are defined. The probability for capture, transfer of a target electron to the projectile, is

$$p_j^\mathrm{c} = p_i^\mathrm{p} \quad \text{for } i = 2j-1,\ j = 1, \ldots, J_\mathrm{t}, \tag{72}$$

where p_i^p is the probability to find an electron in a projectile state (27). Likewise, the probability for transfer of a projectile electron to a target state is

$$p_j^\mathrm{c} = p_i^\mathrm{t} \quad \text{for } i = 2j-1,\ j = J_\mathrm{t}+1, \ldots, J. \tag{73}$$

To avoid confusion, in the present work the expression *capture* is used to refer only to the former process, (72). For the same reas-

ons the probability to transfer an electron from the target to the continuum,

$$p_j^{\mathrm{i}} = 1 - p_j^{\mathrm{t}} - p_j^{\mathrm{c}} \quad \text{for } j = 1, \ldots, J_{\mathrm{t}}, \tag{74}$$

is referred to as *ionization* probability. Corresponding to the probabilities for capture p_j^{c}, ionization p_j^{i}, and to remain at the target p_j^{t} are the indices k_j, l_j, and m_j, respectively. As a consequence of (74) they add up to the number of electrons n_j of each initial condition, $n_j = m_j + k_j + l_j$. With trinomial factors, defined as[3]

$$T(j, k_j, l_j) = (k_j, l_j, m_j)! \left(p_j^{\mathrm{c}}\right)^{k_j} \left(p_j^{\mathrm{i}}\right)^{l_j} \left(p_j\right)^{m_j}, \tag{75}$$

the target trinomial probabilty to transfer k electrons to the projectile and l to the continuum is

$$P_{kl}^{\mathrm{t}} = \sum_{k_1=0}^{n_1} \cdots \sum_{k_{J_{\mathrm{t}}}=0}^{n_{J_{\mathrm{t}}}} \sum_{l_1=0}^{n_1} \cdots \sum_{l_{J_{\mathrm{t}}}=0}^{n_{J_{\mathrm{t}}}} \left[\delta_{k,k_\Sigma}\, \delta_{l,l_\Sigma} \prod_j T(j, k_j, l_j) \right], \tag{76}$$

where

$$k_\Sigma = \sum_j k_j, \quad l_\Sigma = \sum_j l_j.$$

As in the case of the binomial probabilities (71) the Kronecker deltas select combinations of indices which contribute to the overall probability P_{kl} that sum up to the specified k and l. The binomial probabilities (71) can be obtained from sums of trinomial probabilities,

$$P_q = \sum_{k=0}^{N_{\mathrm{t}}} \sum_{l=0}^{N_{\mathrm{t}}-k} \delta_{q,k+l} P_{kl}. \tag{77}$$

[3] The first factor in (75) is the trinomial coefficient, following the convention for generalized multinomial coefficients [118]

$$(a_1, a_2, \ldots, a_n)! = \frac{(a_1 + a_2 + \cdots + a_n)!}{a_1!\, a_2! \cdots a_n!}.$$

By the same token a trinomial probability for projectile electrons can be calculated. While this was not used directly for finding the present results, it will be referred to below. Indices are defined mirroring the target case: The number of electrons transferred to the target is k' and to the continuum l'. Then the trinomial probability for a dressed projectile ion has the form of (76) where target quantities are substituted with projectile quantities,

$$P^{\mathrm{p}}_{k'l'} = \sum_{k_{J_\mathrm{t}+1}=0}^{n_{J_\mathrm{t}+1}} \cdots \sum_{k_J=0}^{n_J} \sum_{l_{J_\mathrm{t}+1}=0}^{n_{J_\mathrm{t}+1}} \cdots \sum_{l_J=0}^{n_J} \Big[\delta_{k',k_\Sigma}\, \delta_{l',l_\Sigma} \prod_j T(j,k_j,l_j) \Big]. \quad (78)$$

3.2.3 *Multinomial analysis for active target and projectile electrons*

The previous two sub-sections were concerned with electron transfer from one centre only, focusing on the target. Electrons of the other centre were ignored, except for the aside (78). Changes of the projectile charge state happen due to direct electron removal from the projectile to the continuum as well as transfer processes between target and projectile. Now probabilities for (projectile) charge-state-coincident (target) multiple ionization are to be calculated. In an intermediate step electron loss from the projectile is considered through the elastic probability

$$P^{\mathrm{p}}_0 = \prod_j (p^{\mathrm{p}}_j)^{N_j}, \quad \text{for } j = J_\mathrm{t}+1, \ldots, J, \quad (79)$$

which is the probability that all projectile electrons remain at the projectile. The coincidence with this probability lowers the probability of each process that leads to the transfer of k_j electrons to the projectile and l_j electrons to the continuum

$$\prod_{j=1}^{J_\mathrm{t}} T(j,k_j,l_j) = P^{\mathrm{p}}_0 \prod_{j=1}^{J_\mathrm{t}} T^{\mathrm{t}}(i,k_i,l_i) \quad (80)$$

where T^{t} is the trinomial factor of (75).

Since P_0^{p} does not depend on the index variables in the sums of (76) it can be multiplied with the result of the sum rather than each summand,

$$P_{kl}^{\mathrm{el.p}} = P_0^{\mathrm{p}} P_{k'l}^{\mathrm{t}}\,, \tag{81}$$

where $k = k' + N_{\mathrm{p}}$. The number of projectile electrons N_{p} is considered to ensure a consistent notation with results of the determinantal analysis (cf. section 3.1). Because transfer processes are unlikely for large impact energies equation (81) is a good method to find target ionization probabilities coincident with an unchanged projectile charge state in that energy regime. Other projectile-charge-state-coincident channels cannot be described correctly or not at all.

Equation (81) expresses the assumption that projectile electrons have to remain at the projectile, which is too simplistic when electron transfer is likely to occur. Then it underestimates the probability to find the system in a final configuration where the projectile charge state has not changed much, although, in practice not by a large margin [50]. As an example to illustrate more complex transfer processes that are neglected in (81) consider the following: a configuration where one electron is in the continuum while the projectile charge state remains unchanged can be reached when one electron from the target is captured by the projectile and coincidentally one electron of the projectile is lost to the continuum.

When transfer between collision centres occurs a further step has to be taken and the multinomial model of reference [50] used. It combines trinomial probabilities of both centres (76, 78). The same line of arguments that leads to (80) applies to these more complex cases. However, rather than having only one global probability a trinomial analysis (78) needs to be performed for the projectile electrons. Similar to (80) where the trinomial target factors (75) are lowered by the elastic projectile probability, the trinomial projectile factor has to be

multiplied,

$$M(\boldsymbol{k}', \boldsymbol{k}'') = f'(\boldsymbol{k}')\ f''(\boldsymbol{k}'') = \prod_{j=0}^{J_\mathrm{t}} T^\mathrm{t}(j, k_j, l_j) \prod_{j=J_\mathrm{t}+1}^{J} T^\mathrm{p}(j, k_j, l_j). \quad (82)$$

In order to condense the formulæ the k_j indices are collected in the vectors $\boldsymbol{k}' = (k_1, \ldots, k_{J_\mathrm{t}})$ and $\boldsymbol{k}'' = (k_{J_\mathrm{t}+1}, \ldots, k_J)$. By following the template of (76) by inserting M instead of T and changing the sums accordingly, the probabilities

$$P_{k',l',k'',l''} = \sum_{k_1=0}^{n_1} \ldots \sum_{k_J=0}^{n_J} \sum_{l_1=0}^{n_1} \ldots \sum_{l_J=0}^{n_J} M(\boldsymbol{k}', \boldsymbol{k}'')\ \delta(k', \boldsymbol{k}', k'', \boldsymbol{k}''), \quad (83)$$

are obtained. The probabilities $P_{k',l',k'',l''}$ are an intermediate result – they stand for a specific pattern of electron transfer and ionization, where the primed k and l indices track where electrons are transferred from and to. The function δ is a placeholder for the product of Kronecker deltas, which is not written out here as it will become clear in the next steps. Reordering the sums one obtains

$$P_{k'l',k''l''} = \sum_{j=1}^{J_\mathrm{t}} \sum_{k_j=0}^{n_j} \sum_{l_j=0}^{n_j-k_j} M'(\boldsymbol{k}')\, \delta_{k'k'_\Sigma}\, \delta_{l'l'_\Sigma} \sum_{j=J_\mathrm{t}+1}^{J} \sum_{k_j=0}^{n_j} \sum_{l_j=0}^{n_j-k_j} M''(\boldsymbol{k}'')\, \delta_{k''k''_\Sigma}\, \delta_{l''l''_\Sigma} \quad (84)$$

which is equivalent to the product of the respective trinomial probabilities for both centres (76, 78)

$$P_{k',l',k'',l''} = P^\mathrm{t}_{k'l'} P^\mathrm{p}_{k''l''}. \quad (85)$$

As in (76) and (78) the k indices count the electrons transferred to the other centre and the l indices those transferred to the continuum (all gained a prime each compared to their first occurrence). One can simply add up $l' + l''$ to get the total number of electrons in the continuum. For the number of electrons at the projectile the transfer

processes compensate each other: $k = N_\mathrm{p} + k' - k'' - l''$. To find the multinomial probability P_{kl} the intermediate probabilities $P_{k',l',k'',l''}$ (85) have to be considered for all possible combinations of transfers expressed by its four indices. Two tallies of the k_j and l_j indices are needed to select only index combinations that lead to the sought final k, and l:

$$\kappa = N_\mathrm{p} + k' - k'' - l'', \quad \lambda = l' + l''. \tag{86}$$

Summation over all indices yields the multinomial probabilities for active target and projectile electons

$$P_{kl}^\mathrm{mlt} = \sum_{k'}^{n_\mathrm{t}} \sum_{l'=0}^{n_\mathrm{t}-k'} \sum_{k''=0}^{n_\mathrm{p}} \sum_{l''=0}^{n_\mathrm{p}-k''} P_{k'l'} P_{k''l''} \, \delta_{k\kappa} \, \delta_{l\lambda} \, . \tag{87}$$

Unlike (81) the multinomial probability P_{kl}^mlt includes electron transfers between both centres.

The determinantal analysis (cf. section 3.1) uses the correct statistics for indistinguishable electrons. Since transition probabilities are defined for the many-electron states with the help of inner products of Slater determinants (57), Pauli exclusion is taken into account in (68). This is not the case for the multinomial methods, where transition probabilities are single-electron properties (27). For the present calculations this simplification reduces the numerical cost and thereby computation time by several orders of magnitude. Omission of Pauli exclusion can be a sensible approximation when the number of possible final states are large in comparision to the number of electrons [107]. The influence of Pauli exclusion on the present B^{2+}–Ne collision results will be discussed in 5.1.3.

4 TEST CALCULATIONS

4.1 BASIS SIZE AND CONVERGENCE

The many-electron problem is treated within an IEM (cf. chapter 1). N single-electron equations (25), are solved with a basis expansion method, the TC-BGM, that is described in chapter 2. The BGM-basis $\left\{\chi_\nu^\mu(t) \;\middle|\; \nu = 1,\ldots,K,\ \mu = 0,\ldots,M_\nu\right\}$ is generated with equation (44),

$$\left|\chi_\nu^\mu\right\rangle = \hat{W}(t)\left|\chi_v^{\mu-1}\right\rangle \qquad \text{(44 revisited)}$$

from the generating basis $\left\{\chi_\nu^0 \;\middle|\; \nu = 1,\ldots,K_\mathrm{t}\right\}$. The states $|\chi_\nu^\mu\rangle$ for $\mu > 0$ are in the following called pseudo states. The $|\chi_\nu^0\rangle$ (45) correspond to bound atomic orbitals of the target φ_ν^0, $\nu = 1,\ldots,K_\mathrm{t}$. Basis states $|\chi_\nu^0\rangle$ for $\nu = K_\mathrm{t}+1,\ldots,K$ that correspond to projectile eigenstates are also included in the BGM basis, although no pseudo states are generated from them. The size and structure of the BGM-basis are determined by a set of parameters M_ν, the so called *hierarchy*.

In the present calculations the atomic orbitals φ_ν^0 of the neon target are results of an OPM calculation [73] (cf. section 1.2). This is also the case for the dressed-ion projectiles, B^{2+} and C^{3+}. The φ_ν^0 for bare-ion projectiles are hydrogen-like orbitals. In the present ion–neon collision calculations $K_\mathrm{t} = 29$ neon orbitals from $2s$ to $4f$ formed the generating basis. Furthermore, $K_\mathrm{p} = 30$ projectile eigenstates, $1s$ to $4f$ were included in the basis. For each spatial orbital $2l+1$ states are

included in this count to address the different m quantum numbers.[1]

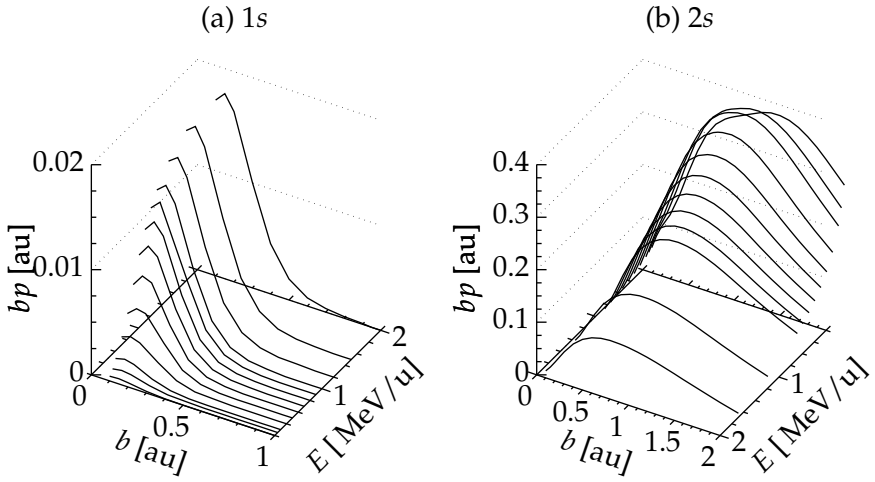

Figure 3: (a) Weighted target electron removal probabilities $bp(b, E)$ of neon 1s electrons in collisions with B^{2+}. (b) weighted ionization probabilities $bp(b, E)$ for a neon 2s electron, shown for reference. Please note that the E-axis in panel (b) is reversed to reduce occlusion.

The neon 1s orbital is not included in the generating basis for the following reasons: (i) For the present collision problems it has only a minor effect on the collision channels of interest. A test calculation has shown that transition probabilities from it are negligibly small except for the highest energies and very small impact parameters (cf. figure 3). Since 1s vacancies are unlikely, transitions to this state can be neglected as well. (ii) The inclusion of the 1s initial condition led to numerical instability. Because of (i) no attempts were un-

[1] The symmetry of the Hamiltonian with respect to the collision plane is used to separate the basis states in two independent subspaces, gerade and ungerade, with the transformation of the spherical harmonics to real functions [107]

$$\left\{Y_{lm}, -l \leq m \leq l\right\} \mapsto \left\{P_l^m \cos\theta \, \sin m\phi, P_l^m \cos\theta \, \cos m\phi, 0 \leq m \leq l\right\},$$

where θ, ϕ are polar and azimuthal angles, and l, m are quantum numbers.

dertaken to remedy these numerical problems, the neon 1s electrons were simply assumed to be passive, i.e. in the dynamics calculation the 1s single-electron state was omitted and the 1s orbital was removed from the zeroth-order of the BGM basis. Still considered were the 1s contributions to the Hartree potential v_{Ha} (8), and the static effective potential v^0_{eff} of the neon atom remained unchanged.

The hierarchy $\{M_\nu\}$ that prescribes the structure of the BGM-basis is chosen following a few rules that rely on experience from previous BGM-calculations with neon targets [103] and calculations using the TC-BGM [74, 106].

The same value for M_ν is chosen for all ν corresponding to orbitals with identical n and l quantum numbers. A monotonous increase of M_ν with ν is preferred, while large steps are to be avoided. However increasing the hierarchy levels M_ν is limited by numerical stability issues. Several examples for such hierarchies are shown in

Table 2: Maximum power M_ν of the potential operator in Eq. (44) for all ν corresponding to target sub-shells 2s to 4f; Each set of M_ν defines the construction of a basis of size N_χ.

M_v for orbitals									
$v=1$	2–4	5	6–8	9–13	14	15–17	18–22	23–29	
2s	2p	3s	3p	3d	4s	4p	4d	4f	N_χ
0	1	2	2	4	5	5	5	5	170
0	1	2	2	4	5	5	5	6	177
0	1	2	3	4	5	5	5	6	180
0	**1**	**2**	**3**	**4**	**5**	**5**	**6**	**6**	**185**
0	1	2	3	4	6	6	6	6	189

table 2. The number of basis states generated for each hierarchy, $N_\chi = \sum_{\nu=1}^{K}(M_\nu + 1)$, is used as an identifier for the bases listed in the table. The hierarchy designated with $N_\chi = 185$, and set in bold, was used to generate the basis for the ion–neon calculations whose results are shown in chapter 5. This hierarchy leads to a basis that

is numerically stable and reasonably well converged, that is, with increasing basis size the results change only little when a few M_ν values of the hierarchy are changed.

Convergence of the basis has been tested with calculations of B^{2+}–Ne collisions over a range of impact energies E and impact parameters b. Figure 4 shows results of these tests. The same hierarchy, $N_\chi = 185$ was used in the present calculations for the other projectile ions (viz. He^{2+}, Li^{3+}, and C^{3+}) in collisions with neon. The observable used for this comparison is the average target electron removal probability, $\bar{p}^{\mathrm{t}}_{\mathrm{rm}}(b) = 1 - P^{\mathrm{t}}_{\mathrm{net}}/N_{\mathrm{t}}$, because it is readily available from the dynamics calculations, and avoids possible influence from the statistical models (cf. section 3). As the differences between the results of the bases of table 2 are too small to be seen at the scale of the plots, the absolute $\bar{p}^{\mathrm{t}}_{\mathrm{rm}}(b)$ values serve as a reference only, while the relative differences of the probabilities for four bases with the $N_\chi = 185$ basis allow for a comparision.

The relative differences of the $N_\chi = 185$ basis with the next larger basis, 189, and immediately smaller basis, 180, remain well under 5%.[2] Increasing the order μ of states generated from neon $4s$ and $4p$ orbitals from $\mu = 5$ to $\mu = 6$, which is the step from $N_\chi = 185$ to $N_\chi = 189$, leads to results that differ little from $N_\chi = 185$. On the other hand, the results from the $N_\chi = 170$ basis differs considerably more from the $N_\chi = 185$ basis for an impact energy of 400 keV/u near $b = 1$ au, the difference occurs close to the maximum of the $p(b)$ curve and therefore has a greater effect on resulting cross sections. The next larger basis, $N_\chi = 177$, does not show such a behaviour, while it differs from $N_\chi = 170$ only by including basis states generated with $\mu = 6$ from neon $4f$ orbitals. At large impact parameters b the relative difference plots tend to exagerate small absolute differences between the calculations as the probabilities $p(b)$ become

[2] There is an artifact, for $N_\chi = 180$ at 1 MeV/u, division by small probabilities at small impact parameters exaggerates the relative differences.

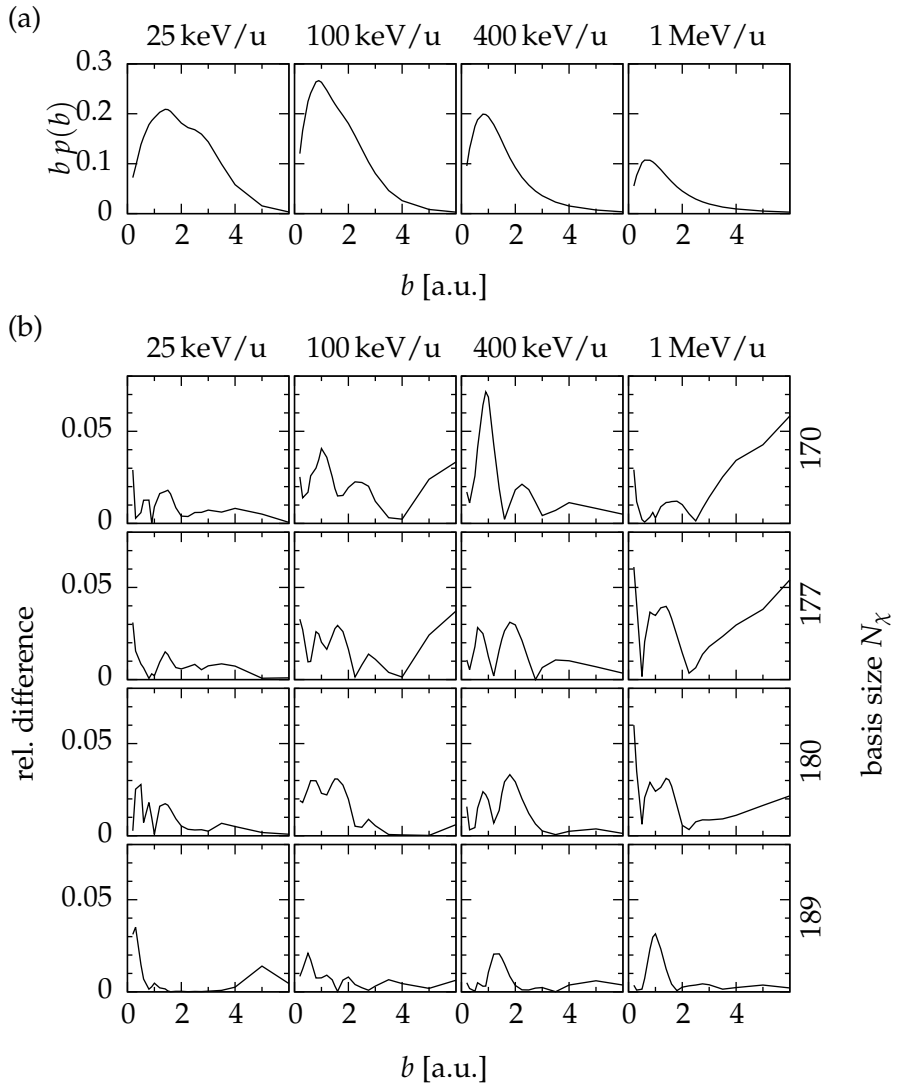

Figure 4: Basis convergence for bases generated with the hierarchies of table 2 in calculations for the B^{2+}–Ne collision system. (a) Average target electron removal probabilities $\bar{p}^{\mathrm{t}}_{\mathrm{rm}}(b) = 1 - P^{\mathrm{t}}_{\mathrm{net}}/N_{\mathrm{t}}$ weighted with the impact parameter b, and as a function of b obtained from $N_\chi = 185$. Plots for four impact energies E are shown side-by-side. (b) Relative differences $\left|p_{N_\chi}/p_{185} - 1\right|$ of the average removal probabilities $\bar{p}^{\mathrm{t}}_{\mathrm{rm}}(b)$ of (a), comparing the basis for $N_\chi = 185$ with bases N_χ, denoted on the right-hand-side of the array.

quite small. The fact that the results do not change very much with changes of the basis size, and that the differences tend to get smaller with increasing basis size (compare $N_\chi = 180$ and $N_\chi = 189$ in figure 4) shows the basis is well converged at $N_\chi = 185$.

4.2 RESPONSE

In section 1.5 it has been mentioned that the extraction of transition amplitudes c_i^ν (26) poses a problem when response is considered in the target Hamiltonian (23) through the screening factor a (22). Transition amplitudes can be extracted by projecting on undisturbed initial eigenstates $|\varphi_\nu^0\rangle$ (29) or on instantaneous eigenstates $|\varphi_\nu(t)\rangle$ (31) of the target Hamiltonian (23). In order to avoid confusion of the similar sounding names in the following the former, φ_ν^0, are referred to as atomic orbitals. The effect of the choice of eigenstates on final results is investigated in this section with the help of test calculations. For these tests an earlier implementation of the BGM, OC-BGM [47–51, 103, 110, 111], was used. Only states centred at the target are included in the zeroth-order subspace of this method. The test collision system consists of the bare-ion He^{2+} projectile and a neon target. The $N_\chi = 185$ hierarchy that is used for the ion–neon TC-BGM calculations and described in section 4.1 was used as well for the test calculations.

The choice of eigenstates to project on influences transition amplitudes that are extracted for two distinct purposes:

(i) *Final-state analysis*: Transition amplitudes are extracted at t_f in order to generate final results, for example, the target net occupation $P_\mathrm{net}^\mathrm{t}$ (28). Since it is an observable that can be calculated directly it is a convenient example for this discussion – that is, the statistical final-state analysis is of no concern. By substituting the transition amplitudes with (26) the dependence on the

bound target states becomes explicit:

$$P_{\text{net}}^{\text{t}} = \sum_{i=1}^{N} \sum_{\nu=1}^{K_{\text{t}}} \left| \langle \varphi_\nu | \psi_i(t_{\text{f}}) \rangle \right|^2. \tag{88}$$

Namely, the bound states are either $|\varphi_\nu\rangle \equiv |\varphi_\nu^0\rangle$ or $|\varphi_\nu\rangle \equiv |\varphi_\nu(t_{\text{f}})\rangle$ for all $\nu = 1, \ldots, K_{\text{t}}$.

(ii) *Response model*: Transition probabilities are extracted at every time step to determine the target occupation as input for the target screening model. That is, the screening factor a (22) in the Hamiltonian (23) also depends on the choice of bound target states. Written out explicitly, by inserting (88) into (22), it is:

$$a(t) = \frac{\sum\limits_{i=1}^{N} \sum\limits_{\nu=1}^{K_{\text{t}}} \left| \langle \varphi_\nu | \psi_i(t) \rangle \right|^2 - \left(N_{\text{t}}^{-1} \sum\limits_{i=1}^{N} \sum\limits_{\nu=1}^{K_{\text{t}}} \left| \langle \varphi_\nu | \psi_i(t) \rangle \right|^2 \right)^{N_{\text{t}}}}{N_{\text{t}} - 1}. \tag{89}$$

For the final-state analysis we suppose that the projectile is far from the target and enough time has passed for the collision system to approach its state at $t \to \infty$. Since the ionization probabilities can be significant for the collisions of interest it is more plausible to project on states that reflect the ionic nature of the target after the collision [107]. Accordingly, in case (i) the more convincing approach is projecting on instantaneous eigenstates, $|\varphi_\nu\rangle \equiv |\varphi_\nu(t)\rangle$. For case (ii) the argument in favour of using instantaneous eigenstates is not as compelling: The screening factor a has to be determined at all times during the collision, including times when both collision centres are at close proximity. Moreover, the change of screening due to response is typically the greatest at exactly these times: shortly before and after the closest approach. Previous calculations have shown that the target occupation sharply reduced immediately after the closest approach, followed by a longer interval where the target occupation

recovered again [48]. For such small internuclear distances neither of the stationary Schrödinger equations (29, 31) is adequate to the situation, as these equations correspond to ideal initial conditions for which the potential of the respective other centre is assumed to have vanished.

Table 3: Quick reference chart for the options A to D, explained in the text.

(88) \ (89)	$\varphi_\nu^0 \mapsto a$	$\varphi_\nu(t) \mapsto a$
$\varphi_\nu^0 \mapsto P_{\text{net}}^{\text{t}}$	A	B
$\varphi_\nu(t) \mapsto P_{\text{net}}^{\text{t}}$	C	D

The choice of atomic orbitals or instantaneous eigenfunctions can be taken independently for both cases, (i) and (ii). Because of the considerable differences between (i) and (ii) all four combinations for the two choices were tested; designated A to D, they are:

A Atomic orbitals φ_ν^0 are used for both cases, i.e. in (88) and (89).

B Instantaneous eigenfunctions $\varphi_\nu(t)$ are used in the response model (89), while atomic orbitals φ_ν^0 are used for the final-state analysis, e.g. in (88).

C Atomic orbitals φ_ν^0 are used in the response model (89), while instantaneous eigenfunctions $\varphi_\nu(t)$ are used for the final-state analysis, e.g. in (88).

D Instantaneous eigenfunctions $\varphi_\nu(t)$ are used for both cases, i.e. in (88) and (89).

As a quick reference the above combinations are listed in table 3.

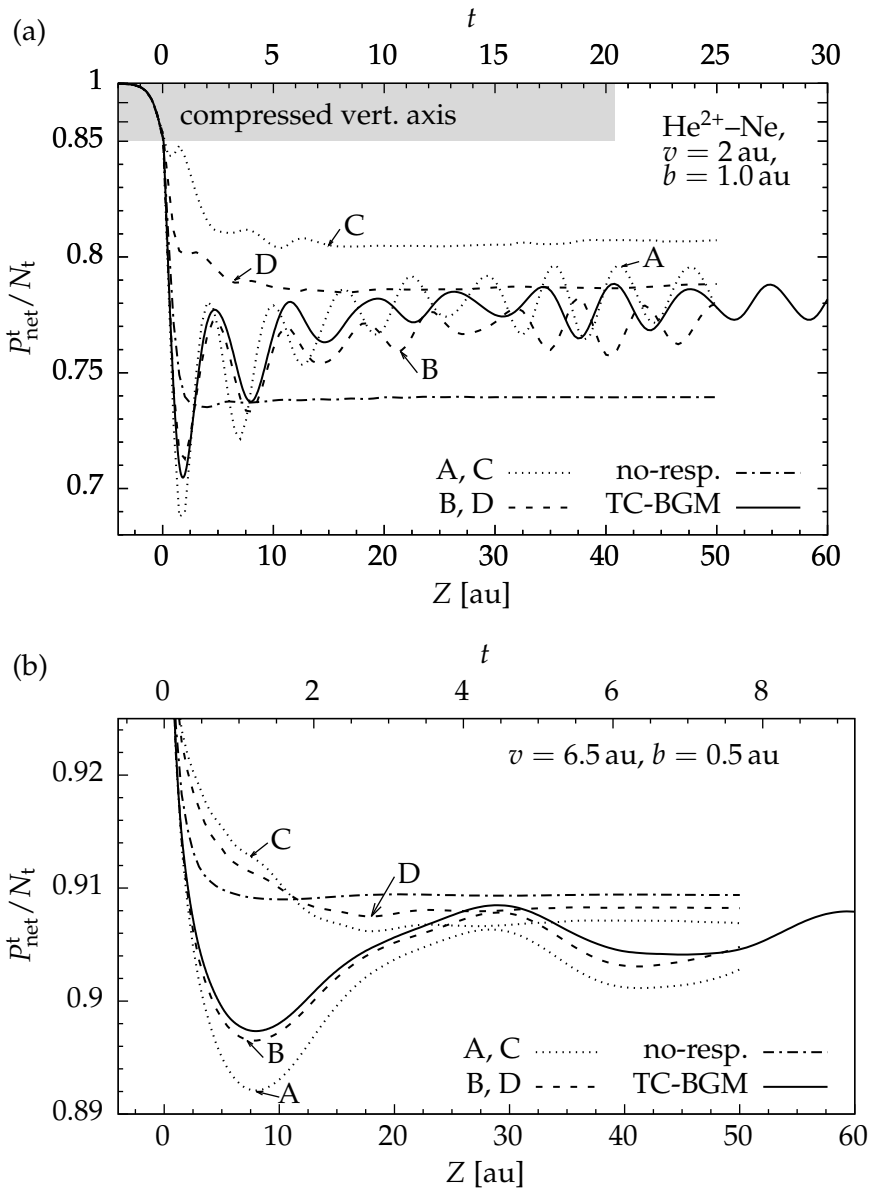

Figure 5: Time development of the average target occupation $P^{\mathrm{t}}_{\mathrm{net}}/N_{\mathrm{t}}$ in He^{2+}–Ne collisions: (a) $v = 2\,\mathrm{au}$ (100 keV/u), $b = 1\,\mathrm{au}$; (b) $v = 6.5\,\mathrm{au}$ (1 MeV/u), $b = 0.5\,\mathrm{au}$. Results of an OC-BGM calculation where no states at the projectile were considered. Curves A, C (dotted lines) and B, D (dashed lines) are explained in the text. Results of a no-response OC-BGM calculation (dash-dotted) and of a target-response TC-BGM calculation (solid line) are shown for comparison. Please note that the vertical axis of (a) is compressed for $P^{\mathrm{t}}_{\mathrm{net}}/N_{\mathrm{t}} > 0.85$.

In figure 5 (a) the average target occupation $P^{\mathrm{t}}_{\mathrm{net}}/N_{\mathrm{t}}$ is shown as a function of the projectile position Z in a 100 keV/u He^{2+}–Ne collision with an impact parameter of $b = 1$ au. The following frame is assumed: the target is at rest; $Z = 0$ and $t = 0$ at the closest approach. Because of the straight-line–trajectory approximation Z in this frame is proportional to time, $Z = vt$.

In the plot, all four curves, corresponding to A - D, show the same behaviour before the closest approach ($Z = 0$). At $Z = -5$ au the probabilty begins to drop from unity to about 0.85. From this point on the curves begin to diverge, and two groups of two curves each can be distinguished: The calculations where atomic orbitals were used in the final-state analysis, A and B, continue to fall sharply and oscillate very noticeably until the calculation ends. Despite the different choice of eigenstates in (89) for A and B, there is no tangible or relevant difference between both curves. In contrast, both calculations where instantaneous eigenstates were used in the final-state analysis, C and D, show hardly any oscillations. The trough immediately after the closest approach is also less pronounced, in particular for curve C. The choice of eigenstates in the target response model leads in the end to a difference between the C and D results.

In comparison to all response calculations the no-response calculation results in noticeably reduced net occupation and shows no oscillations. The results of a TC-BGM calculation – the present target-response results in chapter 5 were calculated in the same way – is also included in figure 5 (a). The different treatment of capture and a different choice of basis parameters somewhat restricts a direct comparison of the OC-BGM and TC-BGM results. Nonetheless, the target-response model in the TC-BGM calculation corresponds to the approach of the A-curve, and shows similar oscillations of $P^{\mathrm{t}}_{\mathrm{net}}/N_{\mathrm{t}}$.[3]

[3] In order to compensate these oscillations the results in chapter 5 are averages of a number of probabilities calculated from $z > 40$ au, in 5 au steps, up to the maximum internuclear distance $R_{\mathrm{in}} = 60$ au.

Figure 5 (b) shows for a collision that is much closer, $b = 0.5\,\text{au}$, and faster, $v = 6.5\,\text{au}$ ($E = 1\,\text{MeV/u}$), a comparison that follows the pattern of the previous figure. The overall behaviour of curves A to D is very similar to that at $v = 2\,\text{au}$, albeit, in a much shorter timeframe. In other words, A and B show noticeable oscillations, while C and D smoothly approach their final values. For such fast collisions, where electron removal probabilities are small, the effect of response is expected to be small, with increasing impact energy the results of response and no-response calculations ought to converge. As seen in comparison with the no-response calculation, and the fine scale of the plot's vertical axis this is nearly the case. Calculation D is indeed very close to the no-response curve, but calculations A and B lead both to increased target electron removal.

The increased ionization in response models A and B appears similar to the effect of shake-off. Shake-off is a process where after sudden electron removal secondary electrons are also lost [119, 120]. This process is typically observed in much faster collisions, for example, in collisions of lowly charged ions with helium where it dominates for impact energies in excess of 10 MeV/u [121]. When the direct ionization happens fast enough other electrons are in a state that is not an eigenstate of the ion, which leads to a transition probability that is found by the overlap of the atomic orbitals with the continuum of the ion [122].

At 1 MeV/u impact energy the no-response OC-BGM and TC-BGM calculations results are almost identical (were the latter shown in figure 5 (b) both curves would be separated by a line's-width only). The no-response curve that is shown in the figure can be used as a reference for OC-BGM as well as for TC-BGM response curves. Like the OC-BGM calculations A and B target electron removal is increased for the response TC-BGM calculation. Since this effect cannot be compensated by averaging it shows up in the present results that will be discussed in the following chapter.

In conclusion, noticeable oscillations occur in response calculations when observables are extracted by projecting on atomic orbitals φ_ν^0. The oscillations can be avoided by using instantaneous eigenstates for the final-state analysis.

Using instantaneous eigenfunctions in the global target-response model leads to reduced electron removal, however, the oscillation issue persists. Since there is no compelling reason to choose one approach over the other when it comes to input for the response model, the difference of the results is inconclusive.

The small scale of the oscillations and differences between the different approaches with regard to the extraction of observables is not relevant to net probabilities and net cross sections. However, based only on net probabilities a prediction for more specific collision channels (e.g. P_{kl} of chapter 3) cannot be made. In the case of often complex transfer-ionization processes small changes of single-electron amplitudes might have considerable effects. The difference between the TC-BGM response curves and the no-response curve at high impact energies shown here can indeed be seen in the present results, where it is amplified in processes in which a large number of electrons are involved. This will be discussed in section 5.2.

Model A has been used in the present TC-BGM target-response calculations. Based on the test calculations and in comparison with previous response calculations the errors due to response model A were considered to be too small to require immediate correction – in particular in the light of the fundamental shortcommings the IEM has when dealing with processes that involve the transfer of a large number of electrons. Nonetheless, it would be sensible to implement model C for future TC-BGM calculations.

5 BARE AND DRESSED ION IMPACT ON NEON

In this chapter the results of TC-BGM calculations for ion–neon collisions are discussed. The focus is at first on B^{2+}–Ne collisions and on multiple target ionization coincident with an unchanged projectile charge state, $Ne + B^{2+} \rightarrow Ne^{q_t+} + B^{2+}$. These collision channels are called *pure ionization* by Wolff et al [35].

The role of active projectile electrons in pure ionization is investigated by comparing the results of two final-state analyses: In one case active target and projectile electrons are considered, while in the other case only target electrons are active. Both analyses use the determinantal method and results of the same TC-BGM dynamics calculation. The multinomial method is used for an analysis of complex transfer ionization processes that involve capture by and loss from the projectile but still lead to the same projectile charge state, $q_p^f = 2$. Subsequently, the role of Pauli exclusion is discussed for this collision system. The overall results of section 5.1 were found in preparation of [123] and published in large parts therein.

A comparison of no-response and target-response results for the He^{2+}–Ne and B^{2+}–Ne collision systems follows in section 5.2. Based on these results the target-response model was used for all following calculations of ion impact on neon, viz. the remaining four sections of chapter 5. The gist of these results was published in [124, 125], however, in the present work more detail is given.

Present target electron capture and projectile electron loss results

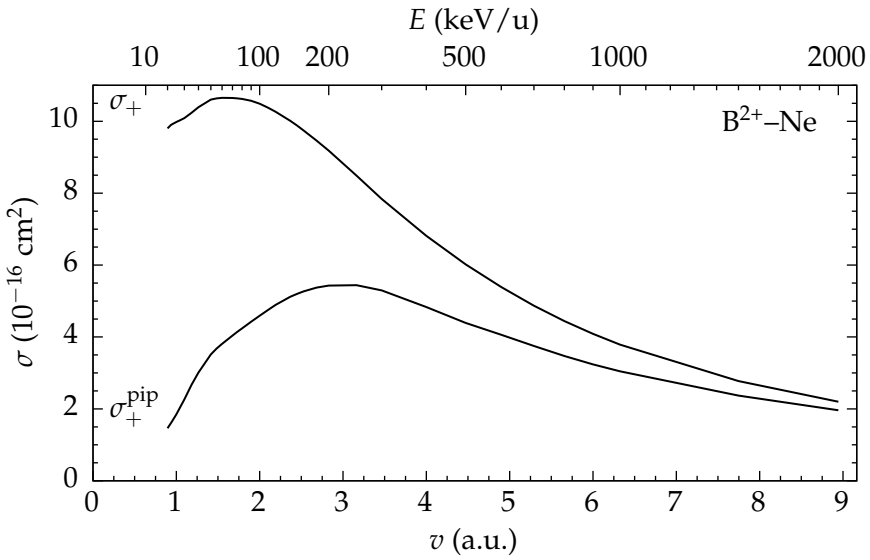

Figure 6: Net recoil ion production σ_+ (56) and positive ion production σ_+^{pip} (90) of [123] as a function of relative velocity v for collisions of $B^{2+}$with Ne atoms.

are compared with experimental data in section 5.3. Building upon this comparison is an investigation of the contributions of different projectile-charge-state-coincident collision channels to the net ionization of neon by B^{2+} impact (section 5.4). In section 5.5 ionization and capture results for C^{3+} and Li^{3+} impact on neon are compared with experimental data. Other than the more detailed analysis for B^{2+}–Ne in previous sections this comparison is brief and mostly serves as preparation of the following section 5.6, where the differences between dressed-ion and bare-ion impact are discussed.

5.1 ACTIVE TARGET AND PROJECTILE ELECTRONS

5.1.1 *Pure target ionization*

In a recent article Wolff et al [35] reported total cross sections for pure target ionization in B^{2+}-Ne collisions resulting from experiments and

theoretical CDW-EIS calculations. Since response was not considered in these calculations the no-response approximation was used in the present TC-BGM calculations discussed in this section. The numbers of electrons found after the collision at the projectile and in the continuum are for pure ionization $k = N_\mathrm{p}$ and $l = q_\mathrm{t}^\mathrm{f}$, respectively. Total cross sections for pure ionization by B^{2+} impact are thus denoted σ_{31} to σ_{35}. Ionization to higher charge states is insignificant, and such data were not provided in reference [35].

Similar to the net recoil ion production σ_+ (56) – which is an inclusive quantity that allows an overview of target ionization in a collision – the positive ion production is defined as

$$\sigma_+^\mathrm{pip} = \sum_l l\sigma_{3l}. \tag{90}$$

To give a scale comparison the positive ion production σ_+^pip is shown together with σ_+ in figure 6. The σ_+ is considerably larger at low impact energies, as capture processes that are dominant in this regime are very likely to change the projectile charge state. The curves approach each other at high impact energies, where capture is insignificant. The remaining difference is due to the loss of projectile electrons to the continuum which is included in σ_+. Target ionization processes that are coincident with different projectile charge states and which make up the increase of the σ_+ over the σ_+^pip curve are discussed in more detail in section 5.4.

For the present results active target electrons and active projectile electrons were considered both in the TC-BGM dynamics calculation and in the statistical final states analysis using the determinantal method (see chapter 2 and section 3.1 respectively). For the rest of this section these results are labelled BGM-T+P. Based on the same TC-BGM dynamics results a modified statistical analysis has been carried out where projectile electrons were considered passive in the de-

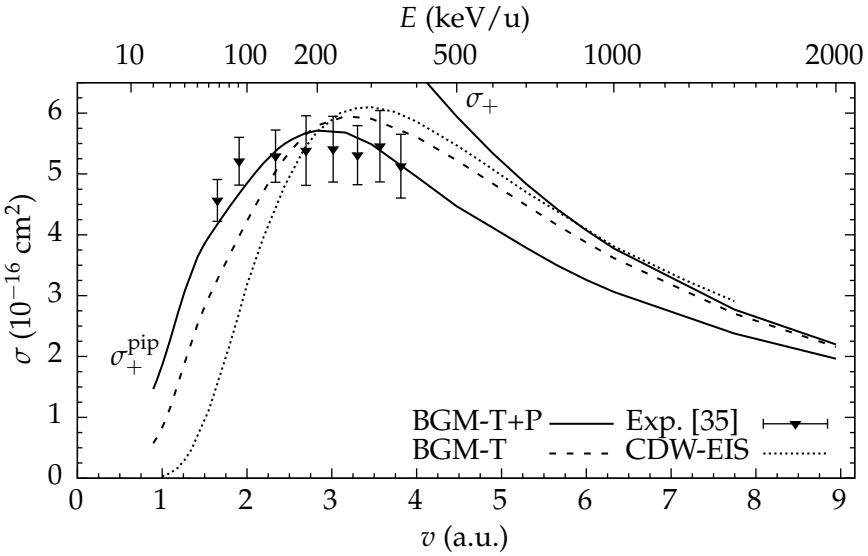

Figure 7: Comparision of positive ion production σ_+^{pip} (90) for $l = 1, \ldots, 5$, for the B^{2+}–Ne collision system using BGM-T+P (solid line) and BGM-T (dashed line) final-state analyses, and of CDW-EIS (dotted line) calculation [35]. For reference, the BGM-T+P net recoil ion production σ_+ curve is partially shown. Experimental data points [35].

terminant method. This means that, propagated projectile states $|\psi_i\rangle$ for $i > N_t$ were not included in the density matrix (63). Yet, the set of final states still includes projectile orbitals, that is, target electron capture is still taken into account. This final-state analysis is henceforth called *target-only* and labelled BGM-T. With regard to projectile electron removal the BGM-T is alike to the CDW-EIS calculation of reference [35] – both do not consider such processes.

Theoretical results are compared with experimental data of [35] for the positive ion production σ_+^{pip} in figure 7. The maximum of the BGM-T+P σ_+^{pip} curve is at 200 keV/u. It falls off rapidly for lower impact energies while it decays slowly towards higher energies. The position of the peak coincides with the middle of the set of experimental data points [35] whose structure resembles a plateau that drops off for the first and last point. Overall, the results of the BGM-T+P calculation are in good agreement with the experiment and lie well within the range of the experimental uncertainty. However, when following the curve from the peak towards lower energies the BGM-T+P curve falls off earlier than the experimental data, the data point at 90 keV/u is noticeably underestimated, the error-bars of the data point at 68 keV/u barely missed.

When comparing BGM-T+P and BGM-T σ_+^{pip} results it is remarkable that BGM-T+P cross sections are higher than those of the BGM-T analysis for slow collisions ($v < 2.5$). After all, BGM-T+P allows electrons to be captured by the projectile, which is indeed very likely to happen in such slow collisions. One might expect that probability would be shifted from pure ioniztion P_{3l} collision channels to other projectile-charge-state-coincident channels, in turn, lowering the cross section for the former. However, these capture processes are compensated by transfer ionization processes, where capture into the projectile is coincident with removal of electrons from it (e.g. capture of one electron from the target and coincident loss of an electron to the continuum). In section 5.1.2 such processes are analysed and

discussed in detail. For faster colllisions, from $v \approx 3$ on, BGM-T results exceed the BGM-T+P results. Overall, the BGM-T+P results are in better agreement with the experimental data than the BGM-T reults.

The results of the CDW-EIS calculation [35] differ noticeably for the positive ion production channel σ_+^{pip}. The maximum of the CDW-EIS σ_+^{pip} curve is at a slightly higher impact energy, at about 300 keV/u, exceeding at this point both the maxima of the BGM-T+P curve and the experimental data. Left of the peak the CDW-EIS curve also falls off more rapidly than the BGM-T+P and BGM-T curves. It underestimates the first three experimental data points at low impact energies. Right of the maximum the CDW-EIS is very similar to the BGM-T curve, both in shape as in absolute values, and thus exceeds the BGM-T+P σ_+^{pip} results. In this energy regime the BGM-T+P probabilities for pure target ionization, that determine the σ_+^{pip}, are lowered because of projectile electron loss, shifting probability to collision channels coincident with higher boron-ion charge states.

Both, the CDW-EIS and the BGM-T calculation do not consider projectile electron loss, which is the only relevant process changing the charge state of the B^{2+}-ions in fast collisions ($E > 1\,\mathrm{MeV/u}$). This makes these σ_+ results comparable to the net recoil ion production σ_+ which is inclusive of all projectile charge states, as can be observed in figure 7: For such fast collisions the CDW-EIS and BGM-T results approach the σ_+ results of the BGM-T+P calculation indeed. (In order to correspond to the results of [35] the sum in (56) has been truncated at five-fold ionization for the σ_+ results shown in figure 7.)

For impact energies where ionization directly to the continuum is insignificant (in comparison to processes involving transfer) the difference between the BGM-T and the CDW-EIS calculations can be explained with transfer ionization processes, which were not modelled in the CDW-EIS calculation. Furthermore, there are differences on a more fundamental level. Below 100 keV/u CDW-EIS is as a perturbative method not expected to be valid [53].

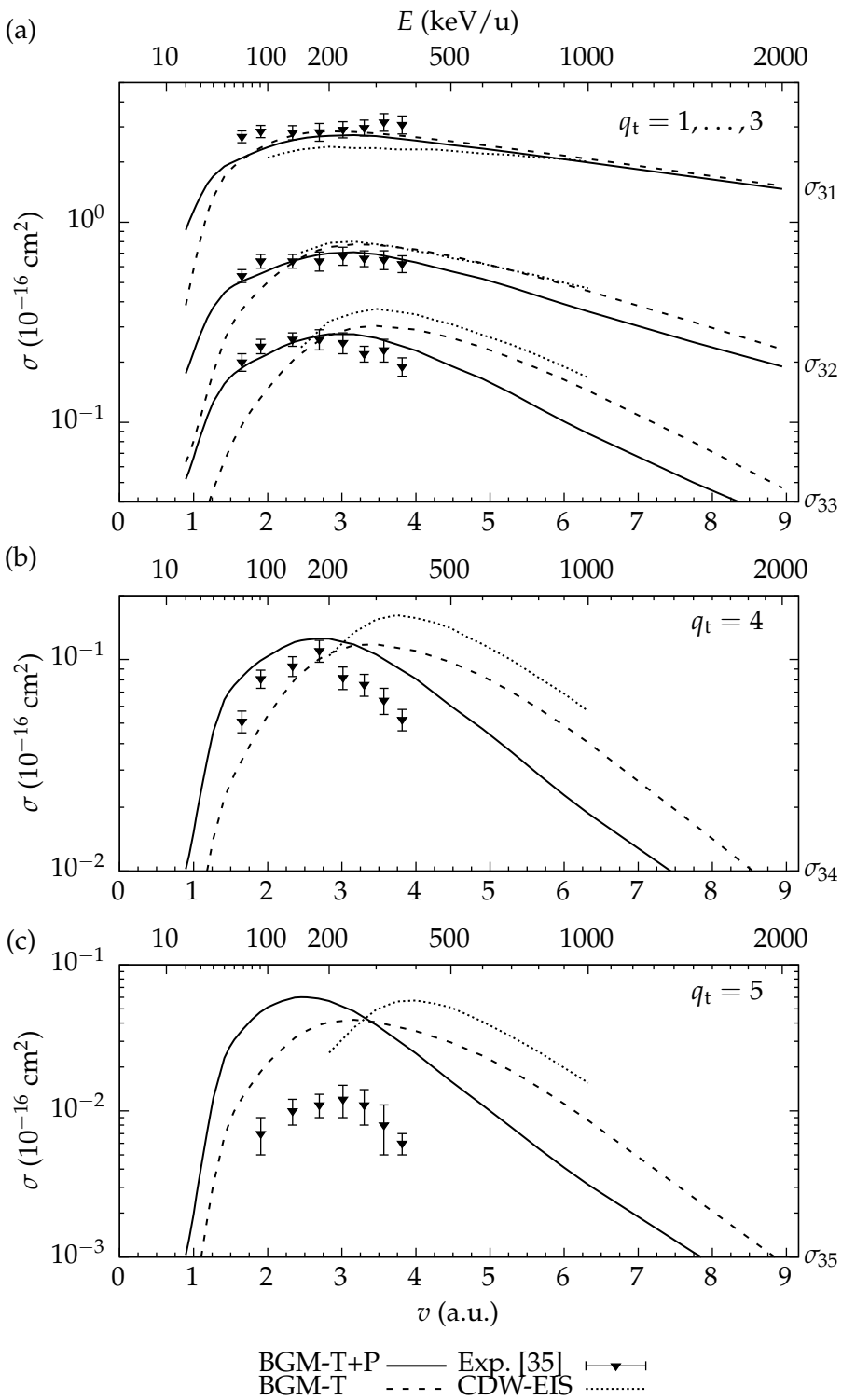

Figure 8: Pure q_t-fold ionization for B^{2+}–Ne collisions; results of no-response BGM-T+P (solid line) and BGM-T (dashed line) calculations, CDW-EIS (dotted line) [35], and experimental data [35] for (a) single, double, and triple pure ionization; (b) four-fold pure ionization; (c) five-fold ionization.

Figure 8 shows pure multiple target ionization cross sections, where $l = 1, \ldots, 5$ electrons are found in the continuum at t_f, while the projectile charge state is unchanged, thus $k = 3$. The q_t weighted sum of these cross sections σ_{3l} is the positive ion production σ_+^{pip} (90). The BGM-T+P curves are in fair agreement with the experimental data for σ_{31}, and in good agreement for σ_{32} and σ_{33}, all three collision channels are shown in panel (a) of figure 8. However, the experimental data points at the lowest impact energies are underestimated for single ionization σ_{31}. The BGM-T+P double and triple ionization curves follow the apparent shape of the experimental data much more closely. In [123] we speculated that response effects would be responsible for underestimating single ionization in slow collisions. However, response calculations carried out in [124] found no indication for this (see also section 5.2 on target response).

The BGM-T+P calculation overestimates the experimental results for pure four-fold ionization σ_{34} while it reproduces the velocity dependence of the experimental data shown in figure 8 (b). The experimental data are overestimated to a much greater extent for pure five-fold ionization σ_{35}, in figure 8 (c). Based on experience from previous IEM calculations – e.g. [50] ($He^{2+}-Ne$), [103] ($C^{4+}-Ne$), [49] ($He^{2+}-Ar$), and [126] ($p-H_2O$) – one can expect multiple ionization to be overestimated when the final charge state of the target q_t^f exceeds the initial charge state of the projectile q_p^i by more than one, $q_t^f > q_p^i + 1$. This is also the case for the present results: the calculation agrees well with the experiment only up to $q_t^f = 3$, that is, triple neon ionization by B^{2+}-impact.

The present BGM-T calculation and the CDW-EIS calculation of [35] converge with increasing projectile energy for pure single and double target ionization, σ_{31} and σ_{32}. For higher final target charge states q_t^f the CDW-EIS curve exceeds the BGM-T curve more and more. This difference at high impact energies is small in comparison to the difference of the BGM-T+P and BGM-T results. For slower collsions the

differences between BGM-T and CDW-EIS are more nuanced than the more inclusive σ_+^{pip} shows. The CDW-EIS curve for single ionization is slightly below the BGM-T curve and has the same shape. For double ionization both curves are nearly identical. Yet, the differences of the CDW-EIS to the BGM-T results are considerable when more target electrons are ionized.

These observations are consistent with the findings from the discussion of figure 7. The results of passive and active projectile electron methods differ in fast collisions mostly because of projectile electron loss. In slower collisions the greatest difference is between the BGM methods and the CDW-EIS, due to the latter's limitations in describing single-electron dynamics in a two-centre situation with the possiblity of electron transfer [124].

5.1.2 *Transfer ionization, multinomial analysis*

Indications of transfer ionization processes were found in section 5.1.1 by comparing BGM-T+P and BGM-T pure ionization results. With the help of the determinant method used in the statistical final-state analysis for both BGM-T+P and BGM-T it is not possible to distinguish such different processes. This is not a limitation of the determinant method, it is rather a fundamental property of the statistics for indistinguishable particles. The determinantal method provides exclusive transfer probabilities, the squared modulus of the inner product of the propagated many-electron wave function (57) with final-state configurations. The present determinant method uses the inclusive probability ansatz [75] which yields the probability to find the system in any configuration that fits given criteria, in this case, a collision channel where k, l electrons are at the projectile and in the continuum, respectively. In order to differentiate different processes that lead to the same k, l a multinomial model can be used (cf. section 3.2). Unlike the determinantal method in the multinomial method anti-

symmetry of electrons is neglected. While one has to be careful with such a picture it can be a good approximation for the present collision problems when focusing on electrons initially at the target. The number of possible states electrons can transfer to is large in comparison to the number of electrons transferred. This makes it less likely that transfer processes that would be blocked by Pauli exclusion contribute to the results of the statistical model. The assumption that the multinomial method is indeed a good approximation for the present problems will be tested in section 5.1.3 where the influence of Pauli exclusion on the present results will be investigated.

With the help of the multinomial method the single-ionization channels can be broken up into contributions from the specific ionization and transfer ionization processes, namely, that lead to $k = 3$, $l = 1$ and $k = 3$, $l = 2$, for pure single and double ionization, respectively.

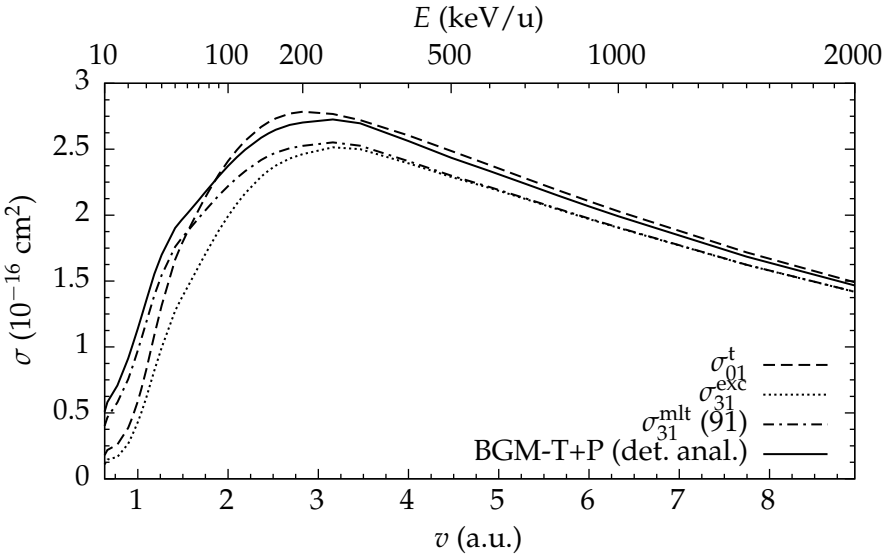

Figure 9: Single target ionization coincident with unchanged projectile charge state ($k = 3$, $l = 1$) cross sections for B^{2+}–Ne collisions; calculated with a multinomial analysis considering active target and projectile electrons $\sigma_{31}^{\mathrm{mlt}}$ (91) (chain line); trinomial single target-only ionization σ_{01}^{t} (dashed line); exclusive single target ionization $\sigma_{31}^{\mathrm{exc}}$ (dotted line); and BGM-T+P determinantal analysis (solid line). See the text for an explanation of the statistical methods used to calculate each cross section.

Figure 9 shows transfer ionization processes contributing to pure single target ionization σ_{31} calculated with the multinomial analysis. The BGM-T+P σ_{31} curve of figure 8 (a), that was calculated with the determinant method, serves as a reference to the multinomial results.

Starting point for this discussion is the σ_{01}^{t} curve, which is the result of a trinomial analysis that considers only active target electrons. It corresponds to transfer of zero electrons to the projectile and one electron to the continuum, and is calculated with equation (76) (cf. section 3.2.2). Since it is indifferent to the projectile charge state the trinomial σ_{01}^{t} curve is nearly identical to the BGM-T curve of figure 8 (a) (not included in figure 9). It is interesting to see the effect of including active projectile electrons, while avoiding more complex

processes where electrons of both centres are transferred. This can be done by taking the elastic probability P_0^{p} (79) for projectile electrons to remain at their centre into account. The modified trinomial probability is $P_{kl}^{\mathrm{el.p}}$ (81). The corresponding cross section for single target ionization is denoted by $\sigma_{31}^{\mathrm{exc}}$. Since $P_0^{\mathrm{p}} \leq 1$ it is not surprising that the $\sigma_{31}^{\mathrm{exc}}$ curve is the lowest in figure 9.

However, exclusive ionization of one target electron is not the only process that leads to a final configuration with one electron in the continuum and three at the boron ion (cf. section 3.2.3). The other processes contributing to this channel can be found by using equation (87), which gives

$$P_{31}^{\mathrm{mlt}} = \underbrace{P_{01}^{\mathrm{t}} P_{00}^{\mathrm{p}}}_{a} + \underbrace{P_{10}^{\mathrm{t}} P_{01}^{\mathrm{p}}}_{b} + \underbrace{P_{11}^{\mathrm{t}} P_{10}^{\mathrm{p}}}_{c} + \underbrace{P_{20}^{\mathrm{t}} P_{11}^{\mathrm{p}} + P_{21}^{\mathrm{t}} P_{20}^{\mathrm{p}} + P_{30}^{\mathrm{t}} P_{21}^{\mathrm{p}} + P_{31}^{\mathrm{t}} P_{30}^{\mathrm{p}}}_{\text{rest}} . \tag{91}$$

$P_{k'l'}^{\mathrm{t}}$ and $P_{k''l''}^{\mathrm{p}}$ are trinomial probabilities (76, 78) that consider only active electrons of target and projectile, respectively.[1] The terms in equation (91) are denoted as follows:

a is identical to the exclusive single-ionization probability P_{31}^{exc}.

b is a transfer ionization process where one electron is transferred

[1] The three electrons at the boron ion offer only a very limited number of combinations, using (78) the trinomial probabilities for projectile ionization and transfer are:

$$\begin{aligned}
P_{01}^{\mathrm{p}} &= 2p_{1s}^{\mathrm{i}} p_{1s} p_{2s} + (p_{1s})^2 p_{2s}^{\mathrm{i}} \\
P_{10}^{\mathrm{p}} &= 2p_{1s}^{\mathrm{c}} p_{1s} p_{2s} + (p_{1s})^2 p_{2s}^{\mathrm{c}} \\
P_{11}^{\mathrm{p}} &= 2p_{1s}^{\mathrm{c}} p_{1s}^{\mathrm{i}} p_{2s} + 2p_{1s}^{\mathrm{c}} p_{2s}^{\mathrm{i}} p_{1s} + 2p_{1s}^{\mathrm{i}} p_{2s}^{\mathrm{c}} p_{1s} \\
P_{20}^{\mathrm{p}} &= (p_{1s}^{\mathrm{c}})^2 p_{2s} + 2p_{1s}^{\mathrm{c}} p_{2s}^{\mathrm{c}} p_{1s} \\
P_{21}^{\mathrm{p}} &= (p_{1s}^{\mathrm{c}})^2 p_{2s}^{\mathrm{i}} + 2p_{1s}^{\mathrm{c}} p_{1s}^{\mathrm{i}} p_{2s}^{\mathrm{c}} \\
P_{30}^{\mathrm{p}} &= (p_{1s}^{\mathrm{c}})^2 p_{2s}^{\mathrm{c}}
\end{aligned} \tag{92}$$

The notation of the projectile single-electron probabilities follows that of section 3.2, the $^{\mathrm{p}}$ labels have been omitted: occupation p_j, transfer to the continuum p_j^{i}, transfer to a target state p_j^{c}.

from the target to the projectile coincident with the transfer of one electron from the projectile to the continuum.

c is a transfer ionization process where one target electron is transferred to the projectile and one to the continuum coincident with the transfer of one electron from the projectile to the target.

rest collects the remaining processes which involve the transfer of several electrons; they contribute very little to the multinomial probability P_{31}^{mlt}.

Since additional terms (*b*, *c*, 'rest') are added to the exclusive single-ionization probability P_{31}^{exc}, the corresponding total cross section $\sigma_{31}^{\mathrm{mlt}}$ is always above the $\sigma_{31}^{\mathrm{exc}}$ curve in figure 9.

For very slow collisions ($v < 1.5$) the $\sigma_{31}^{\mathrm{mlt}}$ curve is also above the target only trinomial σ_{01}^{t} curve and approaches the BGM-T+P curve. The difference between the target-only trinomial cross section σ_{01}^{t} and $\sigma_{31}^{\mathrm{exc}}$ is much smaller in such slow collisions. It indicates that considering projectile electrons to be passive provides better results than it ought to, as ignorance of projectile electron removal compensates for neglecting transfer ionization.

At higher impact energies the $\sigma_{31}^{\mathrm{mlt}}$ and $\sigma_{31}^{\mathrm{exc}}$ curves converge, signalling that transfer-ionization processes do not play a noticeable role at those energies. Projectile electron loss is the only relevant consequence from taking active projectile electrons into account. It is thus remarkable that the BGM-T+P curve is above the multinomial curve, which seems to suggest that projectile electron loss is prevented. A possible explanation is that transfer to the projectile *K* shell is present in the multinomial calculation while the Pauli exclusion principle prevents it in the determinantal analysis. This will be analysed in more detail in section 5.1.3.

It is worthwhile to return to equation (91) in order to examine the

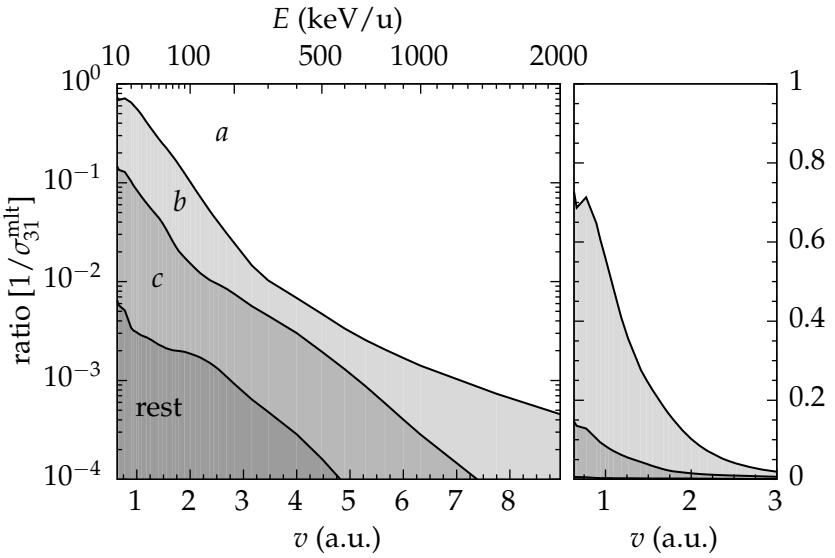

Figure 10: Cumulatively plotted ratios of the transfer ionization contributions in (91) to the multinomial pure single-ionization cross section $\sigma_{31}^{\mathrm{mlt}}$ for B^{2+}–Ne collisions. The same data are drawn against a logarithmic axis on the left and linear axis on the right. The labels *b*, *c* and 'rest' are explained in the text. The complement to the shaded areas (*a*) corresponds to direct target ionization P_{31}^{exc}.

terms that correspond to transfer ionization, labelled b, c and 'rest'. The ratios of these terms to the total multinomial cross section $\sigma_{31}^{\mathrm{mlt}}$ are shown in figure 10. Each term is added cumulatively to the sum of smaller contributions, such that the topmost line represents the ratio of all transfer ionization processes to the total $\sigma_{31}^{\mathrm{mlt}}$. In other words, the shaded area corresponds to transfer ionization while the complement corresponds to exclusive target ionization P_{31}^{exc}, labelled a in (91). Transfer ionization processes are the cause for more than a half of the overall multinomial cross sections at about 30 keV/u, whereas they contribute less than a percent to the overall multinomial cross section $\sigma_{31}^{\mathrm{mlt}}$ for impact energies above 500 keV/u.

Dominant for all impact energies are one-electron transfer processes, labelled b in (91) and figure 10. One electron of the target is captured by the projectile in coincidence with ionization of a projectile electron. Two-electron transfer processes (b) are less likely, at the lowest energies they contribute nearly an order of magnitude less than one-electron processes. Transfer processes where more than two electrons are exchanged between both centres contribute little to $\sigma_{31}^{\mathrm{mlt}}$, they are collectively shown as 'rest'.

The patterns observed for single-ionization curves in figure 9 are also present for pure double ionization, shown in figure 11, although, the differences between the curves are more pronounced. The multinomial expression for double ionization follows the same principle as (91):

$$\begin{aligned} P_{32}^{\mathrm{mlt}} = \quad & \overbrace{P_{02}^{\mathrm{t}} P_{00}^{\mathrm{p}}}^{a} + \overbrace{P_{11}^{\mathrm{t}} P_{01}^{\mathrm{p}}}^{b} + \overbrace{P_{12}^{\mathrm{t}} P_{10}^{\mathrm{p}}}^{c} + \overbrace{P_{21}^{\mathrm{t}} P_{11}^{\mathrm{p}}}^{d} \\ & + \underbrace{P_{22}^{\mathrm{t}} P_{20}^{\mathrm{p}}}_{e} + \underbrace{P_{20}^{\mathrm{t}} P_{02}^{\mathrm{p}} + P_{30}^{\mathrm{t}} P_{12}^{\mathrm{p}} + P_{32}^{\mathrm{t}} P_{30}^{\mathrm{p}}}_{\text{rest}} \end{aligned} \tag{93}$$

The terms are labelled as follows:

a is identical to the exclusive double target ionization P_{32}^{exc} (81),

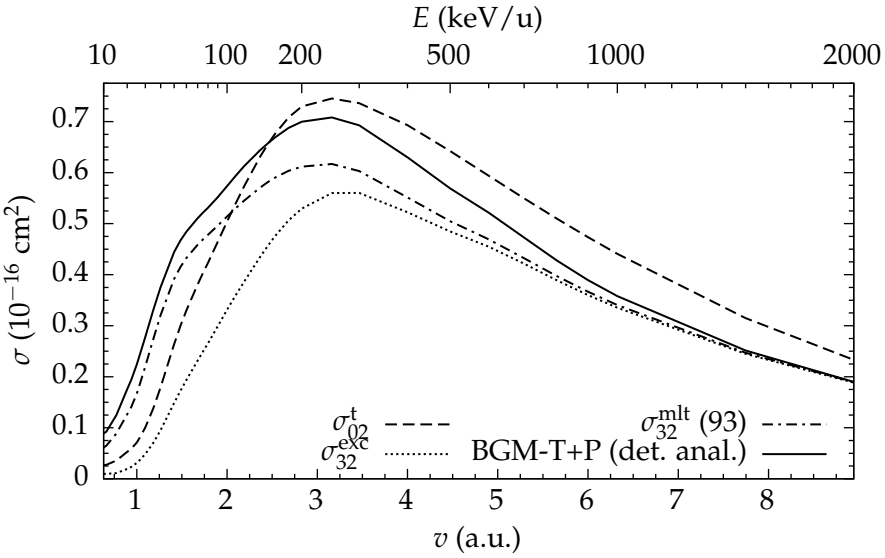

Figure 11: Double target ionization coincident with unchanged projectile charge state ($k = 3$, $l = 2$) cross sections for B^{2+}–Ne, calculated with a multinomial analysis considering active target and projectile electrons $\sigma_{32}^{\mathrm{mlt}}$ (93) (chain line); trinomial double target ionization σ_{02}^{t} (dashed line); exclusive target ionization $\sigma_{32}^{\mathrm{exc}}$ (dotted line); and BGM-T+P determinantal analysis (solid line). See the text for an explanation of the statistical methods used to calculate each cross section.

the probability to transfer two target electrons to the continuum while the projectile electrons remain at their ion.

b is a transfer ionization process where one electron is transferred from the target to the projectile and one electron from the target to the continuum coincident with the transition of one electron from the projectile to the continuum.

c is a transfer ionization process where one target electron is transferred to the projectile and two to the continuum coincident with the transition of one electron from the projectile to the target.

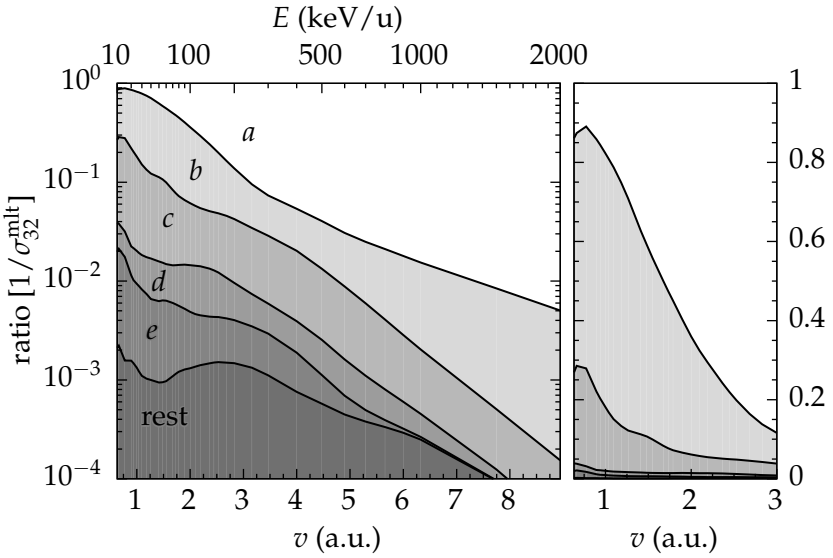

Figure 12: Cumulatively plotted ratios of the transfer ionization contributions in (93) to the multinomial pure double ionization cross section $\sigma_{32}^{\mathrm{mlt}}$ for B^{2+}–Ne collisions. The same data are drawn against a logarithmic axis on the left and linear axis on the right. The labels *b* to *d* and 'rest' are explained in the text. The complement to the shaded areas (*a*) corresponds to direct target ionization P_{32}^{exc}.

d is a transfer ionization process where two electrons are transferred from the target to the projectile and one is transferred from the target to the continuum coincident with one electron transferred from the projectile to the target and one transition from the projectile to the continuum.

e is a transfer ionization process where two electrons are transferred from the target to the projectile and two undergo transitions to the continuum while two electrons are transferred from the projectile to the target.

rest collects the remaining processes which involve the transfer of several electrons; they contribute very little to the multinomial probability P_{32}^{mlt}.

Comparing the cross sections $\sigma_{32}^{\mathrm{exc}}$ and σ_{02}^{t} in figure 11 shows that the more complex transfer ionization processes (b, c, etc.) play a very noticeable role at low to intermediate impact energies. The multinomial cross section σ_{02}^{t} which includes these processes approaches the cross section calculated with the determinant analysis of the BGM-T+P calculation for slow collisions. For fast collisions both the $\sigma_{32}^{\mathrm{exc}}$ and σ_{02}^{t} BGM-T+P curves converge, while the trinomial curve σ_{02}^{t}, where projectile electrons are considered passive lies about 10% above the active-electron curves. This indicates that projectile electron removal plays a significant role and that there are no noticeable effects of Pauli exclusion.

In figure 12 the ratios of the cross sections corresponding to these terms to $\sigma_{32}^{\mathrm{mlt}}$ are shown cumulatively. Transfer-ionization processes outweigh direct ionization at low impact energies. The simplest of these processes b where an electron of the projectile is lost to the continuum dominates the more complex process c where a projectile electron is transferred from the projectile to the target while two target electrons are directly ionized. The more complex processes, (d, e, 'rest') never contribute more than two percent to the total pure double ionization cross section.

5.1.3 *Pauli exclusion*

In the preceding section total cross sections that were calculated with two different approaches were discussed; namely, results of the determinantal and the multinomial analysis. In the determinantal analysis probabilities are calculated from inner products (57) of Slater determinants (4) for the propagated many-electron state and a final configuration. As the Slater determinants are fully antisymmetric many-electron wave functions (under particle exchange) the Pauli exclusion principle is adhered to in the analysis. The multinomial approach does not respect the antisymmetry of the many-electron state.

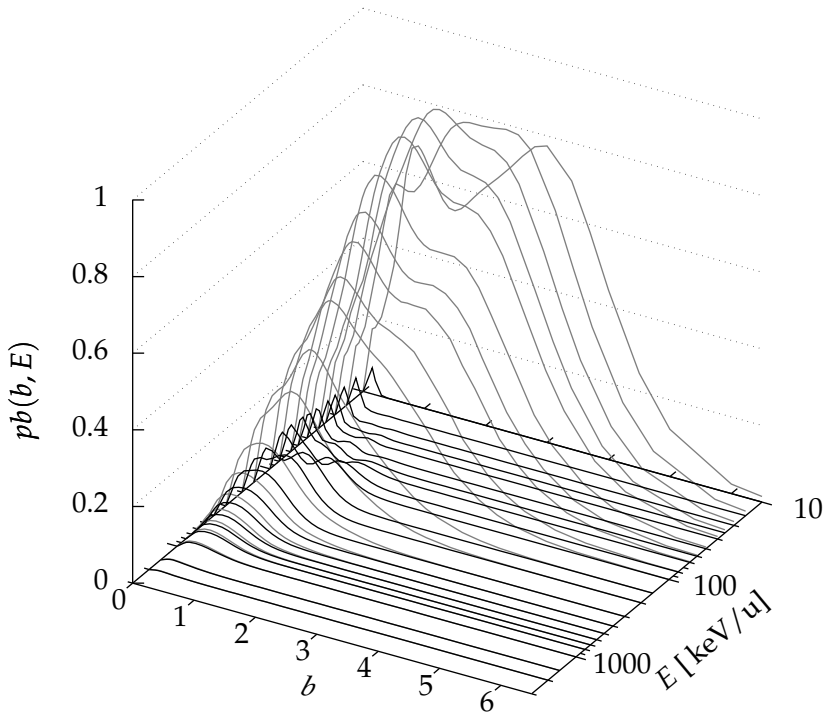

Figure 13: Impact parameter weighted capture probabilities $bp_{1s}^{\mathrm{p,c}}(b)$ from Ne to the B^{2+} $1s$ orbital (dark grey) in comparison to the weighted overall capture probabilities from Ne to B^{2+} $1s$ to $4f$ orbitals (light grey). Shown as a function of the impact parameter b and cascaded for decreasing impact energy E.

(a)

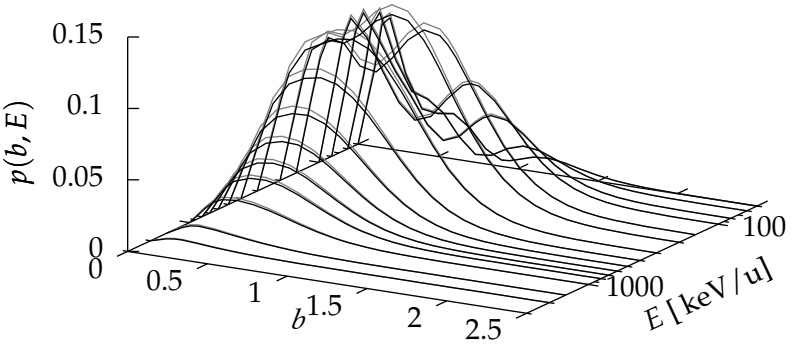

(b)

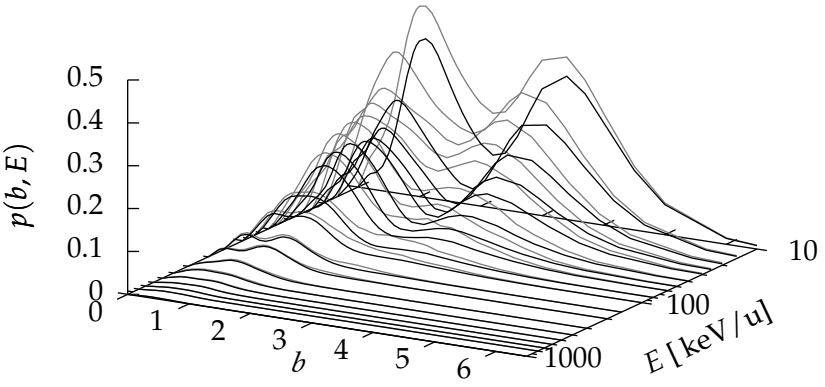

Figure 14: Weighted capture probabilities $pb(b,e)$ from B^{2+} $1s$ (a) and $2s$ (b) to the Ne L shell (black) in comparison to the overall transfer to the target (grey), as a function of impact parameter b and energy E.

Many-electron probabilities are obtained as combinatoric products of single-electron probabilities of independent events.

Figures 9 and 11 show discrepancies between the results of the determinantal method (BGM-T+P) and the multinomial method (P_{kl}^{mlt}). Since the input for the models, (transition amplitudes) as well as the scope (active target and projectile electrons) are the same for both, the observed differences must come from antisymmetry, or rather, from neglecting it. The first aspect to investigate is the missing convergence of the determinantal and multinomial results at high impact energies in figure 9. In that figure the BGM-T+P curve was found to be above the P_{kl}^{mlt} curve. A reason can be found in figure 13 where single-electron probabilities for target electron capture to the projectile $1s$ orbital are shown in comparison with overall capture (to $1s, \ldots, 4f$). While overall capture probabilities fall sharply with increasing impact energy, capture to the K shell reduces only slightly, such that from about 500 keV/u capture to the projectile K shell is the dominant capture channel. As the projectile $1s$ state is initially fully occupied and electron loss is weak this capture channel is suppressed by Pauli exclusion. A suppression of a process that changes the charge state of the projectile leads to an increase in the pure ionization channel σ_{31} – this is consistent with what is shown in figure 9 and what has been observed in a comparison of the multinomial and the determinantal final state analyses for He^+-Ne collisions [102].

The more pronounced differences between determinantal and multinomial results in figures 9 and 11, particularly noticeable at medium impact energies is not explained as directly. The problem is simpy too complex to pin it to a concrete cause.

Pauli exclusion might also matter for transfer to the projectile $2s$ orbital, which is initially occupied by one electron. Electron transfer from the projectile to the, initially fully occupied, target L shell is also noticeable. Figure 14 shows single-electron probabilities for transfer of projectile $1s$ (a) and $2s$ (b) electrons to the target L shell vs overall

electron transfer to the target. Transfer to the neon M and N shells from the projectile $1s$ orbital is negligibly small. At low impact energies transfer from the $2s$ orbital to these shells is present; transfer to the L shell, however, is clearly dominant. In fast collisions the situation is comparable to transfer from $1s$. Accordingly, one can expect transfer from the projectile to the target to be strongly suppressed by Pauli exclusion.

This puts the findings of section 5.1.2 for the contribution of transfer processes to pure target ionization into a slightly different light. Term (c) in the multinomial sum (91) is a process where a projectile electron is transferred to the target, and thus ought to be supressed by Pauli exclusion. However, in the multinomial results shown in figure 10 the contribution by term (c) is quite noticeable. This is also the case for terms (c), (d), (e) in (93) in figure 12. This does however not explain the difference between the BGM-T+P and $\sigma_{3l}^{\mathrm{mlt}}$ curves in figures 9 and 11. However, charge-state-coincident collision channels have a tendency to react sensitively to small changes that suppress other collision channels and in turn shift probability elsewhere. A similar increase of pure ionization cross sections calculated with the determinantal analysis was found in comparisions to results of analyses that do not adhere to the Pauli principle for He^+–Ne collisions [102]. This was explained as a consequence of Pauli blocking of capture to the helium ion [50, 102].

5.2 COMPARISON OF RESPONSE AND NO-RESPONSE CALCULATIONS

So far only results of no-response calculations have been discussed. In the no-response approximation target and projectile nuclei are screened by potentials that are, relative to the respective collision centre, constant in time. In the present IEM description the screening potentials consist of Hartree potentials and, in the case of the target, an exchange potential (cf. section 1.4). When removal probabilities are high the no-response approximation is too simplistic, since it does not address the reduction of screening during the collision. In the target-response model the screening potentials are scaled (21) with a factor that is a function of the net occupation of target states (22) (cf. section 1.3).

The present calculations used an implementation of the target-response model where observables at final time are extracted by projecting on initial target orbitals which leads to oscillations of resulting probabilities. The determinantal method (cf. section 3.1) was used for the statistical final-state analysis. These oscillations were investigated with the help of test calculations in section 4.2. The target-response cross sections shown in this section are averages of results found shortly before the end of the calculation (at five points between $R_{\mathrm{in}} = 40\,\mathrm{au}$ and $R_{\mathrm{in}}(t_{\mathrm{f}}) \approx 60\,\mathrm{au}$) which helps to reduce the effect these oscillations have on the results. In the following no-response results for He^{2+}- and B^{2+}-ion impact on neon are compared with results calculated with the target-response model (22).

5.2.1 *He^{2+}–Ne*

The comparison of target-response and no-response calculations is started with the He^{2+}–Ne collision system. A bare-ion projectile allows to focus on response without having to address the more complex processes that come with projectiles that carry electrons into

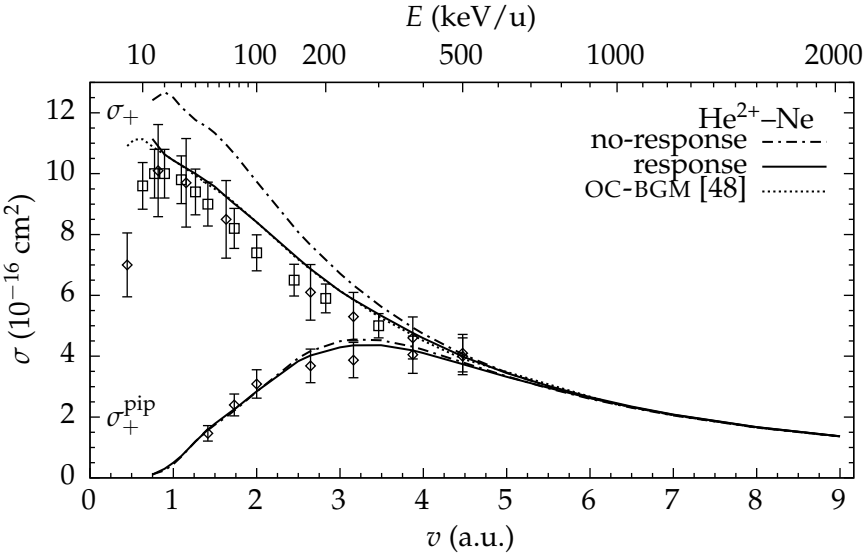

Figure 15: Comparison of the present no-response (chain line) and response (solid line) TC-BGM calculations for He^{2+}–Ne for net recoil ionization σ_+ and positive ion production σ_+^{pip} channels. Previous OC-BGM calculation with target response [48] (dotted line) Experimental data: [66] (squares), [67] (lozenges).

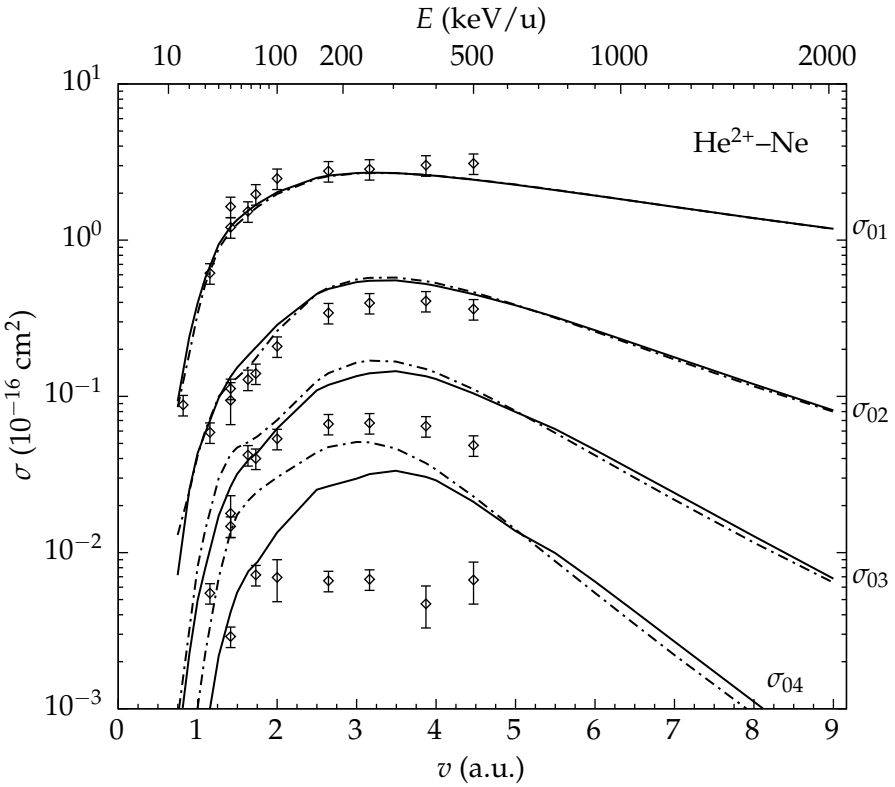

Figure 16: Comparison of no-response (chain line) and response (solid line) TC-BGM calculations for He^{2+}–Ne for pure multiple ionization σ_{01} to σ_{04}. Experimental data: [67] (lozenges).

the collision. Moreover, it also allows a direct comparison with the earlier OC-BGM target-response calculations of reference [48]. The OC-BGM calculations included states centred at the target and BGM-states generated from them. Transition probabilities were extracted by projecting on instantaneous eigenstates (option D in section 4.2) and on bound projectile states. No-response ionization cross sections calculated with the OC-BGM and the present TC-BGM match each other almost exactly (i.e. differences are not discernible at the scale of the figures). Differences between the OC-BGM and TC-BGM response results are due to differences of the implementation of the response model.

In figure 15 target-response and no-response results, for the net recoil ion production σ_+ and the positive ion production σ_+^{pip} are compared. Below 375 keV/u the *no-response* calculation overestimates the experimental net recoil ion production cross sections σ_+ [66, 67], whereas the *response* TC-BGM calculation is mostly in good agreement with the experiments. Nonetheless, for slow collisions the experimental data show a steep rise to a peak at about $v = 0.8$ au which is not present in the response TC-BGM calculation. The curve also exceeds the experimental error margins of several data points from reference [66] while following the trend of the data. The TC-BGM response curve is almost identical to that of the previous OC-BGM response calculation [48]. The most noticeable difference is the aforementioned peak structure for very slow collisions, which is present in the calculations from reference [48], while it is outside of the energy range where the present calculation is numerically stable.

The difference between response and no-response TC-BGM calculations is very small for the positive ion production cross sections σ_+^{pip}. The calculations are in very good agreement with the experimental data [67].

For fast collisions the response and no-response curves converge. As transitions become less likely with increasing impact energy the

net occupation is not changed as much and in turn the screening of the target is not reduced significantly. With a general reduction of single-electron removal probabilities comes also a shift from multiple to single target ionization. This collision channel is, on purpose, affected less by the present response model.

Pure multiple ionization total cross sections σ_{0l} for $l = 1, \ldots, 4$ are shown in figure 16. The response and no-response calculations yield nearly the same results for single σ_{01} and double ionization σ_{02} and are in good agreement with the experimental data [67]. The triple ionization results σ_{03} of both calculations begin to differ noticeably. The experiment is overestimated in fast collisions by the response as well as the no-response calculation. The former curve is lower in slow collisions and therefore marginally closer to the experiment. The response and the no-response calculations differ considerably, both in shape and maximum values for four-fold ionization σ_{04}. The experiment is considerably overestimated by both, where the no-response calculation does much worse than the response calculation. When describing k-fold pure ionization the present theory agrees with the experiment less and less as k increases. This observation is consistent with previous experience that IEM calculations tend to be reliable while $q_{\mathrm{t}}^{\mathrm{f}} \leq q_{\mathrm{p}}^{\mathrm{i}} + 1$ [48, 49, 103, 123, 126].

5.2.2 B^{2+}–Ne

The no-response results of section 5.1 (labelled BGM-T+P) are in the following compared with the results of a target-response calculation. In figure 17 the positive ion production $\sigma_{+}^{\mathrm{pip}}$ and the net recoil ion production σ_{+} are shown. The positive ion production $\sigma_{+}^{\mathrm{pip}}$ curves for the target-response and the no-response calculation are in close proximity over the whole velocity range and are in good agreement with the experimental data of [35]. For two data points corresponding to the slowest collisions the calculations underestimate the exper-

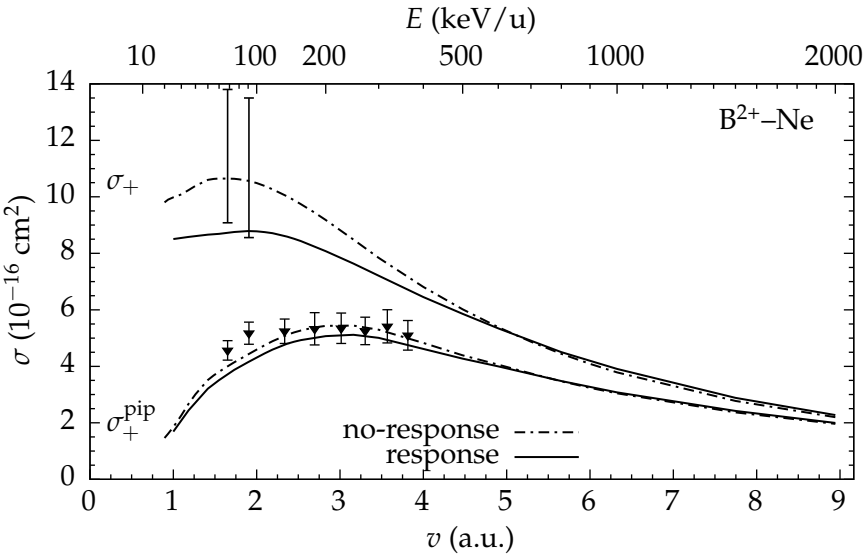

Figure 17: Comparison of response and no-response calculations. Net recoil ion production σ_+, and positive ion production σ_+^{pip} for B^{2+}–Ne. Experimental data points for σ_+^{pip} [35] (triangles). Bars mark a semi-empirically estimated range for σ_+ that is described in the text.

iment. The no-response curve is closer to these data points.

The difference between target-response and no-response calculations becomes more apparent when looking at the net recoil ion production σ_+, where no-response leads to considerably larger cross sections. Unfortunately, experimental net recoil ion production σ_+ results are not available for B^{2+}–Ne. However, while [35] provides pure ionization cross sections, capture and loss data from the same experimental group can be found in [62], though, without information about the coincident target charge state. This allows a semi empirical estimate that provides upper and lower limits for the net recoil ion production σ_+ which is shown in figure 17: The first estimate provides a lower bound for σ_+ by a sum of experimental cross sections for σ_{loss}, single capture $\sigma_{1\text{cap}}$, and double capture $\sigma_{2\text{cap}}$ from reference [62] and positive ion production σ_+^{pip} from reference [35]:

$$\sigma_+ \geq \sigma_{\text{loss}} + \sigma_+^{\text{pip}} + \sigma_{1\text{cap}} + 2\sigma_{2\text{cap}}. \tag{94}$$

This presumes a somewhat unlikely situation where loss and single capture lead only to a final target charge state $q_{\text{f}}^{\text{t}} = 1$ and double capture leads to $q_{\text{f}}^{\text{t}} = 2$. The second estimate also uses results of the present calculation for a semi empirical estimate. Correction factors to compensate for the lack of target charge state information in the experimental data through ratios $\rho_k = (\sum_l l\sigma_{kl})/)(\sum_l \sigma_{kl})$ are obtained from the no-response caculations (68 keV/u: $\rho_2 = 1.5$, $\rho_4 = 1.5$, $\rho_5 = 2.5$; 90 keV/u: $\rho_2 = 1.5$, $\rho_4 = 1.7$, $\rho_5 = 3$). Due to the tendency of the IEM to overestimate multiple ionization it is reasonable to assume that the ratios ρ_k would overestimate actual factors were they to be found in experiments. With the ρ_k factors (94) becomes:

$$\sigma_+ \approx \rho_2\sigma_{\text{loss}} + \sigma_+^{\text{pip}} + \rho_4\sigma_{1\text{cap}} + \rho_5\sigma_{2\text{cap}}$$

Experimental data for 90 keV/u are provided in both articles, how-

ever, data for 68 keV/u are missing in [62] and are linearly interpolated. Experimental errors are considered by using the worst case assumptions of $\sigma \pm \Delta\sigma$ for lower and upper estimates. The target-response curve lies below the lower estimate at 68 keV/u and lies barely in the estimated range at 90 keV/u. Results of the no-response calculation are within the estimated range at both impact energies.

While the target-response and no-response calculations for the positive ion production σ_+^{pip} differed only slightly, the more detailed picture of the pure multiple target ionization cross sections σ_{3l} for $l = 1, \ldots, 5$, that constitute σ_+^{pip} (90), is more differentiated. This is shown in figure 18. For pure single target ionization σ_{31} both calculations yield nearly identical results. Also for pure double target ionization σ_{32} the two methods differ only slightly. When looking at $\sigma_{33}, \ldots, \sigma_{35}$ the difference between the target-response model and the no-response approximation becomes more pronounced. For low to mid impact energies the no-response curves are above the target-response curves. For triple ionization the no-response calculation is in very good aggreement with the experimental results [35] while the target-response model leads to underestimation of the experiment. The experimental four-fold ionization results are overestimated by the no-response calculation, while the target-response curve is below the data at low impact energies and passes through at higher energies. The no-response curve overestimates five-fold ionization considerably. While the target-response results still exceed the experiment they are much closer. As mentioned in the context of He^{2+} impact (figure 16), the IEM calculation tends to increasingly overestimate experimental results (see also section 5.1.1) as the number or removed electrons rises. In the case of B^{2+} impact this happens to a much lesser degree, even the present σ_{34} results are in fair agreement with the experiment.

The nearly identical results for single ionization and very similar

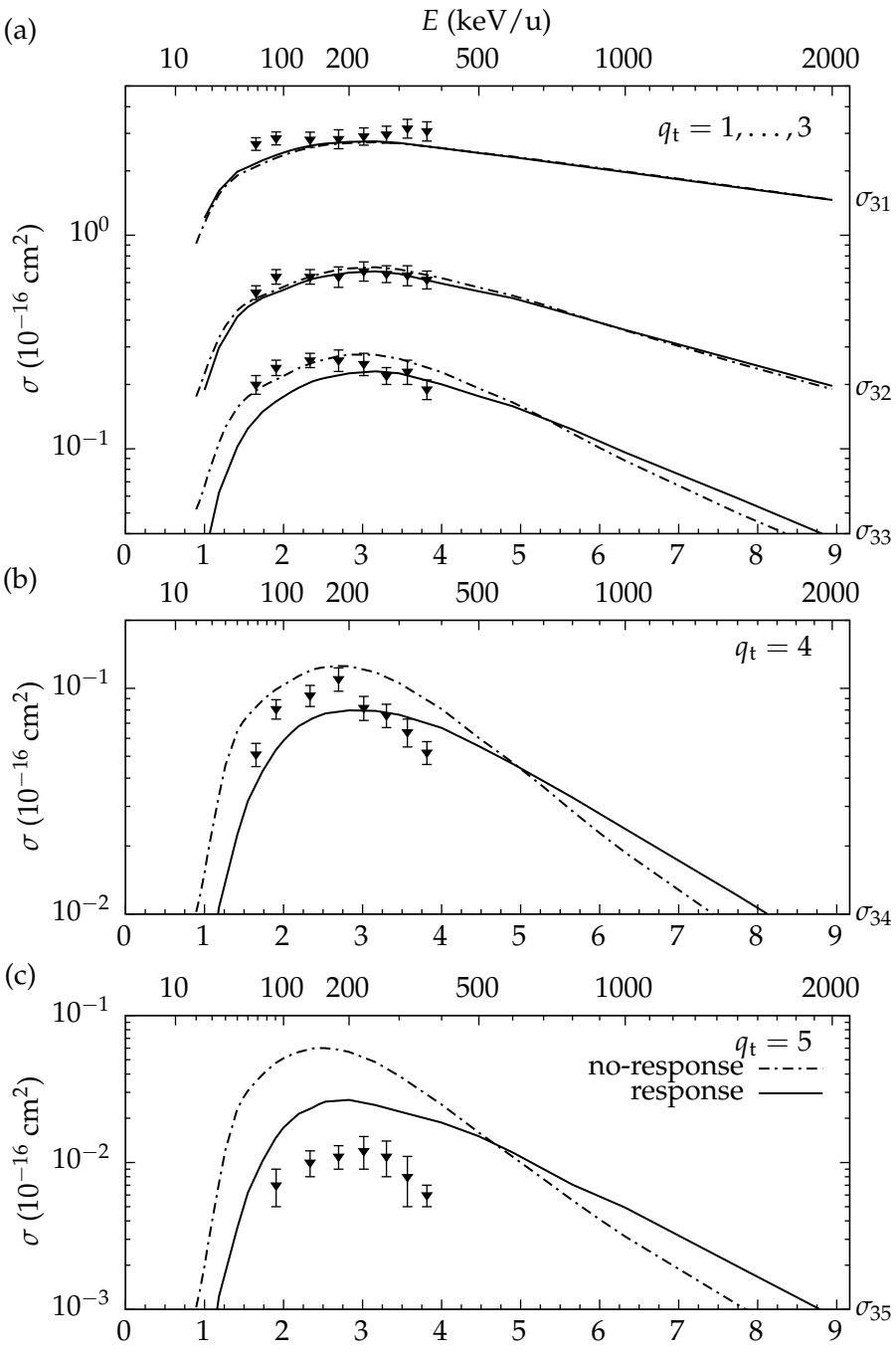

Figure 18: Total cross sections for pure multiple ionization of neon by B^{2+} impact: single to triple $\sigma_{31}, \ldots, \sigma_{33}$ (a), four-fold σ_{34} (b), and five-fold σ_{35} (c) target ionization. Results of a TC-BGM calculations with a target-response model (solid line) and with the no-response approximation (chain line) are shown. Experimental data [35] (triangles).

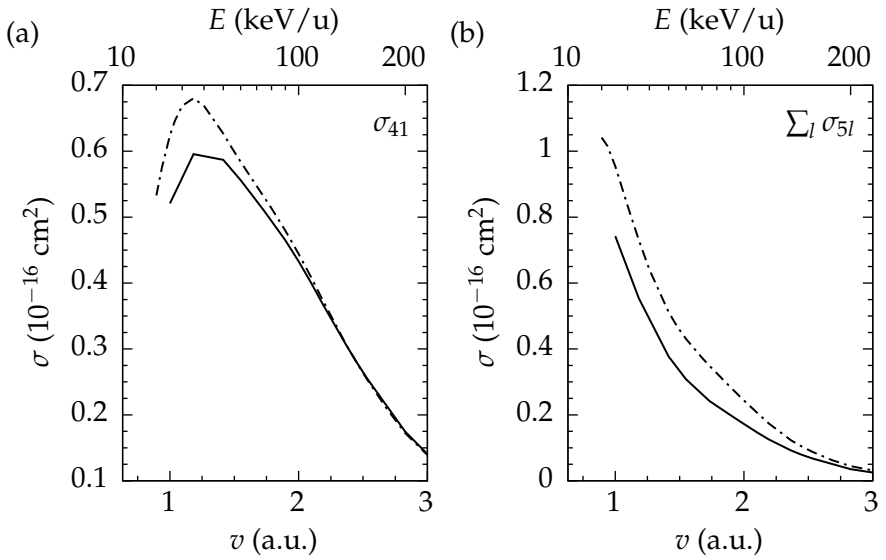

Figure 19: Transfer ionization σ_{41} (a) and double capture $\sum_l \sigma_{5l}$ (b) for B^{2+} impact on neon. Results of TC-BGM target-response (solid line) and no-response (dash-dotted line) calculations.

results for double ionization are caused by the soft onset of the present target-response model (22). When the number of removed electrons increases and the screening potential is scaled down in the global response model the target becomes more attractive, and the remaining, now more strongly bound, electrons are less likely to be removed.

Also noteworthy in figure 18 is that at high energies the curves corresponding to both models do not converge. The target-response results exceed those of the no-response calculation. This points to the problem discussed in section 4.2. Projecting the response solutions on initial atomic eigenstates in the final-state analysis leads to the overall increased target ionization at high-impact energies.

The inclusion of target response has only a minor influence on the agreement of the present capture results with experimental data. Single-capture cross sections σ_{40} are nearly identical in the present target-response and no-response calculations (therefore a direct comparison is not shown here; target-response capture cross sections will

be shown in section 5.3 though).

The effect of response is more noticeable in collision channels where more electrons are removed from the target. Two examples for such channels are shown in figure 19: Transfer-ionization σ_{41} is noticeably reduced in slow collisions by including response in the present model. The target-response double capture cross sections $\sum_l \sigma_{5l}$, that comprise pure capture as well as transfer ionization, are below the no-response results over the whole impact-energy range where capture is a relevant target electron removal process. In absolute terms the differences of the two models for these channels are small on the scale of the net recoil ion production channel σ_+ (figure 17). Nonetheless, the transfer ionization processes lead to high target charge states q_t^t, which due to weighting increases their effect on σ_+. As such differences between target-response and no-response calculations occur for many channels they cumulate and can explain the considerable reduction of the target-response σ_+ curve.

Remarks

The present target-response model (21,22) was used for the ion–neon calculations that will be discussed in the following (viz. sections 5.3 – 5.6). The use of this model is supported by the overall better agreement of the He^{2+}–Ne target-response results with experimental data. The comparison of no-response and response calculations for the B^{2+}–Ne collision system was somewhat inconclusive. For several collision channels the no-response calculations are in better agreement with experimental results than the target-response calculations. However, in these cases the difference between both calculations is not large, and the target-response results are still in fair agreement with the experimental data.

Neglecting the time dependence of the mean field potentials in the no-response approximation would risk to oversimplify the problem.

At the lower end of intermediate impact energy range collisions take long in comparison to the time scale of electron dynamics (cf. figure 5). The electronic density has enough time to react, which ought to be reflected in the effective potential of the target.

5.3 CHANGED PROJECTILE CHARGE STATE

In section 5.1 the focus was on pure target ionization channels, that is, target ionization coincident with unchanged final projectile charge state. Electron transfer and projectile electron loss played a role in removing probability from the pure ionization collision channels. In section 5.2 the focus was still on ionization channels in the comparison of the target-response and the no-response descriptions. Now the focus will shift to collision channels where the final projectile charge state is changed as well. The total cross sections shown in this section are results of the B^{2+}–Ne target-response calculations that were discussed in section 5.2. The determinantal method was used for the statistical final-state analysis.

5.3.1 *Projectile electron loss*

The choice of effective potentials in the present common–mean-field description (cf. section 1.4) prioritizes the correct description of electrons initially at the target. Electrons of both centres are propagated with the single-electron Hamiltonian (23). With this Hamiltonian the target atom is too attractive and the projectile ion is not attractive enough to electrons initially at the projectile, because the target is not entirely screened at asymptotic distances, and the exchange potential is omitted in the projectile effective potential. The consequence can be seen in figure 20 where total cross sections for projectile electron loss

$$\sigma_{\mathrm{ls}} = \sum_{l=1}^{N_{\mathrm{t}}+1} \sigma_{kl} \quad \text{for } k = N_{\mathrm{p}} - 1 \tag{95}$$

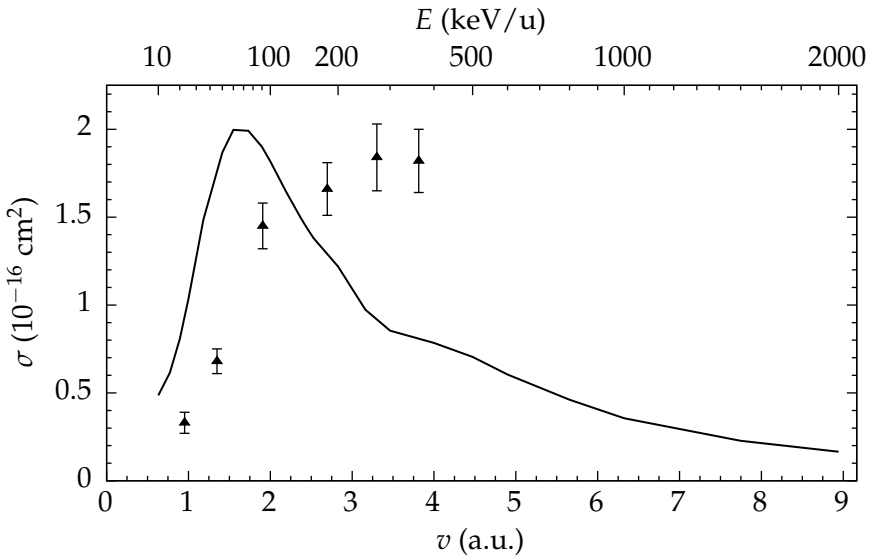

Figure 20: Projectile electron loss σ_{ls} (95) in B^{2+}–Ne collisions. Electron transfer to the target that leads to a negative neon ion ($k = 2$, $l = 0$) is omitted. Experimental data: [62].

are shown: In slow collisions calculated cross sections are about three times higher than the experimental data [62]. Up to its peak at about 70 keV/u the curve rises with increasing impact energy similar to the experimental data. The present results fall short of the experimental cross section for $v > 2$ au. The reason is that antiscreening is not described in the present model. Antiscreening is understood as projectile ionization due to a direct interaction of the active electron with electrons of the other centre, and it is the dominant mechanism for electron loss from B^{2+} at intermediate to high impact energies [62]. It can be approximated by electron impact ionization of the projectile ion [127]. The probability of an electron being transferred to the continuum in an antiscreening process increases with the number of electrons at the collision partner [128]. Due to the large difference of the numbers of initial electrons at the neon atom and boron ion (viz. $N_{\mathrm{t}} = 10$, $N_{\mathrm{p}} = 3$) the effect of antiscreening on target ionization channels is not as pronounced as what is observed

at the projectile.

The asymmetry of the collision system helps with the channels that are coincident with projectile electron loss.[2] Due to the large number of target electrons the weight of target electron procesess in the statistical analysis is greater. Furthermore, with increasing initial projectile-ion charge state the effect of the wrong asymptotic potentials is mitigated. While the target remains too attractive, the projectile electrons are more strongly bound in the first place.

5.3.2 *Capture*

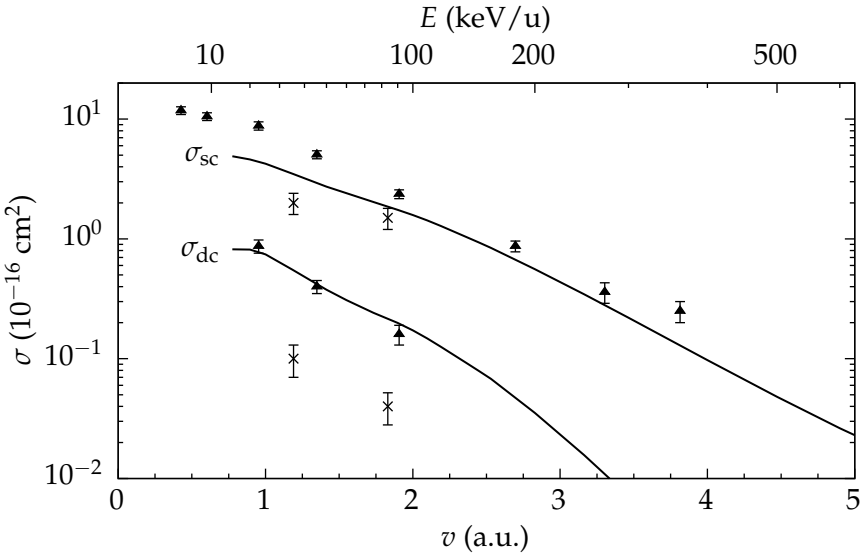

Figure 21: Total cross sections for single capture σ_{sc} (96) and double capture σ_{dc} (97) of neon electrons by B^{2+} projectiles; present target-response calculations (lines). Experimental data: [62] (filled triangles), [129] (exes).

More important in the description of the B^{2+}–Ne collision system

[2] The incorrect asymptotic behaviour of the Hamiltonian for projectile electrons will also be discussed in chapter 6 for He^+–He collisions. Due to the greater symmetry of that collision system the influence of the wrong asymptotic behaviour of (23) is much more pronounced.

are capture processes, namely, processes where the number k of electrons found at the projectile at t_f is greater than N_p. This can be seen at the scale of the graph in figure 21 showing the capture channels of the present calculations, its maximum is about 5 times larger than that of the previous figure. Shown in figure 21 are cross sections for single capture,

$$\sigma_\mathrm{sc} = \sum_l \sigma_{4l}, \tag{96}$$

and double capture,

$$\sigma_\mathrm{dc} = \sum_l \sigma_{5l}. \tag{97}$$

The present single-capture results underestimate the experimental data by Wolff et al [62], in particular in slow collisions. Nonetheless, the theoretical curve shows a similar trend and drops off with increasing energies in the same way the experimental data do. Single capture results by Dmitriev et al [129] are well below the cross sections that were measured by Wolff et al [62]. The present calculations fall between the two sets of experimental data.

The present results for double capture, σ_dc (97) appear to be in very good agreement with the experimental data by Wolff et al [62], however, this may be only fortuitous: It was argued that dynamic and final-state correlations have to be considered when describing capture of multiple electrons [130]. The IEM tends to somewhat overestimate these correlated processes [131–133].

5.4 PROJECTILE CHARGE-STATE-COINCIDENT MULTIPLE IONIZATION

In the previous sections all three cases with regard to the final projectile charge state have been discussed: unchanged charge state, focusing on multiple target ionization (section 5.1.1); projectile electron loss and capture to the projectile. In the discussion of the latter two

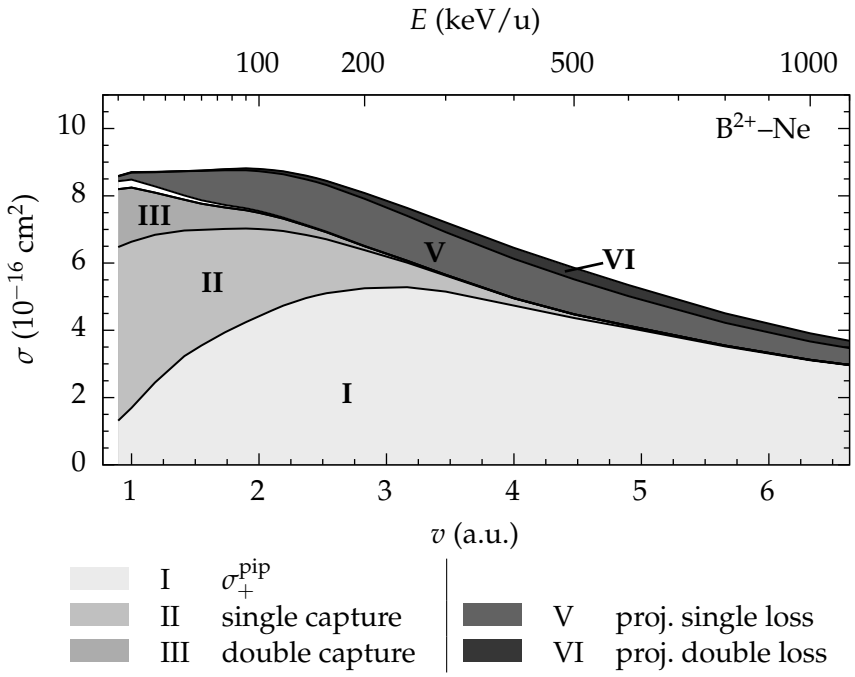

Figure 22: B^{2+}–Ne net recoil ion production σ_+ and the terms in (98) contributing to it.

the target charge state did not matter (section 5.1). In this section the focus returns again to multiple target ionization, but unlike in section 5.1 the contributions of loss and capture processes are also investigated. These contributions are substantial – as already noted in the context of figure 6 where the large gap between the net recoil ion production σ_+ and the positive ion production σ_+^{pip} was apparent.

The results shown in this section have been calculated with the TC-BGM using the target-response model The determinant method has been used for the final-state analysis All results have been published in [124].

The recoil ion production σ_+ can be found as a sum of cross sections for q_t-fold ionization (weighted with q_t) (56). The terms in the sum can be ordered to make explicitly visible the coincident projectile charge state the cross sections σ_{kl} correspond to. Written in this way (56) for the B^{2+}–Ne collision system is:

$$\begin{aligned}\sigma_+ = \overbrace{\sigma_+^{\mathrm{pip}}}^{\mathrm{I}} + \overbrace{\sum_{l=0}^{7}(l+1)\sigma_{4l}}^{\mathrm{II}} + \overbrace{\sum_{l=0}^{6}(l+2)\sigma_{5l}}^{\mathrm{III}} + \cdots \\ + \underbrace{\sum_{l=1}^{9}(l-1)\sigma_{2l}}_{\mathrm{V}} + \underbrace{\sum_{l=2}^{10}(l-2)\sigma_{1l}}_{\mathrm{VI}} + \cdots .\end{aligned} \tag{98}$$

Term (I) is the positive ion production σ_+^{pip}, which was already shown in figure 6. Term (II) is a net ionization quantity for processes where electrons are removed from the target in coincidence with single capture by the projectile. Term (III) is the analogous quantity for double capture. Processes where more than two electrons are captured by the projectile are included in σ_+. However, since they would lead to a negative ion, they are not labelled and collected with the first ellipsis in (98). That such cross sections, σ_{kl} for $k > Z_\mathrm{p}$, emerge – and can be quite large, as will be shown below – is a shortcoming of the

statistical models used in this work.[3] Related to this, there is no term labelled (IV) in (98), it will be needed for capture by triply-charged ions later in this chapter. The terms labelled (V) and (VI) are net cross sections of target ionization processes that are coincident with projectile electron loss.

In figure 22 the contributions of the terms (I) to (VI) are shown. The curve at the bottom corresponds to the positive ion production σ_+^{pip}, denoted (I) in (98). The following terms (II) to (VI) are cumulatively added in the figure, for example, the sum of terms (I) and (II) corresponds to the curve that forms the upper limit of the area labelled (II). As an aside, the value of (II) is not the same as the single capture cross section σ_{sc} (96), the difference comes from the weighting with $l+1$ in (98). These transfer ionization processes are the largest contributions to σ_+ at the lowest impact energies, and do contribute significantly at intermediate impact energies as well.

Transfer ionization where two electrons are captured by the boron-ion (III) are significant only below about 100 keV/u. Loss from the projectile coincident with target ionization occurs almost over the whole impact energy range, and is negligible only for the slowest collisions. Single electron loss (V) is the dominant collision channel, the loss of two electrons (VI) contributes noticeably only for collisions faster than $v = 2$. Target ionization coincident loss of all three electrons initially at the B^{2+}-ion is extremely unlikely and would not be visible on the scale of the plot. One has to keep in mind that the present model is rather inaccurate when it comes to projectile electron loss. In slow collisions (ca $v < 2$ au) this channel is overestimated while at high energies (ca $v > 2$ au) it is considerably underestimated (cf. figure 20).

[3] The product of binomials method of [47] addresses this problem. The method redistributes the events that would lead to un-physical multiple capture to the other capture channels [48]. Its drawbacks are that it does not preserve unity in the probabilities that result from it and, since it is in essence a binomial combination approach, does not adhere to the Pauli principle.

With the addition of target ionization coincident double electron loss the net recoil ion production σ_+ is completed, that is, the uppermost curve shows σ_+. However, there is one area that is not labelled in the figure, which corresponds to unphysical processes, in particular, triple capture to the B^{2+}-ion. The combinatoric approach that is used in the present statistical final-state analyses (in the determinantal analysis equation (64) ff.) includes all mathematically possible combinations of k and l. The corresponding area in the figure is left blank [the small area is between (III) and (V)].

Of note is, that the net recoil ion production σ_+ curve would not shift if the statistical model were flawless. Since σ_+ (55) is the product of an observable $P^{\mathrm{t}}_{\mathrm{net}}$ (21) that is directly obtained without the help of the statistical model its value is not affected by the IEM statistical insufficiencies.[4]

5.5 TRIPLY CHARGED IONS

In this section results calculated with the present model for the C^{3+}–Ne and Li^{3+}–Ne collision systems are discussed in the context of experimental data. This is done in preparation for a discussion where several ion–neon collisions systems are compared, which is to follow in section 5.6. The calculations for the triply charged ions were performed using the TC-BGM with the target-response model (21). For the C^{3+}-ion eigenfunctions of the nuclear potential screened by the OPM Hartree potential [73] were used. Hydrogen-like orbitals were used for Li^{3+}. The BGM bases in in the C^{3+} and Li^{3+} calculations were built with the same hierarchy as that used for B^{2+} and He^{2+} impact calculations (cf. section 4.1). Basis convergence for the C^{3+}–Ne and the Li^{3+}–Ne collision systems was similarly good as for the B^{2+}–Ne

[4] Incidently, were the projectile loss channel correct in the model, it would not change the σ_+ curve either. The target net occupation does not depend on the projectile occupation. However, it would matter in a description that considered projectile response.

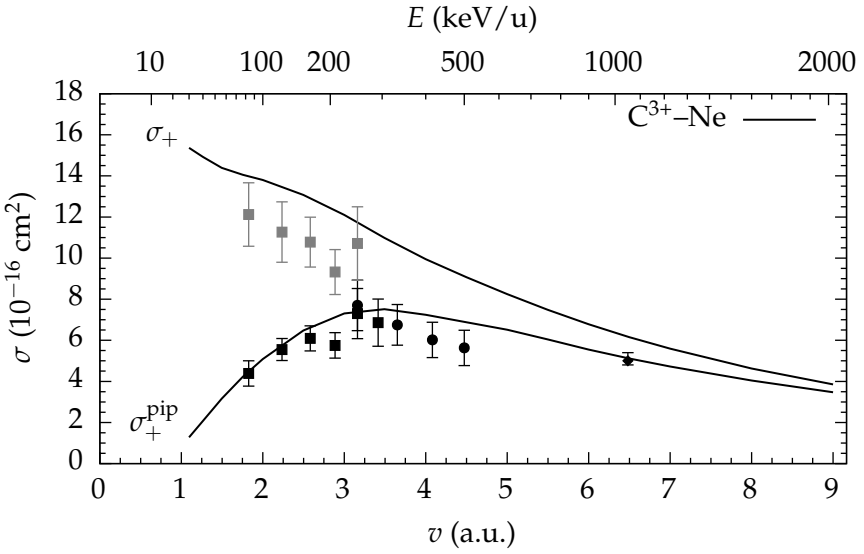

Figure 23: Net recoil ion production σ_+ (56) and positive ion production σ_+^{pip} (90) for C^{3+} impact on neon. Experimental data: σ_+^{pip}: [52] (squares), [64] (circles); σ_+: [56] (diamond) (at $v = 6.5$ au), a lower bound for the net recoil ion production calculated (99) from [52], (grey squares).

collision system.

5.5.1 *Carbon-ion impact*

The positive ion production σ_+^{pip} and the net recoil ion production σ_+ by C^{3+} impact on neon are shown in figure 23. Experimental data were published for the σ_+^{pip} channel at intermediate impact energies [52] (83 keV/u to 292 keV/u), [64] (250 keV/u to 500 keV/u). and for the σ_+ channel at 1 MeV/u [56]. The present σ_+^{pip} results are in fair agreement with experimental data [52, 64]. Although the calculations do not show a structure at 200 keV/u and overestimate the experiment [64] towards higher impact energies the curve reflects the overall shape of the data rather well.

The single datum for net recoil ion production σ_+ from reference [56] is somewhat overestimated by the calculation. From experi-

mental data for projectile electron loss and capture in reference [52] a lower bound for the net recoil ion production

$$\sigma_+ \geq \sum_{l=2}^{5}(l-1)\sigma_{2l} + \sum_{l=1}^{4} l\sigma_{3l} + \sum_{l=0}^{4}(l+1)\sigma_{4l} \tag{99}$$

can be calculated. While it lacks the contributions from ionization coincident with multiple capture and loss processes, it is not too far fetched to assume that the included processes reflect the general trend of $\sigma_+(E)$ reasonably well. With the exception of one considerably raised datum, the present results lie above and agree with the shape suggested by the lower bound for σ_+ (99).

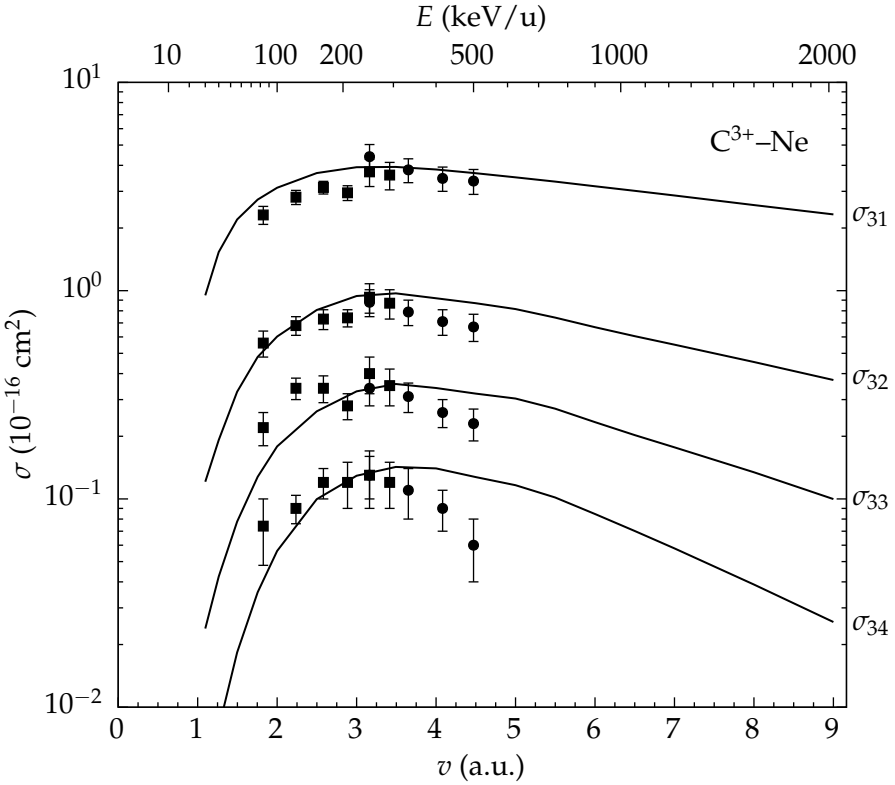

Figure 24: Pure multiple ionization $\sigma_{31}, \ldots \sigma_{34}$ in C^{3+}–Ne collisions. Experimental data: [52] (squares), [64] (circles).

In figure 24 the present calculations for pure multiple ionization σ_{3l}, $l = 1, \ldots, 4$, are compared with experimental results [52, 64]. Although the experiment is slightly overestimated and a trough at about 200 keV/u does not appear in the calculations, overall the present results agree well with the experimental σ_{31} and σ_{32} of [52]. The present calculations are in good agreement with experimental data of reference [64] for σ_{31} and σ_{32}. For higher final charge states of the neon target, the calculations $\sigma_{33}, \ldots, \sigma_{34}$, are altogether in fair agreement with both experiments [52, 64]. A trend to increasingly underestimate the data at low impact energies and overestimate them at high impact energies is noticeable. With increasing l the agreement of the present results for the C^{3+}–Ne σ_{3l} does not degrade as much as it does in the B^{2+}–Ne collision system (cf. figure 8).

Capture σ_{40} and transfer ionization cross sections $\sigma_{41}, \ldots, \sigma_{43}$, that is, transition of one to three target electrons to the continuum coincident with the capture of one electron by the projectile, are shown in figure 25. The present calculations are mostly in good agreement with experimental data [52, 64]. An exception are the σ_{40} and σ_{41} data points of reference [52] at 292 keV/u, which also do not agree with the data for the same impact energy of reference [64]. At higher impact energies the calculated capture cross section σ_{40} drops below the cross section for transfer ionization. This is reflected in the data of [64], where σ_{41} exceeds σ_{40} for fast collisions. At low impact energies the experiment is somewhat underestimated by the present results in all four channels included in the figure. The transfer-ionization process σ_{43} that leads to the highest target charge state $q_t = 4$ is overestimated at high impact energies, and does not fall off as steeply as the experimental data suggest.

Figure 26 shows total cross sections for multiple ionization coincident with single projectile electron loss $\sigma_{22}, \ldots \sigma_{25}$. Projectile electron loss is not well described in the present model (cf. section 1.4) and in

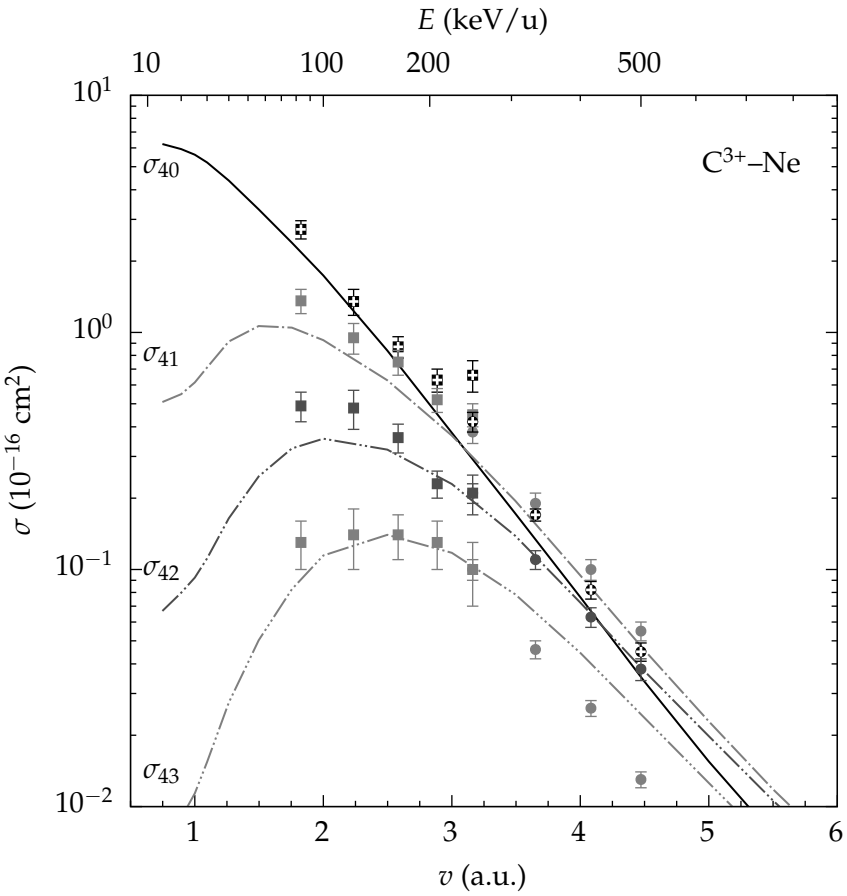

Figure 25: Total cross sections for target electron capture σ_{40} and transfer ionization $\sigma_{41}, \ldots, \sigma_{43}$ in C^{3+}–Ne collisions. Experimental data: [52] (squares), [64] (circles).

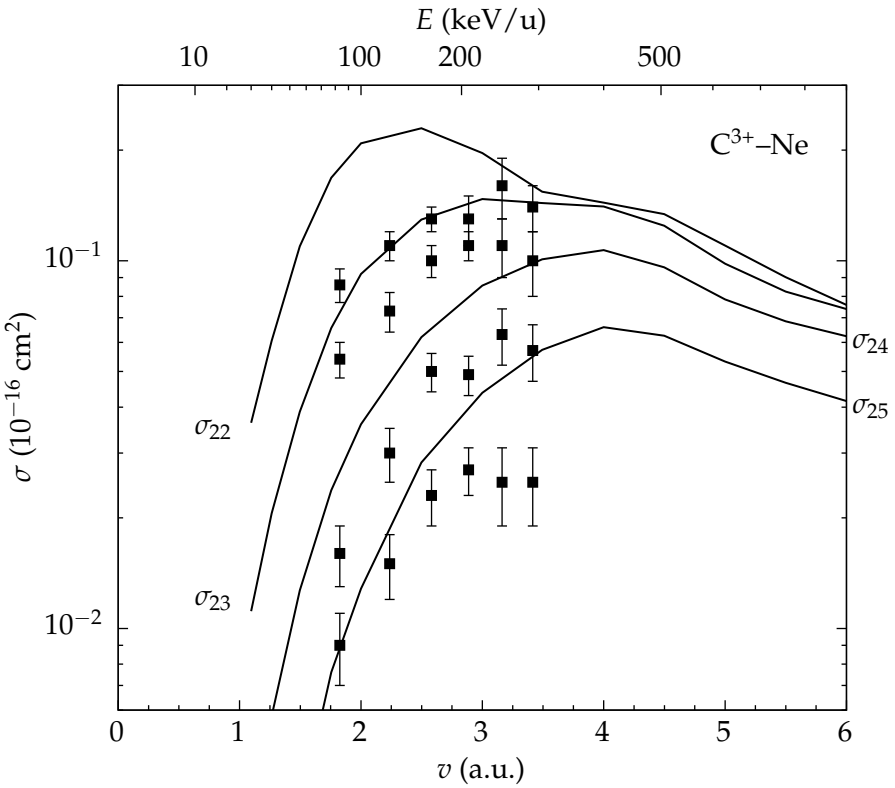

Figure 26: Multiple ionization of Neon by C^{3+} impact coincident with electron loss from the latter, $\sigma_{22}, \ldots \sigma_{25}$. Experimental data: [52] (squares), [64] (circles).

comparison with the experiment [52] it shows the pattern observed for B^{2+} impact (cf. section 5.3.1): In slow collisions projectile electron loss σ_{22} is considerably overestimated and at intermediate impact energies the σ_{22} curve drops off. This pattern becomes less noticeable when more target electrons are removed, $\sigma_{23}, \ldots \sigma_{25}$. Apparently, the coincidence with the less likely double and higher target ionization suppresses the exaggerated projectile electron removal in these channels in the statistical model.

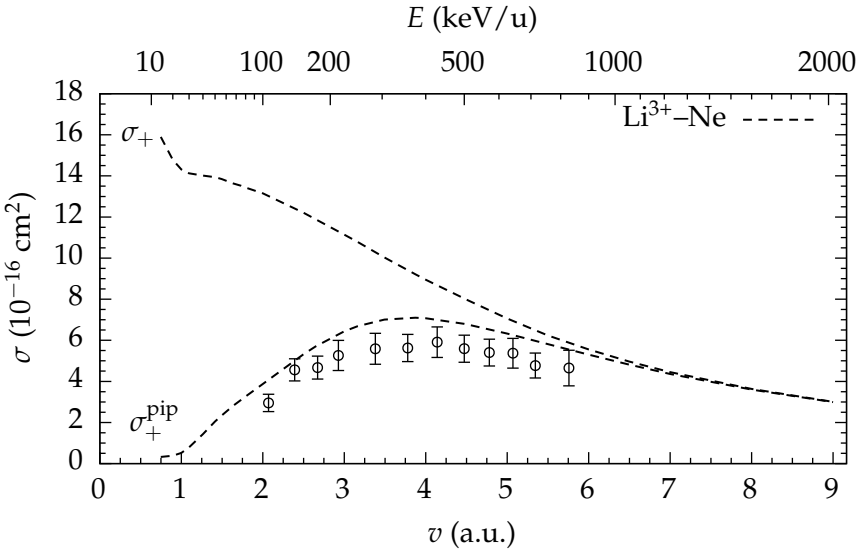

Figure 27: Net recoil ionization σ_+ (56) and positive ion production σ_+^{pip} (90) for Li^{3+} impact on a Ne target. Experimental data: σ_+^{pip}: [64] (circles).

5.5.2 *Lithium-ion impact*

Present results for the positive recoil ion production σ_+^{pip} in neon by Li^{3+} impact are compared with experimental results [64] in figure 27. The theoretical results are in good agreement with the experiment. While the experiment is slightly overestimated by the present theory, the curve follows the shape suggested by the experimental data closely. No experimental net recoil ionization σ_+ cross sections for Li^{3+}–Ne are currently available in the literature.

Total cross sections for pure multiple target ionization σ_{0l}, $l = 1, \ldots, 4$, are shown in figure 28. The present results for σ_{01} agree very well with the experimental data [64]. With increasing l however, the present theory overestimates the experiment more and more. For ionization to the highest charge state included in the comparison, $l = 4$, the theoretical curve is only close to the experimental data points at the lowest impact energies which might be coincidental.

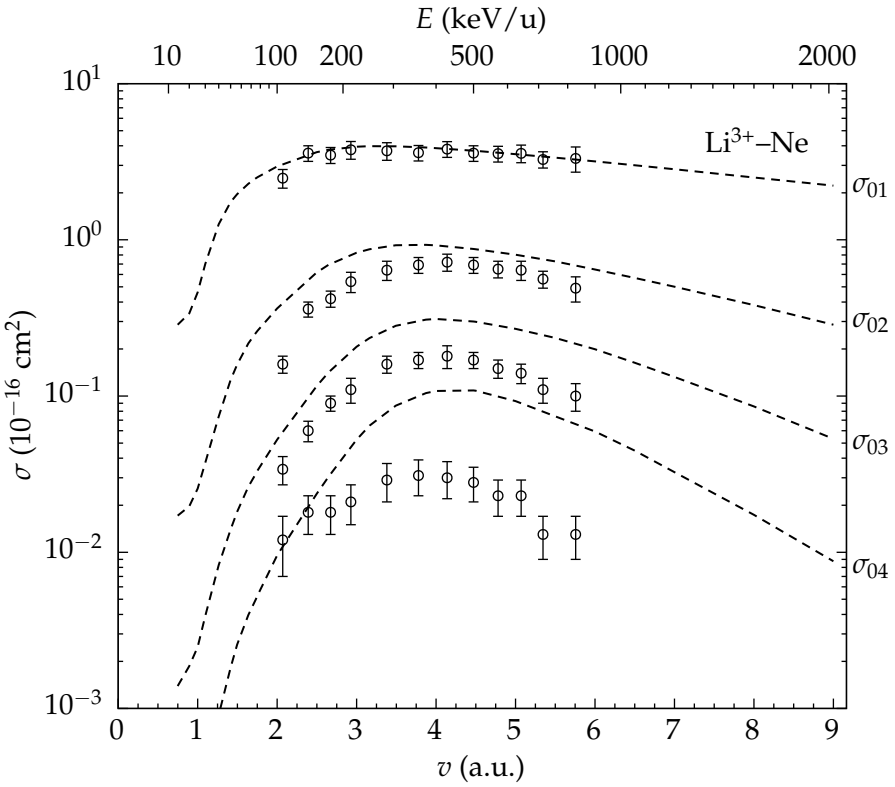

Figure 28: Pure multiple ionization $\sigma_{01}, \ldots \sigma_{04}$ in Li^{3+}–Ne collisions. Experimental data: [64] (circles).

The theoretical description of l-fold ionization by (bare) Li^{3+}-ion impact agrees well with the experiment only up to smaller l than it does for (dressed) C^{3+}-ion impact.

5.6 COMPARISON OF BARE- AND DRESSED-ION IMPACT

In this section ionization by equicharged bare- and dressed-ion impact on neon is compared. The theoretical curves are results of target-response TC-BGM calculations and the determinantal final-state analysis was used. This perspective on dressed-ion collisions is interesting because it allows to see the role of projectile electrons by comparing two systems that can also be observed in experiments. The results of the present theory for B^{2+}, He^{2+}, C^{3+}, and Li^{3+} impact on neon have been compared with experimental results in sections 5.2, 5.3, and 5.5. Since the present theory was found in overall good agreement with the experiments for target ionization collision channels, the comparison of dressed- and bare-ion impact can be discussed solely with the help of the present theoretical results.

5.6.1 *Doubly charged projectiles*

B^{2+} and He^{2+} impact on neon are compared directly in figure 29 which shows the net recoil ion production σ_+ (56) and positive ion production σ_+^{pip} (90). The curves were discussed in the context of figure 17 (B^{2+}–Ne) and figure 15 (He^{2+}–Ne). The positive ion production σ_+^{pip} by B^{2+} impact exceeds that of He^{2+} impact by a margin that is almost constant over the whole impact energy range. In slower collisions ($E \leq 100\,\text{keV/u}$) the gap between the σ_+^{pip} curves widens slightly. In section 5.1.2 a gain for the B^{2+}–Ne pure ionization channels from transfer-ionization processes that led to an unchanged charge state was found for this impact energy range. Since such transfer-ionization processes are not possible in bare-ion collisions it may be responsible for the widening of the margin.

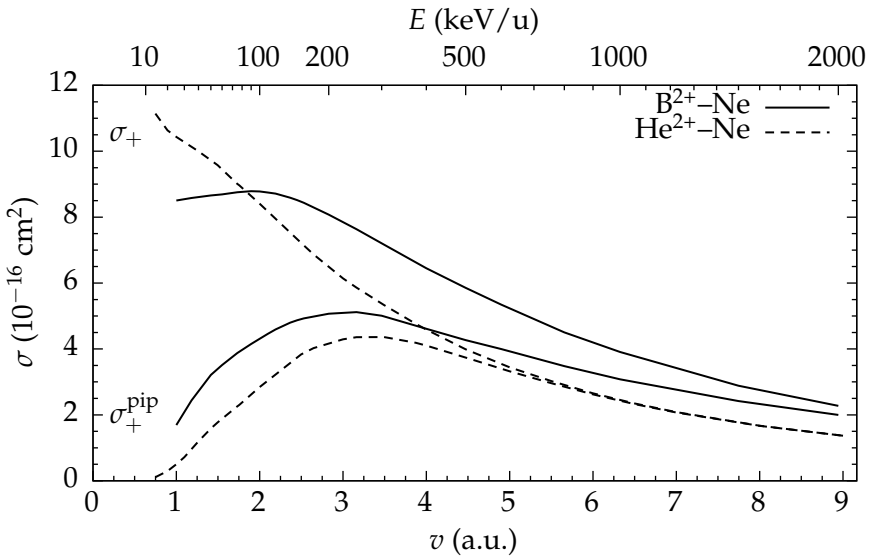

Figure 29: Net recoil ion production σ_+ (56), and positive ion production $\sigma_+^{\rm pip}$ (90) for B^{2+} and He^{2+} impact on a Ne target.

The net recoil ion production σ_+ by B^{2+} impact exceeds that by He^{2+} projectiles in fast collisions, both curves have a similar shape in this regime. The B^{2+} curve shows a local maximum at about $v = 2\,\text{au}$, while the He^{2+} curve rises further for slower collisions. Remarkably, in the slowest collisions considered the He^{2+} cross section is considerably higher than the B^{2+} one. This is unexpected, as typically dressed-ion impact leads to increased ionization compared to bare-ion impact. The reasoning behind this expectation is: While at large internuclear distances $R_{\rm in}$ (before the collision and for large impact parameters) the $q_{\rm p}/r$ Coulomb tail of both types of projectiles is the same, when the charge densities of projectile and target overlap at small internuclear distances $R_{\rm in}$ the $Z_{\rm p}/r$ nuclear potential is

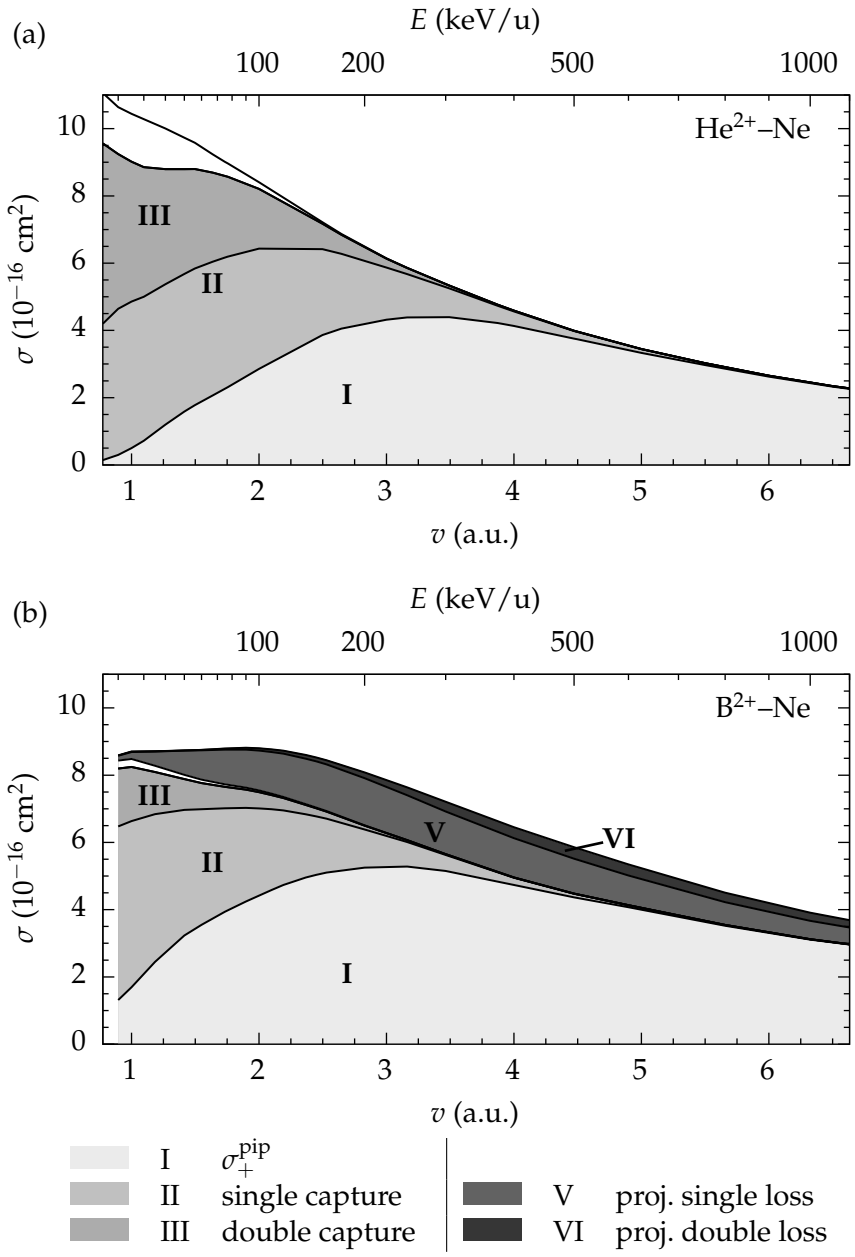

Figure 30: He^{2+}–Ne (a) and B^{2+}–Ne (b) net recoil ion production σ_+ and the terms in (100) and (98), respectively, contributing to it. Panel (b) shows figure 22 again, to ease direct comparison.

not entirely screened.[5] An explanation for the unexpected behaviour can be found in figure 30 where the contributions to the net recoil ion production σ_+ ordered by projectile charge state coincidence are shown for He^{2+}–Ne and B^{2+}–Ne collisions. (The B^{2+}–Ne plot has been shown previously, in section 5.4.) The terms for He^{2+}–Ne are labelled following the conventions of (98) as follows:

$$\overbrace{\phantom{\sigma_+^{\mathrm{pip}}}}^{\mathrm{I}} \quad \overbrace{\phantom{\sum_{l=0}^{7}(l+1)\sigma_{1l}}}^{\mathrm{II}} \quad \overbrace{\phantom{\sum_{l=0}^{6}(l+2)\sigma_{2l}+\cdots}}^{\mathrm{III}}$$

$$\sigma_+ = \sigma_+^{\mathrm{pip}} + \sum_{l=0}^{7}(l+1)\sigma_{1l} + \sum_{l=0}^{6}(l+2)\sigma_{2l} + \cdots . \qquad (100)$$

Comparing the plots for He^{2+} impact and B^{2+} impact the much larger size of the areas labelled (II) and (III) in the former is evident. This translates to increased single capture (II) and double capture (III) cross sections by He^{2+} impact. The latter is only a minor contribution to σ_+ in B^{2+}–Ne collisions, whilst in He^{2+}–Ne collisions it contributes nearly as much to σ_+ as single capture. Moreover, while collision processes where more than two electrons are captured by the doubly charged projectile ions account only for a minor increase of σ_+ for the B^{2+}projectile [the empty gap between (III) and (V) in figure 30 (b)], it increases σ_+ considerably for slow He^{2+} impact.

While such capture processes are an artefact of the statistical model used in the final-state analysis, the net recoil ion production σ_+ is unaffected by the statistical models as via (55) it depends on the target net occupation $P^{\mathrm{t}}_{\mathrm{net}}$ (28) only. In other words, a statistical model that

[5] The expectation of increased ionization by dressed ions led to models where dressed ion impact is described with the help of an effective charge of the projectile, for example in CTMC caclulations [39]. Experimental values for such an effective charge can be obtained from ratios of cross sections for bare and dressed ion impact [35, 64, 134], for example [35],

$$Z_q^{\mathrm{eff}} = 2\left[\sigma_q(B^{2+})/\sigma_q(He^{2+})\right]^{1/2q}.$$

In the case of He^{2+}–Ne and B^{2+}–Ne such an approach could lead to an effective charge that is smaller than the actual charge state of the projectile.

were to avoid such capture processes would also lead to slightly different results for all other collision channels – effectively increasing the other areas in figure 30 (a) in such a way that they add up to the same σ_+, which is determined by (55). The regions labelled (V) and (VI) are absent in the He^{2+}–Ne plot, as they correspond to processes that are coincident with projectile electron loss. Accordingly, unlike in dressed-ion impact the σ_+ and σ_+^{pip} curves for bare ion impact converge in fast collisions.

5.6.2 *Triply charged projectiles*

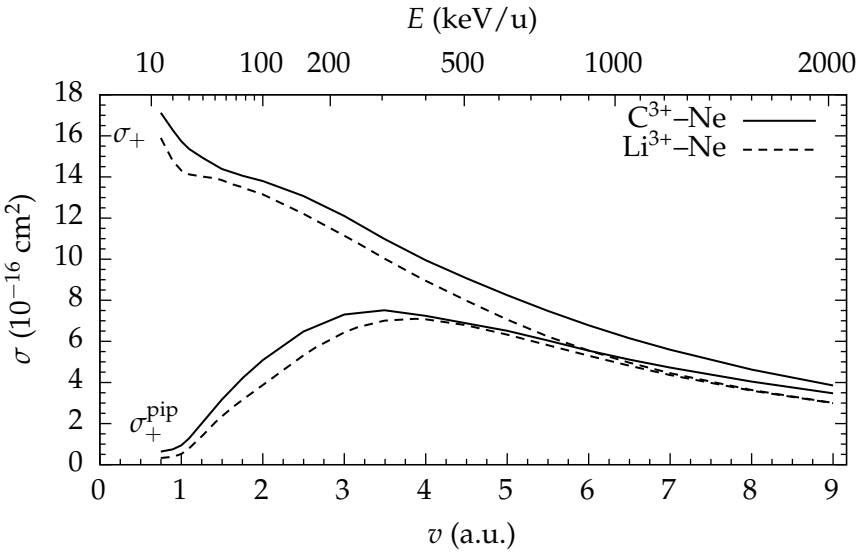

Figure 31: Net recoil ion production σ_+ (56) and positive ion production σ_+^{pip} (90) for C^{3+} and Li^{3+} impact on a Ne target.

Unlike in the case of doubly-charged ion impact the net recoil ion production σ_+ curves for Li^{3+} and C^{3+} impact on neon in figure 31 do not intersect. The net recoil ion production σ_+ by dressed-ion impact exceeds that by bare-ion impact by a fairly consistent margin over the whole impact energy range. Like the Li^{3+} curve the C^{3+} curve rises with decreasing impact energy. Other than in the case for

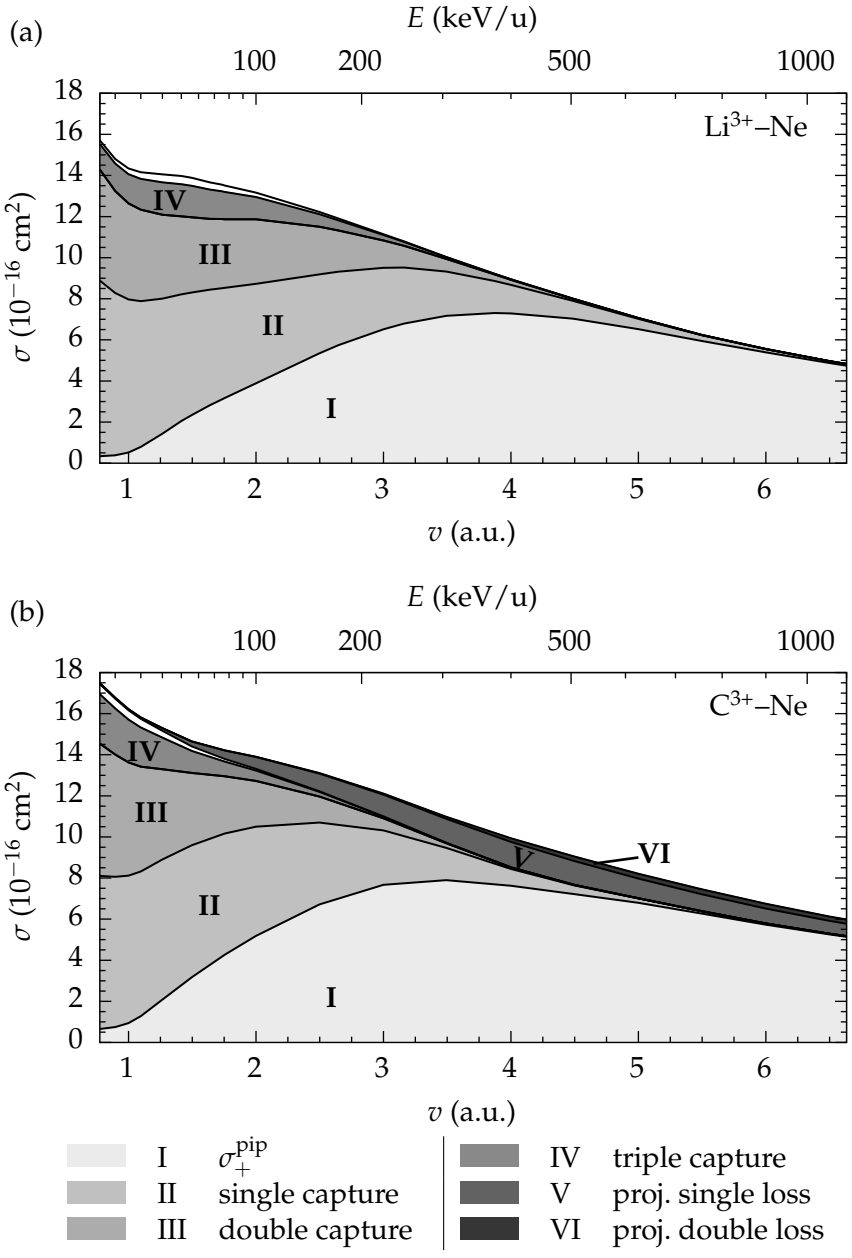

Figure 32: Li^{3+}–Ne (a) and C^{3+}–Ne (b) net recoil ion production σ_+ and the terms in (101) and (102), respectively, contributing to it.

collisions with doubly charged ions the Li^{3+} and C^{3+} σ_+ curves are steepest at the lowest impact energies. In particular, the C^{3+} curve has no local maximum.

The positive ion production σ_+^{pip} results due to Li^{3+} and C^{3+} impact differ only by a small margin. The gap is the largest between $v \approx 1\,\text{au}$ and $v \approx 4\,\text{au}$, this is also the regime where transfer processes are dominant – a hint that complex transfer ionization processes might increase the positive ion production in the C^{3+}–Ne collision system as well (cf. B^{2+}–Ne, section 5.1.2). In fast collisions the gap between the σ_+^{pip} curves widens again, ionization in this regime is more and more caused by close collisions, where the stronger nuclear charge of the C^{3+} is relevant.

The contributions to the net recoil ion production σ_+ are shown in figure 32 for Li^{3+} impact (a) and C^{3+} impact (b) on neon. The convention of (98) is used here as well. Explicitly, the equations for the Li^{3+} projectile are,

$$\sigma_+ = \overbrace{\sigma_+^{\text{pip}}}^{\text{I}} + \overbrace{\sum_{l=0}^{7}(l+1)\sigma_{1l}}^{\text{II}} + \overbrace{\sum_{l=0}^{6}(l+2)\sigma_{2l}}^{\text{III}} + \overbrace{\sum_{l=0}^{5}(l+2)\sigma_{3l}}^{\text{IV}} + \cdots ; \tag{101}$$

while for the C^{3+} projectile

$$\begin{aligned}\sigma_+ = {} & \overbrace{\sigma_+^{\text{pip}}}^{\text{I}} + \overbrace{\sum_{l=0}^{7}(l+1)\sigma_{4l}}^{\text{II}} + \overbrace{\sum_{l=0}^{6}(l+2)\sigma_{5l}}^{\text{III}} + \overbrace{\sum_{l=0}^{5}(l+2)\sigma_{6l}}^{\text{IV}} + \cdots \\ & + \underbrace{\sum_{l=1}^{9}(l-1)\sigma_{2l}}_{\text{V}} + \underbrace{\sum_{l=2}^{10}(l-2)\sigma_{1l}}_{\text{VI}} + \cdots .\end{aligned} \tag{102}$$

The equations differ from (100) and (98), respectively, only by writ-

ing out and labelling the triple-capture term (IV). For impact by triply charged ions capture plays a noticeable role in faster collisions than it did in the case of doubly charged ion impact. The contributions by transfer ionization processes to σ_+ show for the Li^{3+} projectile a similar overall pattern to that observed for the He^{2+}–Ne system. The contribution by double capture (III) is less significant, however. Three-fold capture (IV) contributes noticeably to σ_+. Capture of more than three electrons makes up only a very small part of the total. Because such processes become increasingly unlikely the deficiency of the statistical analysis that yields these un-physical results does not weigh as much for the triply–charged-ion projectiles as it did for the doubly–charged-ion projectiles.

For the C^{3+}–Ne collision system the contributions by transfer ionization processes (II–IV) to σ_+ are very similar to those for Li^{3+}–Ne. This again is unlike the observations for collisions with doubly charged projectiles, where for B^{2+} impact ionization coincident with double capture (III) contributes noticeably less to the total. The apparently smaller contribution of loss-ionization (V) and (VI) in the C^{3+}–Ne system than in the B^{2+}–Ne system can be explained by the different scales. Cross sections for projectile electron loss are similar for both projectile ions, but the net recoil ion production σ_+ is considerably larger in the case of the triply charged projectile.

As was mentioned above, the net recoil ion production σ_+ in collisions of neon with the doubly charged projectiles He^{2+} and B^{2+} shows an unexpected pattern where σ_+ by the bare ion exceeds that by the dressed ion at low impact energies. Such a pattern is not apparent for impact by Li^{3+} and C^{3+} ions on neon, and, indeed, figure 32 demonstrates that capture processes are similarly strong for both projectiles.

6 ASYMPTOTIC CORRECTION IN HELIUM-ION–HELIUM COLLISIONS

In chapter 1 starting from a TDHF ansatz single-electron equations (9) and (11) were developed for electrons initially at the target and at the projectile, respectively. Section 1.4 introduced three ways to combine the target and projectile problems. In the first approach (i) the coupled–mean-field method, electrons of each centre are evolved in time independently with either the target Hamiltonian (23) or projectile Hamiltonian (24). This approach served only as a reference in the present work, it has been used in references [51, 101, 102]. In (ii), the common–mean-field (CMF) approach, initial target and projectile electrons are evolved in time with the same target Hamiltonian (23). The ion–neon collision results discussed in chapter 5 were calculated with the CMF approach. A third approach was so far only fleetingly mentioned in the present work. The concept of (iii) is to use a common Hamiltonian for target and projectile electrons that is defined piecewise. N electrons are evolved in time with this Hamiltonian in order to preserve the orthogonality of the propagated states, similar to the CMF approach. At the same time the Hamiltonian is constructed in a way that leads to the correct asymptotic behaviour for electrons of both centres at initial time t_0, when a large internuclear distance is presumed.

For potentials V_t and V_p with the respectively correct asymptotic

behaviour the ansatz for such a Hamiltonian is [135]:[1]

$$\hat{h}(\boldsymbol{r}) = -\frac{1}{2}\Delta + \min\big(V_\mathrm{t}(\boldsymbol{r}), V_\mathrm{p}(\boldsymbol{r})\big). \tag{103}$$

Initial target and projectile wave functions $\psi_i(t)$, $i = 1, \ldots, N$ are propagated in the single-electron equations (25) with (103). The potentials are defined through $\hat{h} = \hat{T} + \hat{V}$ from the single-electron Hamiltonians of the target (23) (in no-response form, $a = 1$) and the projectile (24). Written out they are

$$V_\mathrm{t}(\boldsymbol{r}) = -\frac{Z_\mathrm{t}}{r_\mathrm{t}} + v^\mathrm{t}_\mathrm{ex}(r_\mathrm{t}) + v^\mathrm{t}_\mathrm{Ha}(r_\mathrm{t}) - \frac{Z_\mathrm{p}}{r_\mathrm{p}} + v^\mathrm{p}_\mathrm{Ha}(r_\mathrm{p}), \tag{104}$$

$$V_\mathrm{p}(\boldsymbol{r}) = -\frac{Z_\mathrm{t}}{r_\mathrm{t}} + v^\mathrm{t}_\mathrm{Ha}(r_\mathrm{t}) - \frac{Z_\mathrm{p}}{r_\mathrm{p}} + v^\mathrm{p}_\mathrm{ex}(r_\mathrm{p}) + v^\mathrm{p}_\mathrm{Ha}(r_\mathrm{p}). \tag{105}$$

Both equations differ only by including exclusively the target v^t_ex or projectile exchange potential v^p_ex. This allows to re-write (103), with a minimum function of exchange potentials only

$$\hat{h}(\boldsymbol{r}) = -\frac{1}{2}\Delta - \frac{Z_\mathrm{t}}{r_\mathrm{t}} + v^\mathrm{t}_\mathrm{Ha}(r_\mathrm{t}) - \frac{Z_\mathrm{p}}{r_\mathrm{p}} + v^\mathrm{p}_\mathrm{Ha}(r_\mathrm{p}) + \min\big(v^\mathrm{t}_\mathrm{ex}(r_\mathrm{t}), v^\mathrm{p}_\mathrm{ex}(r_\mathrm{p})\big). \tag{106}$$

In the following this approach will be called asymptotic correction (AC) approach. At large internuclear distances the minimum function selects the exchange potential of the closer centre since the exchange potentials are attractive (cf. figure 2). At t_0 for an electron at the target, $r_\mathrm{t} \ll r_\mathrm{p}$ (cf. p. 12), and (106) is in effect identical to the single-electron target Hamiltonian (23), because the electronic probability density vanishes long before it reaches the interface (near

[1] With the following definition of the minimum function:

$$\min\left[f(\boldsymbol{x}), g(\boldsymbol{x})\right] = \begin{cases} f(\boldsymbol{x}) & \text{for } f(\boldsymbol{x}) < g(\boldsymbol{x}) \\ g(\boldsymbol{x}) & \text{otherwise} \end{cases}$$

where $f, g : \mathbb{R}^3 \to \mathbb{R}$.

$r_t = r_p$) in the potential function. By the same token, for a projectile electron at t_0 and $r_p \ll r_t$, (106) is in effect identical to the single-electron projectile Hamiltonian (24).

At closer internuclear distances positions for which the probability density of target electrons does not vanish reach those regions of space where $v_{ex}^{p}(\boldsymbol{r}) < v_{ex}^{t}(\boldsymbol{r})$, and the minimum function takes the value of v_{ex}^{p} (vice versa for projectile electrons). Target electrons are then propagated in a Hamiltonian that is in effect different from that of the CMF approach. (The interface of the piecewise Hamiltonian is not necessarily near $r_t = r_p$ at distances where the exchange potentials do not approach the asymptotic limit.)

When the internuclear distance after the collision becomes large again the interface of the piecewise Hamiltonian does not matter any more in the propagation of electrons. However, unlike before the collision, the charge state of target and projectile is in general fractional and the notion of a *correct* asymptotic behaviour is not suitable any more.

6.1 THE HE^+–HE COLLISION SYSTEM

He^+ impact on He has been chosen to test the AC approach in no-response TC-BGM calculations. For the neon-ion collision systems (cf. chapter 5) one can argue that the incorrect asymptotic behaviour for projectile electrons in the CMF Hamiltonian is acceptable due to the great differences between the nuclear potentials and between the numbers of initial electrons, and that the relative error of omitting the projectile exchange potential is not large due to the high initial charge state of the projectile ions (cf. 1.4). For the He^+–He collision system, due to its greater symmetry, these arguments are not compelling, which was a reason to develop the AC approach in the first place.

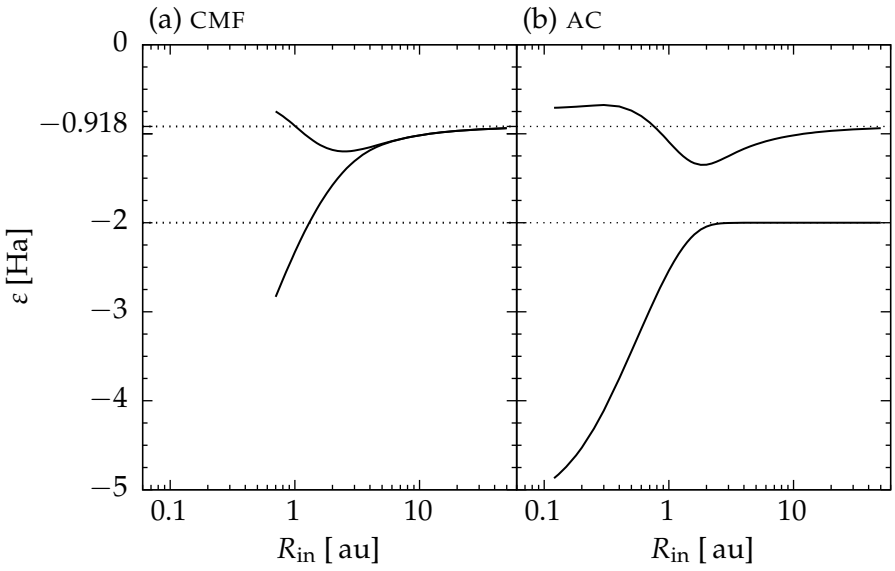

Figure 33: The two lowest energy eigenvalues ε as functions of the internuclear distance R_{in} for the He^+–He system, for the single-electron Hamiltonians: (a) CMF (108), and (b) AC (109). (Below $R_{\mathrm{in}} = 0.6$ au the CMF calculation is numerically unstable.)

In spin-restricted HF for a two-electron spin-singlet system the modulus of the exchange potential is half the Hartree potential; i.e. for the helium atom the exchange potential compensates for self-interaction only. For convenience one can define the screening potential

$$v_{\mathrm{s}} = \frac{v_{\mathrm{Ha}}}{2} = |v_{\mathrm{ex}}|. \tag{107}$$

The Hartree potential of the He^+ ion is assumed half of the Hartree potential of the helium atom, and thus identical to v_{s}. With the screening potentials of target and projectile v_{s}, that differ only by being centred at $\boldsymbol{R}_{\mathrm{t}}$ and $\boldsymbol{R}_{\mathrm{p}}$, respectively, the single-electron Hamiltonian (23) of the no-response CMF approach can be written as [135]:

$$\hat{h} = -\frac{1}{2}\Delta - \frac{2}{r_{\mathrm{t}}} + v_{\mathrm{s}}(r_{\mathrm{t}}) - \frac{2}{r_{\mathrm{p}}} + v_{\mathrm{s}}(r_{\mathrm{p}}). \tag{108}$$

At internuclear distances $R_{\mathrm{in}} \to \infty$ the eigenfunctions of the stationary SE are helium atomic orbitals for both centres. This can be seen in figure 33 (a) where the energy eigenvalues ε with respect to the CMF Hamiltonian (108) are shown as a function of the internuclear distance R_{in}: With increasing internuclear distance the energy eigenvalues approach $\varepsilon = -0.918\,\mathrm{Ha}$ which is the helium $1s$ eigenvalue of the OPM [73] atomic orbital.

The Hamiltonian (106) of the AC written with v_{s} is:

$$\hat{h} = -\frac{1}{2}\Delta - \frac{2}{r_{\mathrm{t}}} - \frac{2}{r_{\mathrm{p}}} + v_{\mathrm{s}}(r_{\mathrm{t}}) + \min\left[v_{\mathrm{s}}(r_{\mathrm{t}})\,,\; v_{\mathrm{s}}(r_{\mathrm{p}})\right]. \tag{109}$$

Energy eigenvalues with respect to this Hamiltonian are shown in figure 33 (b). The lowest eigenvalue approaches $\varepsilon = -Z_{\mathrm{p}}^2/2 = -2\,(\mathrm{Ha})$ for $R_{\mathrm{in}} \to \infty$, which corresponds to the hydrogen-like ground state of the undisturbed He^+-ion.[2] The curve reaches this eigenvalue at a distance of a few atomic units, which shows that the target nucleus is fully screened. The second lowest eigenvalue approaches the energy eigenvalue of the OPM helium atomic orbital, as in the CMF case. Here the perturbation by the projectile potential does lower the eigenvalues at asymptotic distances by $q_{\mathrm{p}}/R_{\mathrm{in}}$. For example, at $R_{\mathrm{in}} = 10\,\mathrm{au}$ $\varepsilon = -1.018\,\mathrm{Ha}$ which is 0.1 Ha below the OPM eigenvalue.

The differences between the CMF and AC approach seen in figure 33 have an immediate consequence for the TC-BGM calculations: in the CMF approach eigenfunctions of the projectile are helium atomic orbitals, while for the AC calculation the projectile orbitals are hydrogen-like. The structure of the model space in the TC-BGM also biases the calculations for the target as the higher order basis states that represent the continuum are generated (44) from target orbitals only.

[2] In the CMF as well as the AC ansatz for small internuclear distances the collision system approaches the $R_{\mathrm{in}} \to 0$ limit of a combined $Z_{\mathrm{p}} + Z_{\mathrm{t}}$ nuclear charge.

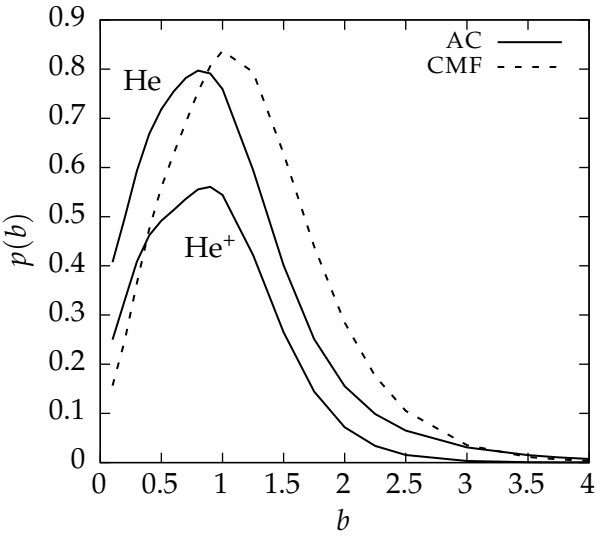

Figure 34: Target and projectile 1s single-electron probabilities $p(b)$ for transfer to the other collision centre, at $E = 25\,\mathrm{keV/u}$ calculated with a TCAO basis. AC (solid line) transfer from the He target and from the He^+ projectile. CMF (dashed line) both curves are identical.

This bias can be avoided with a TCAO basis that comprises only eigenstates (1s to 4f) of the target and the projectile, no higher order BGM states are included. It comes at the cost that without states representing the continuum a TCAO basis only allows electron transfer between the target and the projectile, and vice versa. Such a basis is of very limited use in a collision calculation, but it can provide a good test. Single-electron probabilities for 1s target electron transfer to the projectile, and the analogous projectile quantity, calculated with a TCAO basis, are shown in figure 34 (as functions of the impact parameter b and for 25 keV/u impact energy). Due to the symmetry of the description the transition probabilities $p(b)$ for a target and a projectile electron are identical in the CMF calculation.

In contrast, the AC calculation results in two distinct curves for target and projectile electrons. Electron transfer probabilities from the projectile to the target are lower than those from the target to the projectile. This agrees with the expectation; the initially unscreened projectile is more attractive. An interpretation of these curves beyond such basic observations is not sensible though, as the TCAO basis can describe strongly perturbed states at small internuclear distances only poorly. For example, the CMF and AC target 1s curves in figure 34 diverge for $b < 3$, this difference could be to any degree due to: (i) non-vanishing parts of target orbitals reach into the space where the minimum function flips in the AC case (i.e. positions $\boldsymbol{r}$ where $r_\mathrm{p} < r_\mathrm{t}$), while the target Hamiltonian stays unchanged in the CMF case; (ii) the TCAO bases in the AC and CMF calculations are different but both describe the problem inadequately.

A full BGM basis $\{|\chi_\nu^\mu\rangle\}$ was generated with (44) from helium atomic eigenstates $|\varphi_\nu^0\rangle$. The maximum values M_ν for the hierarchy levels, $\mu \leq M_\nu$, are in the notation of table 2 (p. 54):

1s	2s	2p	3s	3p	3d	4s	4p	4d	4f
0	0	1	2	2	2	3	2	5	6

Basis convergence is not as good as that observed for the ion–neon collisions (cf. section 4.1). Nonetheless, small changes of the hierarchy lead to results that differ by no more than 10%. This is acceptable, since theoretical works for similar systems (e.g. He^{2+}–He [81, 82, 100, 136], Li^{2+}–He [136]) give reason to expect far greater discrepancies with experimental results.

The helium $1s$ state does couple to pseudo states which leads to artificially increased electron removal probabilities. This was similar to the numerical problems described in section 4.1 for the neon $1s$ state. The simple solution used before, namely, removing the $1s$ from the basis, is not possible here. However, the coupling to the continuum led to an error independent of the impact parameter b that was corrected for on the level of single-electron probabilities. Since this prevents a determinantal analysis the multinomial method of section 3.2 was used to calculate total cross sections σ_{kl} to find at final time k electrons at the projectile and l in the continuum.

6.2 RESULTS

Total cross sections σ_{kl} for the projectile electron loss channels ($k = 0$) are shown in figure 35. In panel (a) it can be seen that for loss coincident with an unchanged target charge state, σ_{01}, the AC leads to considerably reduced cross sections compared to the CMF calculation (108) and much better agreement with experimental data by DuBois [68]. While the CMF calculation overestimates the experimental data considerably, the AC calculation tends to underestimate them below 50 keV/u noticeably. Target ionization coincident with projectile electron loss cross sections σ_{02} and σ_{03} are shown in figure 35 (b). For both channels the AC calculation leads to smaller cross sections than the CMF calculation. In the case of single ionization of the target, σ_{02}, the AC curve agrees well with the experimental data of DuBois [68] at low impact energies. The data by Santos et al [78],

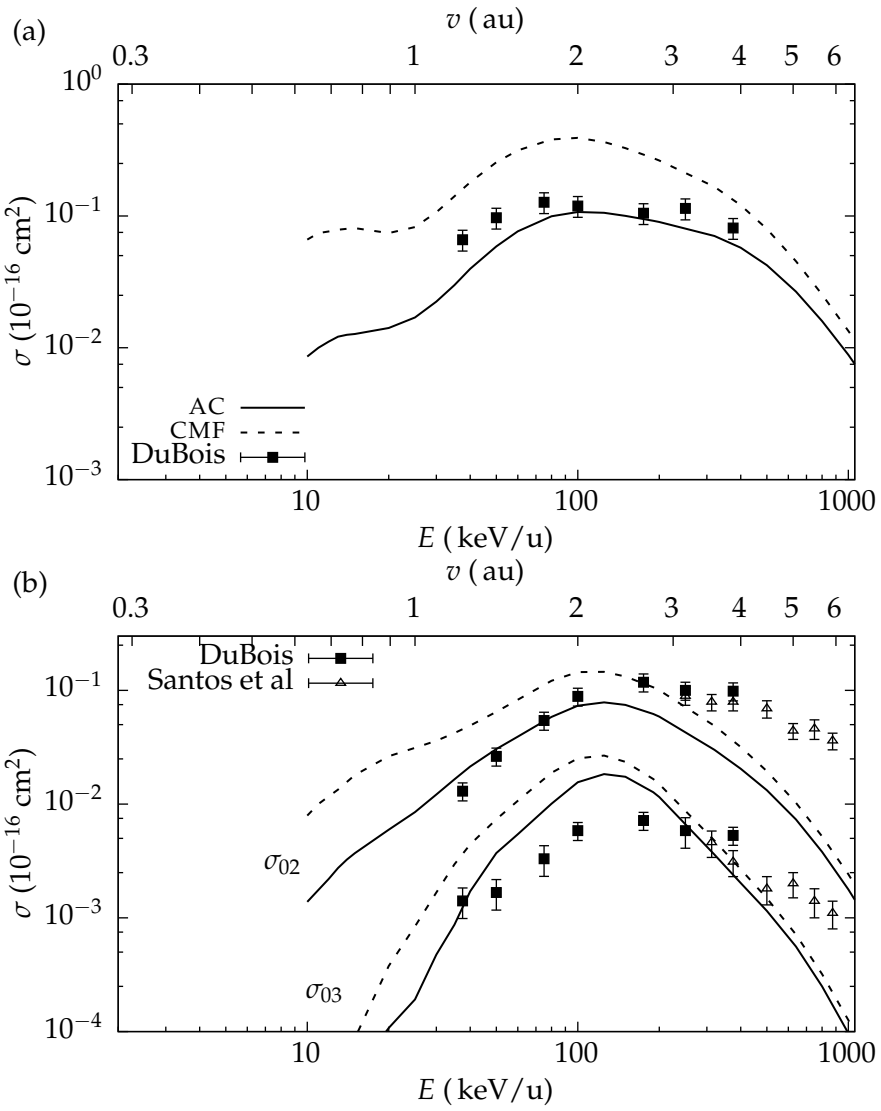

Figure 35: (a) Total cross sections for projectile electron loss with unchanged target σ_{01} and (b) coincident with target single σ_{02} and double σ_{03} ionization in He^+–He collisions. TC-BGM calculations: AC (solid line), CMF (dashed line). Experimental data: DuBois [68] (squares); Santos et al [78] (triangles).

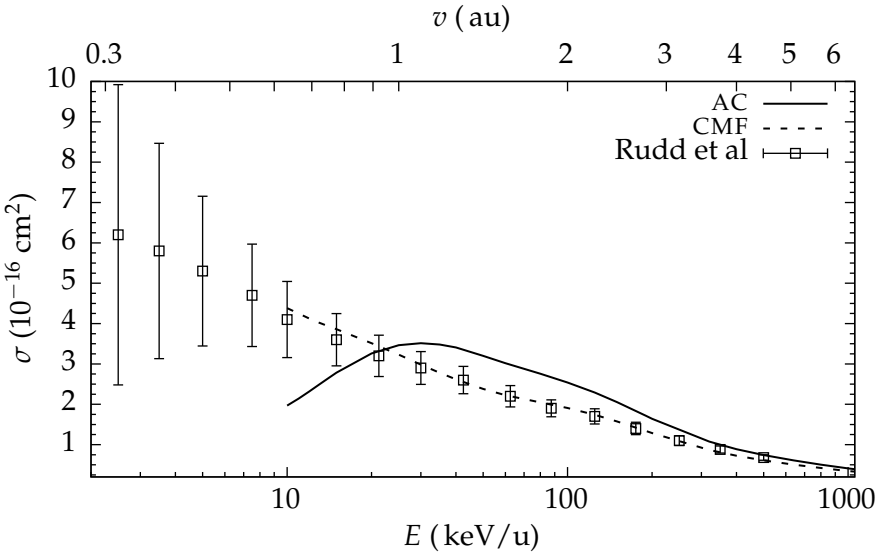

Figure 36: Net recoil ion production σ_+ in He^+–He collisions. TC-BGM calculations: AC (solid line), CMF (dashed line). Experimental data: Rudd et al [58].

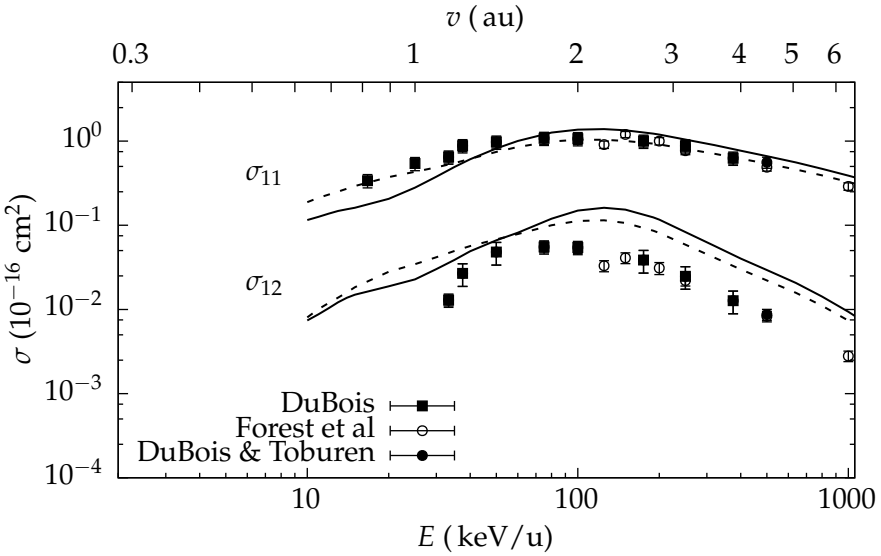

Figure 37: Pure single σ_{11} and double σ_{12} ionization in He^+–He collisions. TC-BGM calculations: AC (solid line), CMF (dashed line). Experimental data: DuBois [68] (squares); Forest et al [77] (open circles); DuBois and Toburen [76] (filled circles).

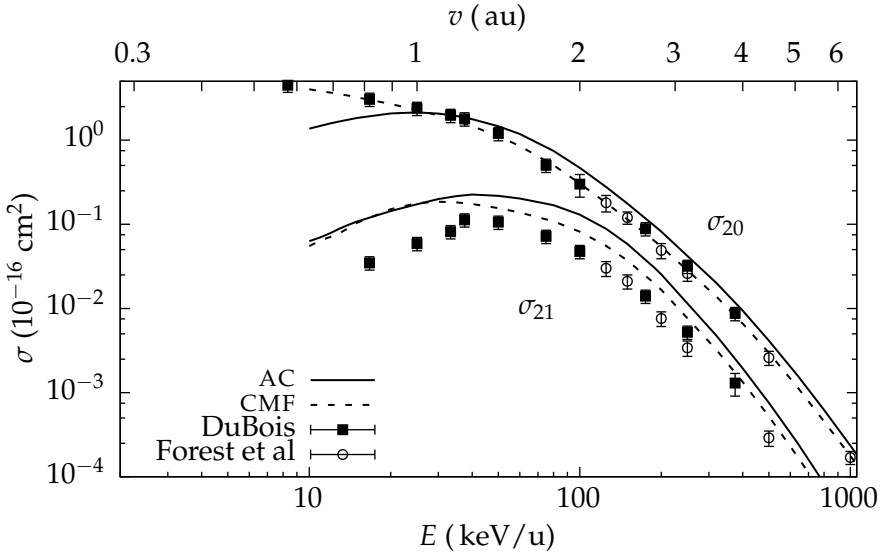

Figure 38: Capture σ_{20} and transfer ionization σ_{21} in He^+–He collisions. TC-BGM calculations: AC (solid line), CMF (dashed line). Experimental data: DuBois [68] (squares); Forest et al [77] (open circles).

which were measured at high impact energies only, are underestimated by both calculations. For these collisions antiscreening (cf. p. 98) contributes strongly to electron removal [78] but is not described in the present model. For the loss coincident double ionization channel σ_{03} both theoretical curve considerably overestimate the experimental data at low impact energies. The difference between the AC and the CMF calculations is smaller for the σ_{03} channel as was the case for the other projectile loss channels. The multinomial probability $P_{03} = (p_t^{\text{ion}})^2 p_p^{\text{ion}}$ is mostly determined by target ionization which changes less between AC and CMF calculations. This appears also to be the source of the poor agreement with the data. Double electron removal from helium is in general a correlated process which is not very well described in an IEM description [71, 132, 133].

While the projectile loss channels are in general described better in the AC model than in the CMF approach, the very opposite is the case

for target ionization. This can be seen for the net recoil ion production σ_+ which is shown in figure 36 in comparison to experimental results [58]. The CMF calculation is in very good agreement with the experiment while the AC calculation underestimates the experiment at low impact energies and overestimates it for intermediate energies; only in the limit of fast collisions does the AC curve approach the CMF curve.

The two observations (i) that both models cannot describe two-electron processes well; and (ii) the CMF approach describes processes involving initial target electrons better than the AC approach; are repeated for pure single σ_{11} and double σ_{12} ionization (fig. 37) as well as capture σ_{20} and transfer ionization σ_{21} (fig. 38): The CMF approach leads to results in good agreement with the experimental data for the single-electron processes (σ_{11}, σ_{20}), while the AC neither agrees qualitatively nor quantitatively. The two-electron processes (σ_{12}, σ_{21}) are overestimated by both calculations.

Discussion

Compared to the CMF approach the AC approach leads for the projectile electron loss channel to a considerable reduction of cross sections and better agreement with the experiment. On the other hand, target electron removal is poorly described by the AC ansatz. This is most evident for the net recoil ion production where the AC calculations cannot reproduce the impact energy dependence of the experimental results, while the CMF calculation is in excellent agreement with the data. This points to a fundamental flaw of the present AC approach: The asymptotic behaviour of the AC Hamiltonian at large internuclear distances is only correct when electron removal from the target is negligible, namely, before the collision or for large impact parameters. Over a considerable impact parameter and energy range it is unlikely that the two collision partners remain unchanged.

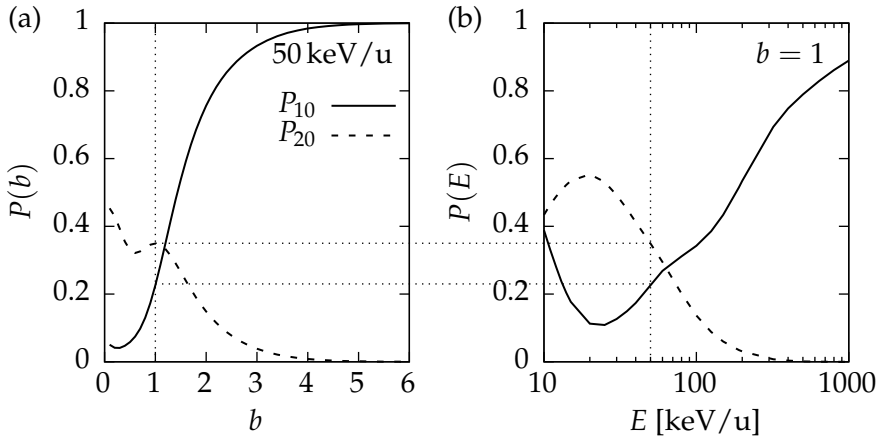

Figure 39: He^+–He multinomial probabilities for unchanged target and projectile P_{10} (solid line) and single capture P_{20} (dashed line) as functions of the impact parameter b (a) at 50 keV/u impact energy; and the impact energy E (b) at $b = 1$ au, from an AC calculation.

This can be seen in figure 39 that shows the elastic probability P_{10} as a function of the impact parameter b and the impact energy E. While the probabilities in the figure are results of an AC calculation, there are no relevant qualitative differences vis-à-vis a CMF calculation. In close collisions at 50 keV/u it is unlikely to find the collision system in a configuration that corresponds to the AC Hamiltonian (109) at $t = t_f$. Likewise, over a large impact energy range close collisions at $b = 1$ au lead also to a changed charge state of either collision partner. It is in fact more likely for close and slow collisions ($b < 1$ au, $E < 60$ keV/u) to find two electrons at the projectile and one at the target, which can be seen in the P_{20} curves also shown in the figure. The collision system is flipped, so to say, the projectile is a helium atom and the target a He^+-ion after the collision. Such a situation is better described by the CMF Hamiltonian. In order to address this, one may consider to extend the present AC approach (109) beyond the no-response approximation, for example, by using a global re-

sponse model similar to that described in section 1.3.

However, a global response approach for the AC Hamiltonian ought to model the time dependence of the effective potentials of both, target and projectile, for the following reasons: At large internuclear distances the CMF and AC Hamiltonians are effectively the same for initial target electrons. Yet the ionization results of the CMF approach agree with experiments while the AC results do not. The discrepancy must come from times when the AC Hamiltonian appears in effect different from the CMF Hamiltonian. That is, when non-vanishing parts of the target orbitals are closer to the projectile nucleus than to the target nucleus, $r_\mathrm{t} > r_\mathrm{p}$. In the no-response AC Hamiltonian of the He^+–He system (109) when $r_\mathrm{t} > r_\mathrm{p}$ the effective potential of the projectile is always more attractive than that of the target. A reduction of the target screening only might have little effect. An increase in projectile screening, as response to electron capture, however, might have a noticeable effect. Yet, target screening ought not be neglected either. The arguments used in the case of the target-response model to neglect projectile response for ion–neon collisions – namely, that processes involving target electrons are preferred by the CMF IEM description, and that projectile response was found insignificant for a similar collision system – do not apply to the present case. After all, we went to great lengths in the AC approach to avoid the preference of the IEM for one centre. However, no further effort was spent on the AC ansatz as we found it more worthwhile to continue with the CMF approach for the ion–neon collision systems, discussed in chapter 5.

CONCLUSIONS

Results of theoretical calculations for dressed-ion (B^{2+} and C^{3+}) and bare-ion (He^{2+} and Li^{3+}) impact on neon atoms are presented in this dissertation. The non-perturbative quantum mechanical TC-BGM was used with a common–mean-field description of the collision problem to compute single-electron transition amplitudes. This description is based on a TDHF ansatz, where the many-electron wave function is expressed as a Slater determinant that comprises single-electron wave functions.

Local potential approximations led to single-electron equations in the form of TDSEs with a common Hamiltonian for electrons of both collision centres. This common–mean-field description has the disadvantage that the asymptotic behaviour is not correct for the initial projectile electrons at large internuclear distances before the collision. The time dependence of the electronic screening of the target nucleus was considered with a global target response model, where the screening potential is scaled with a factor that is a function of the electron occupation of the target.

Two statistical final-state analyses were used to calculated multi-electron probabilities and total cross sections, namely, a determinantal analysis, and a multinomial method. Many-electron probabilities are obtained in the former method from inner products of Slater determinants representing the propagated states at final time and final configurations, Pauli exclusion is adhered to. The multinomial method is a combinatoric approach where single-electron probabilit-

ies quantify independent events, whose products are many-electron processes. This approach does not consider the antisymmetry of the many-electron state and thus does not respect the Pauli exclusion principle.

ION–NEON COLLISIONS

Total cross sections resulting from the present calculations were compared with experimental data. While the agreement of the theoretical calculations for specific collision channels varied, overall the results were in good agreement with the experiments for all four ion–neon collision systems. For collision channels where only few electrons underwent transitions the agreement was good except for the projectile electron loss channels. At small impact energies the experiments were considerably overestimated for these channels, which can be understood as a consequence of the choice of effective potentials in the common–mean-field approach used for the two-centre collision problem. In contrast, at large impact energies the picture was reversed and the experiments were considerably underestimated because antiscreening, a significant cause of electron loss in these fast collisions [52], was not considered in the calculations.

Moreover, the present calculations tend to overestimate experimental pure multiple target ionization cross sections corresponding to high final target charge states. This was most noticeable for triple and quadruple ionization of neon by He^{2+} and Li^{3+} ions. Based on experience from previous IEM calculations (e.g. [48, 49, 103, 126]) one might expect the agreement with experiments to be good as long as the final target charge state does not exceed the initial projectile charge state by more than one [123]. Yet, while this expectation was met by the He^{2+}–Ne calculation, quadruple target ionization in collisions with Li^{3+}-ions was considerably overestimated. In contrast, for pure multiple target ionization, by dressed-ion projectile

impact, namely, by B^{2+} and C^{3+}, the calculations were in fairly good agreement with experimental results, including quadruple ionization. Presumably, the stronger projectile nuclear potential is responsible. While at large internuclear distances before the collision the nuclear potential is screened and appears like an equicharged bare ion, in close collisions where the electronic densities of both collision partners overlap the actual nuclear potential plays a role. For the single and double (pure) ionization channels the agreement between calculations and experiments is slightly better for bare-ion than for dressed-ion projectiles. A reason for this could be the greater complexity due to the presence of electrons at the projectile, as these can be transferred to the target or transition to the continuum. This leads to more processes that contribute to the observed collision channels, each of which also contributing its uncertainties.

The influence of active projectile electrons on pure target ionization cross sections was investigated for the B^{2+}–Ne collision system by comparing the present results with results of a determinantal analysis where these electrons were considered passive. Overall, the active projectile electron results were in better agreement with experimental results than the passive projectile electron results. At high impact energies the absence of projectile electron loss led to overestimation of the experimental data. The passive-projectile electron calculations resulted in cross sections that were close to results of a CDW-EIS calculation [35] for which projectile electrons were also considered passive.

The passive-projectile electron calculations underestimated experimental pure ionization data at low impact energies. Also they led to total cross sections that are lower than those resulting from the present active projectile electron calculation. This seems counterintuitive at first, since the inclusion of active projectile electrons in the model provides an additional mechanism for the projectile charge state to be changed. In turn, ionization events would contribute to

other charge-state-coincident ionization channels.

This prompted an investigation of such transfer ionization processes. A multinomial final-state analysis was used as it allows a very detailed view of specific multi-electron transfer and ionization mechanisms. It was found that transfer ionization contributes significantly to pure single ionization in slow B^{2+}–Ne collisions. In the transfer ionization processes that contributed the most one electron is captured by the projectile and one electron emitted from the projectile to the continuum, Transfer ionization processes were also found to be the prevalent mechanisms for pure double ionization for impact energies below 100 keV/u. In particular a process where one electron is transferred to the projectile and one electron each from the target and projectile is emitted to the continuum contributed by far the most to the pure double ionization cross sections.

The pure ionization cross sections calculated with the multinomial analysis were found to differ from the results calculated with the determinantal analysis. This can be attributed to Pauli exclusion which may prevent electron transfer, and which is considered in the determinantal analysis but not in the multinomial analysis. This was corroborated by single-electron transition probabilities that showed that electrons which are transferred from the projectile to the target are almost exclusively transferred to the L shell. While this shell is initially fully occupied in the neon atom, such transfers are not necessarily fully suppressed. Whenever single-electron transition probabilities from the projectile to the target are significant, coincident transitions from the initial target states reduce the neon ground state occupation. Capture is then not fully blocked by Pauli exclusion.

Transfer ionization processes where the projectile charge state is the same after the collision do contribute to pure target ionization cross sections. A theoretical description that represents electrons at the projectile only by an effective charge or screening potential, leads to different results than a description where projectile electrons are

actively propagated (but that is otherwise identical). One might surmise that active projectile electrons ought to be considered when a description of dressed-ion–atom collisions is to be accurate, even when solely channels where the projectile charge state remains unchanged are considered.

Net recoil ion production σ_+ results for all four ion–neon collision systems were shown. Unfortunately, experimental data are available only for He^{2+}-Ne collisions. The present calculations agreed well with those data. The net recoil ion production can be calculated independently from the statistical models as it depends only on the target net occupation; it is thus inclusive of all final projectile charge states. In the present calculations it was found that for medium to fast collisions the positive ion production (i.e. the target charge-state weighted sum of pure multiple ionization cross sections) accounts for most of the net recoil ion production. At low impact energies multiple ionization coincident with electron capture are the predominant contributions in all four investigated collision systems. Contributions of single, double, and triple capture (only for Li^{3+} and C^{3+}) coincident target ionization were shown. In the case of dressed ion impact, B^{2+} and C^{3+}, target ionization coincident with projectile electron loss was also found to contribute significantly to the net recoil ion production in medium to fast collisions.

In a comparison of equicharged bare- and dressed-ion collisions with neon it was found that net recoil ion production by He^{2+} impact exceeds that by B^{2+} impact in slow collisions. This is unexpected, as typically in collisions with dressed ions target ionization is stronger than in collisions with the corresponding bare ions [56]. This is indeed the case for C^{3+}–Ne vs. Li^{3+}–Ne: the net recoil ion production by dressed-ion impact consistently exceeds that by the bare-ion impact. The reason for the unusual feature for the doubly-charged ions was found in a comparison of the projectile-charge-

state-coincident contributions to the net recoil ion production: capture by the He^{2+} ion, and in particular double capture, was considerably stronger than by the B^{2+} ion.

TARGET RESPONSE

TC-BGM calculations that used the no-response approximation and the target-response model of reference [48] were compared. For the He^{2+}–Ne collision system the target-response calculation was clearly in better agreement with experimental data. For pure multiple target ionization in collisions of B^{2+} with Ne the no-response calculations agreed well with experimental results, while the target-response calculation tended somewhat to underestimate the data. Previous BGM calculations that considered target response [48, 49, 51, 103] showed that target response partially compensates the tendency of IEM calculations to overestimate multiple ionization. When assuming that this is also the case for the B^{2+}–Ne collision system, one might speculate that the calculated cross sections were lower (or the experimental values too large) for unknown reasons, which in turn compensates for the IEM-inherent overestimation of multiple ionization.

The no-response and target-response curves do not converge at high impact energies. This indicates a deficiency of the present implementation of the target-response model. The final-state probabilities are extracted by projecting the propagated states on initial atomic eigenstates of the target. However, when target electron removal is high in a collision, screening of the nuclear potential is considerably lowered in the present target-response model, and the instantaneous eigenstates of the (now) ionic target differ considerably from atomic eigenstates. This leads to an overestimation of target electron removal, as was shown in test calculations for He^{2+} impact on neon. It is advisable to implement in the TC-BGM code a method to project on instantaneous eigenstates for the final-state analysis.

In the present target-response model the screening potential of the target depends on the target occupation, and therefore the definition of when an electron is bound. When target and projectile are in close proximity and the electronic densities overlap defining an electron as belonging to, and screening, one centre is only a pragmatic approximation. There is no physical reason for either approach namely, to project onto initial atomic orbitals or instantaneous eigenstates. Nonetheless, both approaches to the target-response model were also included in the above mentioned test calculations. While the results of both approaches differ slightly they do not cause the oscillations in time that can be observed for probabilities that were extracted by projecting on initial atomic eigenstates. Therefore there is no need to move from projecting on atomic orbitals to instantaneous orbitals to find the target net occupation as input for the response model.

The target response model was used to calculate the present results for ion–neon collisions, with the exception of the pure target ionization B^{2+}–Ne cross sections in the fifth chapter that were compared with CDW-EIS results [35] that used a no-response calculation.

ASYMPTOTIC CORRECTION

The present TC-BGM model can accurately describe collision systems over a wide energy range and for many collision channels. An example are the present results for ion–neon collisions. However, the TC-BGM cannot give an accurate overview of all collision channels in dressed-ion–atom collisions, because the description of projectile electrons lacks in the common–mean-field description. One reason is that initial projectile electrons are propagated with a Hamiltonian whose effective potentials do not show the correct asymptotic behaviour at large internuclear distances before the collision. It has been attempted to address this shortcoming by using a piecewise defined potential function in the common Hamiltonian.

The ansatz was described and adopted for He^+–He collisions: The exchange potentials of the target atom and the projectile ion are arguments in a minimum function, which selects the combination of exchange potentials that is correct at large internuclear distances for electrons of each respective centre. Calculations with this asymptotic correction approach for He^+–He were in better agreement with experiments for projectile electron loss channels than results of a common–mean-field description. In contrast, target electron removal channels, for example the net recoil ion production, were in considerably worse agreement with experiments when the asymptotic correction approach was used.

An explanation is that the asymptotic correction Hamiltonian only shows the correct asymptotic behaviour before the collision. During the collision the occupation of the target and the projectile may change dramatically, resulting in a collision system that is described badly by the asymptotic correction. Due to a (fortuitous) symmetry of the potentials the common–mean-field approach describes the situation after the collision much better.

Considering response in the asymptotic correction approach could perhaps correct this deficiency, by letting effective potentials of both centres adapt to the changing electron occupation. However, using the present global response model for this would run into difficulties that would require coarse approximations and introduce free parameters. One suspects this would overburden the IEM ansatz, and as it would invite tweaking of the free parameters, water down the first principles approach of the theoretical model.

DISCUSSION AND OUTLOOK

In its current state the TC-BGM is a well developed method that can be used to calculate total cross sections for diverse collision channels in ion–atom collisions [71, 112, 113, 123, 124, 126, 132, 133, 137].

The author therefore considers the TC-BGM as the method of choice for the intermediate energy regime. While the *n*CTMC [40, 41] can provide the same level of detail, the classical approach does not consider the quantum mechanical nature of atomic collision problems. The quantum mechanical CDW-EIS method has also been used to describe dressed-ion–atom collisions [26, 28–35], however, active electrons could not be considered for both collision centres. Moreover, perturbative methods reach their limits at relative velocities $v \gtrapprox 1\,\mathrm{au}$, which are of particular interest in ion–atom collisions.

In the recent decades the experimental techniques have advanced to kinematically complete collision experiments, in broad strokes these can be subsumed as variants of cold target recoil ion momentum spectroscopy (COLTRIMS) [138]. Such experiments can determine the three-dimensional momentum vectors of all free particles in the final state. It is increasingly expected from theoretical descriptions to provide not only total cross sections but differential cross sections (DCS) $\mathrm{d}\sigma/\mathrm{d}\Omega$ that quantify the probability of finding the system in a given final state in dependence of the scattering angle.

That this is quite a challenge for current models, can be seen, for example, in the context of recent experimental results for collisions of 75 keV protons on atomic hydrogen [139] a single-electron problem. According to Sarkadi [36] non-perturbative quantum mechanical descriptions are necessary to deal with this problem (a very recent example for such a calculation is in reference [140]).

Zapukhlyak [106, 141–143] used the eikonal method [144] to calculate DCS from impact-parameter dependent transition amplitudes obtained with the TC-BGM. Calculations with this method are very involved and require much experience and effort to conduct. A more recent collaborative effort combines TC-BGM and CDW-EIS calculations for ion–lithium collisions [145, 146].

A more fundamental problem are the limitations of the IEM when

describing processes that involve several electrons. In part the overestimation of multiple ionization can be attributed to response. In the TDOPM approach of Keim et al [98] the time-dependent effective potential is calculated at each time step as the wave functions evolve in time. This approach can be considered as the exchange-only limit of a time-dependent DFT (TDDFT) description for the collision problem. Keim found significant response effects for ionization of helium by antiproton, proton, and bare helium-ion impact [98, 100, 147]. Yet, it did correct only partially the overestimation of double ionization. One may interpret the difference of these calculations to experimental results as due to correlation.

Recent works investigated if correlation is responsible for increased double ionization of helium by antiproton impact [71, 132] as well as proton and He^{2+} impact [133]. While a correlation model [148] for the effective potential had only little effect, considering final-state correlation led to improved results in comparison to results of an IEM final-state analysis. Double-ionization probabilities were obtained from the two-electron density which was approximated with the model of reference [149] (no exact functionals for many-electron observables are known in DFT).

Final-state correlation and response might provide a way to improve the description of multiple ionization, multiple capture and similar many-electron channels that can be observed in experiments. This is worthwhile pursuing insofar, as a complete and accurate description of a collision problem by a single calculation, and in the case of an effective single-particle description, with a common Hamiltonian, is a demanding test for theory. Unfortunately, there is no apparent way for a single IEM calculation to yield accurate results for initial target as well as projectile electrons when a local mean-field approximation is used. In the future a spin TDDFT approach might help to address this problem.

In its present form the TC-BGM with the target-response model can

provide, as was said above, fairly accurate total cross sections to a large number of collision channels and different collision systems. In combination with models on the level of the final-state analysis it is possible to include, for example, post-collisional Auger effects [111, 150], antiscreening [52], and fragmentation of molecules [126]. Calculations for further collision systems are by themselves interesting as this can help to understand the physics behind observed cross-section data. It also gives confidence in the method as its weaknesses get established, which could help to quantify uncertainties of TC-BGM calculations. [2]. Theoretical predictions of cross sections for charge transfer have potential for practical applications, for example, ion collisions with water molecules are especially interesting in this regard [113, 126, 137, 151].

BIBLIOGRAPHY

[1] D. E. Post, *Role of atomic collisions in fusion*, Report PPPL-1877 (Princeton Plasma Phys. Lab., 1982).

[2] H. K. Chung, B. J. Braams, K. Bartschat, A. G. Csaszar, G. W. F. Drake, T. Kirchner, V. Kokoouline, and J. Tennyson, "Uncertainty estimates for theoretical atomic and molecular data", (2016), arXiv:1603.05923 [physics.atom-ph].

[3] R. Rajeev, T. Madhu Trivikram, K. P. M. Rishad, V. Narayanan, E. Krishnakumar, and M. Krishnamurthy, "A compact laser-driven plasma accelerator for megaëlectronvolt-energy neutral atoms", Nat. Phys. **9**, 185 (2013).

[4] L. J. Lanzerotti, et al., "The hot plasma environment at Jupiter: Ulysses results", Science **257**, 1518 (1992).

[5] J. G. Wang, A. R. Turner, D. L. Cooper, D. R. Schultz, M. J. Rakovic, W. Fritsch, P. C. Stancil, and B. Zygelman, "Electron capture in collisions of S^{4+} with helium", J. Phys. B **35**, 3137 (2002).

[6] W. Wolff, I. J. de Souza, A. C. Tavares, G. F. S. de Oliveira, and H. Luna, "Electron-recoil ion and recoil ion-projectile coincidence techniques applied to obtain absolute partial collision cross sections", Rev. Sci. Instrum. **83**, 123107 (2012) 10.1063/1.4772395.

[7] D. Schardt, "Tumor therapy with high-energy carbon ion beams", Nucl. Phys. A **787**, Proc. 9. Int. Conf. Nucl. – Nucl. Coll., 633 (2007).

[8] E. Haettner, H. Iwase, M. Krämer, G. Kraft, and D. Schardt, "Experimental study of nuclear fragmentation of 200 and 400 MeV/u ^{12}C ions in water for applications in particle therapy", Phys. Med. Biol. **58**, 8265 (2013).

[9] E. Takada, "Carbon ion radiotherapy at NIRS-HIMAC", Nucl. Phys. A **834**, 10. Int. Conf. Nucl. – Nucl. Coll., 730c (2010).

[10] H. Nikjoo, S. Uehara, W. E. Wilson, M. Hoshi, and D. T. Goodhead, "Track structure in radiation biology: Theory and applications", Int. J. Radiat. Biol. **73**, 355 (1998).

[11] C. Champion, "Multiple ionization of water by heavy ions: a Monte Carlo approach", Nucl. Instrum. Methods Phys. Res. B **205**, 11. Int. Conf. Phys. Highly Charged Ions, 671 (2003).

[12] Y. Ralchenko, "A guide to internet atomic databases for hot plasmas", J. Quant. Spect. Rad. Transf. **99**, 499 (2006).

[13] C. Cocke, and R. Olson, "Recoil ions", Phys. Rep. **205**, 153 (1991).

[14] E. Montenegro, W. Meyerhof, and J. McGuire, "Role of two-center electron–electron interaction in projectile electron excitation and loss", in , Vol. 34, edited by B. Bederson, and H. Walther, Advances In Atomic, Molecular, and Optical Physics (Academic Press, 1994), pp. 249–300.

[15] (a) E. Schrödinger, "Quantisierung als Eigenwertproblem", Annalen der Physik **79**, 361 (1926); (b) ibid. **79**, 489 (1926); (c) ibid. **80**, 437 (1926); (d) ibid. **81**, 109 (1926); (e) "An undulatory theory of the mechanics of atoms and molecules", Phys. Rev. **28**, 1049 (1926).

[16] A. E. S. Green, D. L. Sellin, and A. S. Zachor, "Analytic independent-particle model for atoms", Phys. Rev. **184**, 1 (1969).

[17] D. R. Bates, and G. Griffing, "Inelastic collisions between heavy particles I: Excitation and ionization of hydrogen atoms in fast encounters with protons and with other hydrogen atoms", Proc. Phys. Soc. London, Sec. A **66**, 961 (1953).

[18] D. S. F. Crothers, and J. F. McCann, "Ionisation of atoms by ion impact", J. Phys. B **16**, 3229 (1983).

[19] I. M. Cheshire, "Continuum distorted wave approximation; resonant charge transfer by fast protons in atomic hydrogen", Proc. Phys. Soc. London, Sec. A **84**, 89 (1964).

[20] D. Belkic, "A quantum theory of ionisation in fast collisions between ions and atomic systems", J. Phys. B **11**, 3529 (1978).

[21] D. S. F. Crothers, and R. McCarroll, "Correlated continuum - dis-torted-wave resonant double electron capture in He^{2+}–He collisions", J. Phys. B **20**, 2835 (1987).

[22] H. F. Busnengo, A. E. Martínez, and R. D. Rivarola, "Single electron capture from He targets", J. Phys. B **29**, 4193 (1996).

[23] P. D. Fainstein, V. H. Ponce, and R. D. Rivarola, "A theoretical model for ionisation in ion–atom collisions. Application for the impact of multicharged projectiles on helium", J. Phys. B **21**, 287 (1988).

[24] L. Gulyas, P. D. Fainstein, and A. Salin, "CDW-EIS theory of ionization by ion impact with Hartree-Fock description of the target", J. Phys. B **28**, 245 (1995).

[25] M. E. Galassi, P. N. Abufager, A. E. Martinez, R. D. Rivarola, and P. D. Fainstein, "The continuum distorted wave eikonal initial state model for transfer ionization in H^+, He^{2+} + He collisions", J. Phys. B **35**, 1727 (2002).

[26] C. C. Montanari, E. C. Montenegro, and J. E. Miraglia, "CDW-EIS calculations for multiple ionization of Ne, Ar, Kr and Xe by the impact of H^+ and He^+ , including post-collisional electron emission", J. Phys. B **43**, 165201 (2010).

[27] J. K. M. Eichler, A. Tsuji, and T. Ishihara, "Electron capture into partially stripped projectile ions", Phys. Rev. A **23**, 2833 (1981).

[28] J. M. Monti, J. Fiol, D. Fregenal, P. D. Fainstein, R. D. Rivarola, W. Wolff, E. Horsdal, G. Bernardi, and S. Suárez, "Experimental and theoretical results on electron emission in collisions between partially dressed ions with He targets", Phys. Scr. **2013**, 014031 (2013).

[29] J. M. Monti, R. D. Rivarola, and P. D. Fainstein, "Quantum interferences in swift highly-charged dressed-ion–atom collisions", J. Phys. B **41**, 201001 (2008).

[30] V. Rodríguez, "CDW-EIS theoretical calculations of projectile deflection for single ionization in highly charged ion–atom collisions", Nucl. Instrum. Methods Phys. Res. B **205**, 498 (2003).

[31] P. D. Fainstein, and L. Gulyás, "Three- and four-body dynamics in single ionization of He by swift highly charged Au^{53+} ions", J. Phys. B **38**, 317 (2005).

[32] J. M. Monti, R. D. Rivarola, and P. D. Fainstein, "Distorted wave theories for dressed-ion–atom collisions with GSZ projectile potentials", J. Phys. B **44**, 195206 (2011).

[33] J. E. Miraglia, and M. S. Gravielle, "Ionization of He, Ne, Ar, Kr, and Xe by impact of He^+ ions", Phys. Rev. A **81**, 042709 (2010).

[34] C. C. Montanari, J. E. Miraglia, W. Wolff, H. Luna, A. C. F. Santos, and E. C. Montenegro, "Multiple ionization of atoms including post-collisional contributions", J. Phys.: Conf. Ser. **388**, 012036 (2012).

[35] W. Wolff, H. Luna, A. C. F. Santos, E. C. Montenegro, R. D. DuBois, C. C. Montanari, and J. E. Miraglia, "Effectiveness of projectile screening in single and multiple ionization of Ne by B^{2+}", Phys. Rev. A **84**, 042704 (2011).

[36] L. Sarkadi, "Classical trajectory Monte Carlo model calculations for ionization of atomic hydrogen by 75-keV proton impact", Phys. Rev. A **82**, 052710 (2010).

[37] R. Abrines, and I. C. Percival, "Classical theory of charge transfer and ionization of hydrogen atoms by protons", Proceedings of the Physical Society **88**, 861 (1966).

[38] R. E. Olson, and A. Salop, "Charge-transfer and impact-ionization cross sections for fully and partially stripped positive ions colliding with atomic hydrogen", Phys. Rev. A **16**, 531 (1977).

[39] R. E. Olson, "Multiple-ionisation cross sections for highly - strip-ped ions colliding with He, Ne and Ar:" J. Phys. B **12**, 1843 (1979).

[40] D. R. Schultz, R. E. Olson, C. O. Reinhold, S. Kelbch, C. Kelbch, H. Schmidt-Bocking, and J. Ullrich, "Coincident charge state production in F^{6+}+Ne collisions", J. Phys. B **23**, 3839 (1990).

[41] D. R. Schultz, P. S. Krstić, and C. O. Reinhold, "Inelastic processes in 1-1000 keV/u collisions of Be^{q+} ($q = 2 - 4$) ions with atomic and molecular hydrogen", Phys. Scr. **1996**, 69 (1996).

[42] J. Fiol, R. E. Olson, A. C. F. Santos, G. M. Sigaud, and E. C. Montenegro, "Simultaneous projectile and target ionization in He^+ + Ne collisions", J. Phys. B **34**, L503 (2001).

[43] L. H. Toburen, R. D. DuBois, C. O. Reinhold, D. R. Schultz, and R. E. Olson, "Experimental and theoretical study of the electron spectra in 66.7–350-keV/u C^++He collisions", Phys. Rev. A **42**, 5338 (1990).

[44] K. J. Schaudt, N. H. Kwong, and J. D. Garcia, "Fully converged time-dependent Hartree-Fock results for He^{2+}–He: Correlation in inclusive charge transfer", Phys. Rev. A **43**, 2294 (1991).

[45] A. Henne, H. J. Lüdde, A. Toepfer, T. Gluth, and R. M. Dreizler, "Doorway approximation of the optical potential: application to one-electron ion–atom scattering systems", J. Phys. B **26**, 3815 (1993).

[46] O. J. Kroneisen, H. J. Lüdde, T. Kirchner, and R. M. Dreizler, "The basis generator method: optimized dynamical representation of the solution of time-dependent quantum problems", J. Phys. A **32**, 2141 (1999).

[47] T. Kirchner, H. J. Lüdde, M. Horbatsch, and R. M. Dreizler, "QM description of ionization, capture, and excitation in proton collisions with atomic oxygen", Phys. Rev. A **61**, 052710 (2000).

[48] T. Kirchner, M. Horbatsch, H. J. Lüdde, and R. M. Dreizler, "Time-dependent screening effects in ion–atom collisions with many active electrons", Phys. Rev. A **62**, 042704 (2000).

[49] T. Kirchner, M. Horbatsch, and H. J. Lüdde, "Time-dependent independent-particle model calculation of multiple capture and ionization processes in p-Ar, $\overline{p}$-Ar, and He^{2+}-Ar collisions", Phys. Rev. A **66**, 052719 (2002).

[50] T. Kirchner, and M. Horbatsch, "Nonperturbative calculation of projectile-electron loss, target ionization, and capture in He^++Ne collisions", Phys. Rev. A **63**, 062718 (2001).

[51] T. Kirchner, M. Horbatsch, and H. J. Lüdde, "Coupled mean-field description of electron removal processes in He^+–Ne and He^+-Ar collisions", J. Phys. B **37**, 2379 (2004).

[52] T. Kirchner, A. C. F. Santos, H. Luna, M. M. Sant'Anna, W. S. Melo, G. M. Sigaud, and E. C. Montenegro, "Charge-state-correlated cross sections for electron loss, capture, and ionization in C^{3+}–Ne collisions", Phys. Rev. A **72**, 012707 (2005).

[53] T. Kirchner, H. J. Lüdde, and M. Horbatsch, "A time-dependent quantal approach to electronic transitions in atomic collisions", Recent Res. Devel. Phys **5**, 433 (2004).

[54] W. Seim, A. Muller, I. Wirkner-Bott, and E. Salzborn, "Electron capture by Li^{i+} ($i = 2, 3$), N^{i+}, and Ne^{i+} ($i = 2, 3, 4, 5$) ions from atomic hydrogen", J. Phys. B **14**, 3475 (1981).

[55] M. B. Shah, and H. B. Gilbody, "Screening-antiscreening effects in one-electron loss by fast Li^+ and Li^{2+} ions in collisions with H, H_2 and He", J. Phys. B **24**, 977 (1991).

[56] S. H. Be, T. Tonuma, H. Kumagai, H. Shibata, H. Kase, T. Kambara, I. Kohno, and H. Tawara, "Net ionisation cross-sections of rare gases by collisions of fast highly charged heavy projectiles", J. Phys. B **19**, 1771 (1986).

[57] C. L. Cocke, "Production of highly charged low-velocity recoil ions by heavy-ion bombardment of rare-gas targets", Phys. Rev. A **20**, 749 (1979).

[58] M. E. Rudd, T. V. Goffe, A. Itoh, and R. D. DuBois, "Cross sections for ionization of gases by 10–2000-keV He^+ ions and for electron capture and loss by 5–350-keV He^+ ions", Phys. Rev. A **32**, 829 (1985).

[59] T. Tonuma, H. Kumagai, T. Matsuo, and H. Tawara, "Coincidence measurements of slow recoil ions with projectile ions in 42-MeV Ar^{q+}-Ar collisions", Phys. Rev. A **40**, 6238 (1989).

[60] S. Kelbch, C. L. Cocke, S. Hagmann, M. Horbatsch, C. Kelbch, R. Koch, H. Schmidt-Bocking, and J. Ullrich, "Recoil-ion production cross sections and differential scattering angle dependences in 2.5-15 MeV F^{n+} ($n = 4, 6, 8$) on Ne collisions", J. Phys. B **23**, 1277 (1990).

[61] W. S. Melo, M. M. Sant'Anna, A. C. F. Santos, G. M. Sigaud, and E. C. Montenegro, "Electron loss and single and double capture of C^{3+} and O^{5+} ions in collisions with noble gases", Phys. Rev. A **60**, 1124 (1999).

[62] W. Wolff, H. Luna, A. C. F. Santos, E. C. Montenegro, and G. M. Sigaud, "Electron loss and multiple electron capture of B^{2+} and C^{3+} ions colliding with Ne and Ar targets", Phys. Rev. A **80**, 032703 (2009).

[63] A. C. F. Santos, G. M. Sigaud, W. S. Melo, M. M. Sant'Anna, and E. C. Montenegro, "Absolute cross sections for electron loss, electron capture, and multiple ionization in collisions of C^{3+} with noble gases", Phys. Rev. A **82**, 012704 (2010).

[64] J. S. Ihani, H. Luna, W. Wolff, and E. C. Montenegro, "Multiple ionization of neon induced by Li^{3+} and C^{3+} projectiles: Influence of projectile screening in the ionization and electron capture channels", J. Phys. B **46**, 115208 (2013).

[65] A. L. C. Losqui, F. Zappa, G. M. Sigaud, W. Wolff, M. M. Sant'Anna, A. C. F. Santos, H. Luna, and W. S. Melo, "Absolute cross sections for electron loss, electron capture, and multiple ionization in collisions of Li^{2+} with argon", J. Phys. B **47**, 045202 (2014).

[66] M. E. Rudd, T. V. Goffe, and A. Itoh, "Ionization cross sections for 10-300 keV/u and electron-capture cross sections for 5-150 keV/u He^{2+} ions in gases", Phys. Rev. A **32**, 2128 (1985).

[67] R. D. DuBois, "Ionization and charge transfer in He^{2+}–rare-gas collisions. II", Phys. Rev. A **36**, 2585 (1987).

[68] R. D. DuBois, "Multiple ionization in He^{+}–rare-gas collisions", Phys. Rev. A **39**, 4440 (1989).

[69] M. E. Rudd, R. D. DuBois, L. H. Toburen, C. A. Ratcliffe, and T. V. Goffe, "Cross sections for ionization of gases by 5-4000-keV protons and for electron capture by 5-150-keV protons", Phys. Rev. A **28**, 3244 (1983).

[70] M. Born, and R. Oppenheimer, "Zur Quantentheorie der Molekeln", Annalen der Physik **389**, 457 (1927).

[71] N. Henkel, M. Keim, H. J. Lüdde, and T. Kirchner, "Density-functional-theory investigation of antiproton–helium collisions", Phys. Rev. A **80**, 032704 (2009), arXiv:1103.3785 [physics.atom-ph].

[72] H.-C. Kao, T.-Y. Kuo, H.-P. Yen, C.-M. Wei, and K.-N. Huang, "Relativistic cross sections of electron-impact ionization of hydrogenic ions", Phys. Rev. A **45**, 4646 (1992).

[73] E. Engel, and S. H. Vosko, "Accurate optimized-potential-model solutions for spherical spin-polarized atoms: Evidence for limitations of the exchange-only local spin-density and generalized-gradient approximations", Phys. Rev. A **47**, 2800 (1993).

[74] M. Zapukhlyak, T. Kirchner, H. J. Lüdde, S. Knoop, R. Morgenstern, and R. Hoekstra, "Inner- and outer-shell electron dynamics in proton collisions with sodium atoms", J. Phys. B **38**, 2353 (2005).

[75] H. J. Lüdde, and R. M. Dreizler, "Comment on inclusive cross sections", J. Phys. B **18**, 107 (1985).

[76] R. D. DuBois, and L. H. Toburen, "Single and double ionization of helium by neutral-particle to fully stripped ion impact", Phys. Rev. A **38**, 3960 (1988).

[77] J. L. Forest, J. A. Tanis, S. M. Ferguson, R. R. Haar, K. Lifrieri, and V. L. Plano, "Single and double ionization of helium by intermediate–to–high-velocity He^+ projectiles", Phys. Rev. A **52**, 350 (1995).

[78] A. C. F. Santos, G. M. Sigaud, W. S. Melo, M. M. Sant'Anna, and E. C. Montenegro, "Absolute cross sections for projectile electron loss accompanied by target multiple ionization in collisions of He^+ with noble gases", J. Phys. B **44**, 045202 (2011).

[79] J. Blaizot, and G. Ripka, *Quantum theory of finite systems* (MIT Press, 1986).

[80] A. Henne, A. Toepfer, H. J. Lüdde, and R. M. Dreizler, "Time-dependent Hartree-Fock calculations for the $He^+(1s)$+$He^+(1s)$ system", J. Phys. B **19**, L361 (1986).

[81] K. C. Kulander, K. R. S. Devi, and S. E. Koonin, "Time-dependent Hartree-Fock theory of charge exchange: Application to He^{2+} + He", Phys. Rev. A **25**, 2968 (1982).

[82] W. Stich, H. Lüdde, and R. Dreizler, "Time-dependent Hartree-Fock description of one and two electron capture in collisions of $(He–He)^{2+}$", Phys. Lett. A **99**, 41 (1983).

[83] K. Gramlich, N. Grün, and W. Scheid, "The time-dependent Hartree-Fock method within a Gauss-lobe basis and application to proton–He collisions", J. Phys. B **19**, 1457 (1986).

[84] P.-O. Löwdin, "Quantum theory of many-particle systems. III. extension of the Hartree-Fock scheme to include degenerate systems and correlation effects", Phys. Rev. **97**, 1509 (1955).

[85] (a) H. Nakashima, and H. Nakatsuji, "Solving the Schrödinger equation for helium atom and its isoelectronic ions with the free iterative complement interaction (ICI) method", J. Chem. Phys. **127**, 224104 (2007); (b) Y. I. Kurokawa, H. Nakashima,

and H. Nakatsuji, "Solving the Schrödinger equation of helium and its isoelectronic ions with the exponential integral (Ei) function in the free iterative complement interaction method", Phys. Chem. Chem. Phys. **10**, 4486 (2008).

[86] J. H. McGuire, "Correlation in atomic scattering", Phys. Rev. A **36**, 1114 (1987).

[87] N. Stolterfoht, "Electron correlation processes in energetic ion–atom collisions", in *Spectroscopy and collisions of few-electron ions: Proc. study conf. SCOFEI '88*, edited by M. Ivascu, V. Florescu, and V. Zoran, (World Scientific, New York, London, Singapore, 1989).

[88] D. A. Micha, and K. Runge, "Time-dependent many-electron approach to slow ion–atom collisions: The coupling of electronic and nuclear motions", Phys. Rev. A **50**, 322 (1994).

[89] J. D. Talman, and W. F. Shadwick, "Optimized effective atomic central potential", Phys. Rev. A **14**, 36 (1976).

[90] R. T. Sharp, and G. K. Horton, "A variational approach to the unipotential many-electron problem", Phys. Rev. **90**, 317 (1953).

[91] J. C. Slater, "A simplification of the Hartree-Fock method", Phys. Rev. **81**, 385 (1951).

[92] W. Kohn, and L. J. Sham, "Self-consistent equations including exchange and correlation effects", Phys. Rev. **140**, A1133 (1965).

[93] R. M. Dreizler, and E. K. U. Gross, *Density functional theory: an approach to the quantum many-body problem* (Springer, Berlin, Heidelberg, 1990).

[94] E. Engel, and R. Dreizler, *Density functional theory: an advanced course* (Springer, Berlin, Heidelberg, New York, 2011).

[95] E. Engel, and R. Dreizler, *Orbital functionals: Optimized potential method*, Chap. 6 in [94].

[96] E. Engel, "Orbital-dependent functionals for the exchange-correlation energy: a third generation of density functionals", in *A primer in density functional theory*, edited by C. Fiolhais, F. Nogueira, and M. Marques, Lecture Notes in Physics, Vol. 620 (Springer, Berlin, New York, 2003).

[97] C. A. Ullrich, U. J. Gossmann, and E. K. U. Gross, "Time-dependent optimized effective potential", Phys. Rev. Lett. **74**, 872 (1995).

[98] M. Keim, A. Achenbach, H. J. Lüdde, and T. Kirchner, "Microscopic response effects in collisions of antiprotons with helium atoms and lithium ions", Phys. Rev. A **67**, 062711 (2003).

[99] T. Kirchner, M. Horbatsch, E. Wagner, and H. J. Lüdde, "Modelling of polarization and correlation effects in the ionization of helium by antiprotons", J. Phys. B **35**, 925 (2002).

[100] M. Keim, "Untersuchung lokaler Responseffekte in interatomaren Stößen mit zwei aktiven Elektronen im Rahmen zeitabhängiger Dichtefunktionaltheorie", Dissertation (Johann Wolfgang Goethe-Universität, Frankfurt am Main, 2004).

[101] T. Kirchner, "Pauli blocking and laser manipulation of the electron dynamics in atomic collisions", Nucl. Instrum. Methods Phys. Res. B **233**, 151 (2005).

[102] T. Kirchner, H. J. Lüdde, and M. Horbatsch, "Nonperturbative study of the rearrangement dynamics in ion–atom collisions with active electrons on projectile and target", Phys. Scr. **2004**, 364 (2004).

[103] T. Kirchner, M. Horbatsch, and H. J. Lüdde, "Nonperturbative calculation of charge-changing processes in C^{4+} scattering from neon atoms", Phys. Rev. A **64**, 012711 (2001).

[104] H. J. Lüdde, and R. M. Dreizler, "Microscopic optical potentials for time-dependent quantum systems", Comput. Phys. Commun. **63**, 345 (1991).

[105] (a) H. Feshbach, "Unified theory of nuclear reactions", Ann. Phys. **5**, 357 (1958); (b) ibid. **19**, 287 (1962).

[106] M. Zapukhlyak, "Einblicke in die atomare Vielteilchendynamik von Streuprozessen durch ab-initio-Rechnungen", Dissertation (Clausthal University of Technology, 2008).

[107] T. Kirchner, "Quantentheoretische Beschreibung von Vielelektronenprozessen in ion–atom-Stößen", Dissertation (Johann Wolfgang Goethe-Universität, Frankfurt am Main, 1999).

[108] H. J. Lüdde, A. Henne, T. Kirchner, and R. M. Dreizler, "Optimized dynamical representation of the solution of time-dependent quantum problems", J. Phys. B **29**, 4423 (1996).

[109] H. J. Lüdde, A. Henne, A. Salin, A. Toepfer, and R. M. Dreizler, "Time-dependent optical potentials: non-Markovian and doorway approaches", J. Phys. B **26**, 2667 (1993).

[110] T. Kirchner, H. J. Lüdde, and R. M. Dreizler, "Effective single-particle description of single and multiple processes in p^+–Ne collisions", Phys. Rev. A **61**, 012705 (1999).

[111] T. Spranger, and T. Kirchner, "Auger-like processes in multiple ionization of noble gas atoms by protons", J. Phys. B **37**, 4159 (2004).

[112] L. Fernández-Menchero, T. Kirchner, and H. J. Lüdde, "Extension of the basis generator method for application to laser-molecule interactions", Phys. Rev. A **79**, 023416 (2009).

[113] M. Murakami, T. Kirchner, M. Horbatsch, and H. J. Lüdde, "Single and multiple electron removal processes in proton–water-molecule collisions", Phys. Rev. A **85**, 052704 (2012).

[114] F. de Heer, J. Schutten, and H. Moustafa, "Ionization and electron capture for helium ions incident on noble and diatomic gases between 10 and 150 keV.", Physica **32**, 1793 (1966).

[115] A. S. Schlachter, K. H. Berkner, W. G. Graham, R. V. Pyle, P. J. Schneider, K. R. Stalder, J. W. Stearns, J. A. Tanis, and R. E. Olson, "Ionization of rare-gas targets by collisions of fast highly charged projectiles", Phys. Rev. A **23**, 2331 (1981).

[116] A. S. Schlachter, W. Groh, A. Müller, H. F. Beyer, R. Mann, and R. E. Olson, "Production of highly charged rare-gas recoil ions by 1.4-MeV/amu U^{44+}", Phys. Rev. A **26**, 1373 (1982).

[117] M. Horbatsch, "A semiclassical time-dependent Hartree model calculation of capture and multiple ionization in heavy ion–Ar collisions", Phys. Lett. A **187**, 185 (1994).

[118] E. W. Weisstein, *Multinomial Coefficient*, MathWorld–A Wolfram Web Resource, Retrieved on 2015-06-18.

[119] J. H. McGuire, *Electron correlation dynamics in atomic collisions* (Cambridge University Press, Cambridge, UK, 1997) Chap. 6.

[120] T. A. Carlson, and M. O. Krause, "Electron shake-off resulting from *K*-shell ionization in neon measured as a function of photoelectron velocity", Phys. Rev. **140**, A1057 (1965).

[121] H. Knudsen, L. H. Andersen, P. Hvelplund, G. Astner, H. Cederquist, H. Danared, L. Liljeby, and K. .-.-G. Rensfelt, "An experimental investigation of double ionisation of helium atoms in collisions with fast, fully stripped ions", J. Phys. B **17**, 3545 (1984).

[122] M. H. Mittleman, "Single and double ionization of He by electrons", Phys. Rev. Lett. **16**, 498 (1966).

[123] G. Schenk, M. Horbatsch, and T. Kirchner, "Role of projectile electrons for target-recoil-charge-state production in intermediate-energy B^{2+}–Ne collisions", Phys. Rev. A **88**, 012712 (2013).

[124] G. Schenk, and T. Kirchner, "Multiple ionization of neon atoms in collisions with bare and dressed ions: A mean-field description considering target response", Phys. Rev. A **91**, 052712 (2015).

[125] G. Schenk, and T. Kirchner, "Bare- and dressed-ion impact collisions from neon atoms studied within a nonperturbative mean-field approach", Phys. Proc. **66**, 22 (2015).

[126] M. Murakami, T. Kirchner, M. Horbatsch, and H. J. Lüdde, "Fragmentation of water molecules by proton impact: The role of multiple electron processes", Phys. Rev. A **85**, 052713 (2012).

[127] J. H. McGuire, *Electron correlation dynamics in atomic collisions* (Cambridge University Press, Cambridge, UK, 1997) Chap. 8.

[128] E. C. Montenegro, A. C. F. Santos, W. S. Melo, M. M. Sant'Anna, and G. M. Sigaud, "Effective strength of the electron-electron interaction in simultaneous projectile and target ionization", Phys. Rev. Lett. **88**, 013201 (2001).

[129] I. Dmitriev, Y. Teplova, and Y. Fainberg, "Investigation of cross sections for the formation and destruction of negative boron ions", J. Exp. Theor. Phys. **89**, 830 (1999).

[130] J.-Y. Chesnel, H. Merabet, X. Husson, F. Frémont, D. Lecler, H. Jouin, C. Harel, and N. Stolterfoht, "Energy dependence of cross sections for double-electron capture in 48–132-keV C^{6+}+He collisions", Phys. Rev. A **53**, 2337 (1996).

[131] J. P. Hansen, and K. Taulbjerg, "Electron correlation in highly-charged-ion collisions", Phys. Rev. A **45**, R4214 (1992).

[132] M. Baxter, and T. Kirchner, "Correlation in time-dependent density-functional-theory studies of antiproton–helium collisions", Phys. Rev. A **87**, 062507 (2013).

[133] M. Baxter, and T. Kirchner, "Time-dependent density-functional-theory studies of collisions involving He atoms: Extension of an adiabatic correlation-integral model", Phys. Rev. A **93**, 012502 (2016).

[134] L. H. Toburen, N. Stolterfoht, P. Ziem, and D. Schneider, "Electronic screening in heavy-ion–atom collisions", Phys. Rev. A **24**, 1741 (1981).

[135] M. Keim, T. Kirchner, and H. J. Lüdde, *Private communication*, 2005.

[136] W. Stich, H. J. Lüdde, and R. M. Dreizler, "TDHF calculations for two-electron systems", J. Phys. B **18**, 1195 (1985).

[137] M. Murakami, T. Kirchner, M. Horbatsch, and H. J. Lüdde, "Quantum-mechanical calculation of multiple electron removal and fragmentation cross sections in He^+–H_2O collisions", Phys. Rev. A **86**, 022719 (2012).

[138] J. Ullrich, R. Moshammer, A. Dorn, R. Dörner, L. P. H. Schmidt, and H. Schmidt-Böcking, "Recoil-ion and electron momentum spectroscopy: reaction-microscopes", Rep. Prog. Phys. **66**, 1463 (2003).

[139] A. C. Laforge, K. N. Egodapitiya, J. S. Alexander, A. Hasan, M. F. Ciappina, M. A. Khakoo, and M. Schulz, "Three-body dynamics in single ionization of atomic hydrogen by 75 keV proton impact", Phys. Rev. Lett. **103**, 053201 (2009).

[140] H. R. J. Walters, and C. T. Whelan, "Differential ionization of a one-electron target under bare-ion impact: application to proton-impact ionization of atomic hydrogen", Phys. Rev. A **92**, 062712 (2015).

[141] M. Zapukhlyak, T. Kirchner, A. Hasan, B. Tooke, and M. Schulz, "Projectile angular-differential cross sections for transfer and transfer excitation in proton collisions with helium", Phys. Rev. A **77**, 012720 (2008).

[142] M. Zapukhlyak, and T. Kirchner, "Projectile angular-differential cross sections for electron transfer processes in ion–helium collisions: Evidence for the applicability of the independent electron model", Phys. Rev. A **80**, 062705 (2009).

[143] T. Spranger, M. Zapukhlyak, and T. Kirchner, "Angular differential cross sections for multiple ionization of rare gas atoms by protons with inclusion of Auger-like processes", J. Phys. B **40**, 1081 (2007).

[144] R. McCarroll, and A. Salin, "Impact parameter treatment of atomic collisions", J. Phys. B **1**, 163 (1968).

[145] T. Kirchner, N. Khazai, and L. Gulyás, "Role of two-electron excitation-ionization processes in the ionization of lithium atoms by fast ion impact", Phys. Rev. A **89**, 062702 (2014), arXiv:1501.03900 [physics.atom-ph].

[146] M. D. Śpiewanowski, L. Gulyás, M. Horbatsch, and T. Kirchner, "Doubly-differential-cross-section calculations for *K*-shell-vacancy production in lithium by fast O^{8+}–ion impact", Phys. Rev. A **93**, 012707 (2016), arXiv:1601.01340 [physics.atom-ph].

[147] M. Keim, A. Achenbach, H. Lüdde, and T. Kirchner, "Time-dependent density functional theory calculations for collisions of bare ions with helium", Nucl. Instrum. Methods Phys. Res. B **233**, 240 (2005).

[148] M. Lein, and S. Kümmel, "Exact time-dependent exchange-correlation potentials for strong-field electron dynamics", Phys. Rev. Lett. **94**, 143003 (2005).

[149] F. Wilken, and D. Bauer, "Adiabatic approximation of the correlation function in the density-functional treatment of ionization processes", Phys. Rev. Lett. **97**, 203001 (2006).

[150] G. Schenk, and T. Kirchner, "Projectile electron loss in collisions of Ar^{6+} and Ar^{8+} ions with He and Ar atoms", J. Phys. B **42**, 205202 (2009).

[151] T. Kirchner, M. Murakami, M. Horbatsch, and H. J. Lüdde, "Chapter eleven – Ion collisions with water molecules: A time-dependent density functional theory approach", in *Theory of heavy ion collision physics in hadron therapy*, Vol. 65, edited by D. Belkić, Advances in Quantum Chemistry (Academic Press, 2013), pp. 315–337.

COLOPHON

This document is set in 12 pt Palatino and was created with LaTeX2e. The layout is based on a KOMA script class.

The present document is set in a single-sided layout for the electronic theses and dissertations (ETD) database of York University. Page numbers differ from the version approved by the examination committee, however, the content of the main matter is identical. The front matter of the present version of this document also lacks the dedication, which, unfortunately, does not conform with the regulations of the ETD.